

Statistics for dark matter subhalo searches in gamma rays from a kinematically constrained population model: Fermi-LAT-like telescopes

Gaétan Facchinetti,^{1,*} Julien Lavalle,^{1,†} and Martin Stref^{2,‡}

¹*Laboratoire Univers & Particules de Montpellier (LUPM),
CNRS & Université de Montpellier (UMR-5299),*

Place Eugène Bataillon, F-34095 Montpellier Cedex 05 — France

²*LAPTh, Université Savoie Mont Blanc & CNRS,*

Chemin de Bellevue, 74941 Annecy Cedex — France

Cold dark matter subhalos are expected to populate galaxies in numbers. If dark matter self-annihilates, these objects turn into prime targets for indirect searches, in particular with gamma-ray telescopes. Incidentally, the Fermi-LAT catalog already contains many unidentified sources that might be associated with subhalos. In this paper, we determine the probability for subhalos to be identified as gamma-ray pointlike sources from their predicted distribution properties. We use a semi-analytical model for the Galactic subhalo population, which, in contrast to cosmological simulations, can be made fully consistent with current kinematic constraints in the Milky Way and has no resolution limit. The model incorporates tidal stripping effects from a realistic distribution of baryons in the Milky Way. The same baryonic distribution contributes a diffuse gamma-ray foreground which adds up to that, often neglected in subhalo searches, generated by the smooth dark matter and the unresolved subhalos. This configuration implies a correlation between pointlike subhalo signals and diffuse background. Based on this semi-analytical modeling, we generate mock gamma-ray data assuming an idealized telescope resembling Fermi-LAT and perform a likelihood analysis to estimate the current and future sensitivity to subhalos in the relevant parameter space. We find a number of detectable subhalos of order $\mathcal{O}(< 1)$ for optimistic model parameters and a WIMP mass of 100 GeV, maximized for a cored host halo. This barely provides support to the current interpretation of several Fermi unidentified sources as subhalos. We also find it more likely to detect the smooth Galactic halo itself before subhalos, should dark matter in the GeV-TeV mass range self-annihilate through s -wave processes.

PACS numbers: 12.60.-i,95.35.+d,98.35.Gi

I. INTRODUCTION

While under experimental or observational pressure, the thermal dark matter (DM) scenario is still considered as appealing owing to its simple production mechanism and to the fact that it is within reach of current experiments. A typical realization amounts to assuming that DM is made of exotic particles with masses and couplings to standard model particles such that they can be produced from the hot plasma in the early universe, and to selecting model parameters for which DM is cold [1–3] and with a predicted cosmological abundance that matches with the one measured by cosmological probes [4–7]. If there is no matter-antimatter asymmetry in the dark sector, and if DM is driven to chemical equilibrium before freezing out, then weakly-interacting massive particles (WIMPs) arise as prototypical self-annihilating DM candidates, leading to a diversity of potentially observable signatures¹ [11–16]. In this article, we focus on indi-

rect DM searches [16–18] with gamma rays, and therefore assume that DM self-annihilates in DM halos nearly at rest and into standard model particles, producing gamma rays through direct emission, hadronization of the final states, or bremsstrahlung [19]. This implicitly restricts the available WIMP parameter space to s -wave annihilation processes (typically mediated by pseudo-scalar interactions if DM is made of fermions), for which the annihilation rate does not depend on DM particle velocities. Other parts of the WIMP parameter space (*e.g.* scalar interactions) can still be probed by indirect detection techniques [20, 21], but are more efficiently so with direct detection [15, 22, 23] and at colliders [9, 24, 25]. We also restrict the target space by focusing on searches in the Milky Way (MW) only [26].

The generically rather small scattering rate between WIMPs and the hot plasma in the early universe leads to a very small cutoff scale in the matter power spectrum, implying a typical mass ranging from 10^{-3} - $10^{-12} M_{\odot}$ for the first DM structures to collapse in the matter cosmological era [27–34]. In the standard hierarchical picture of structure formation [35–37], these first minihalos, or

* gaetan.facchinetti@umontpellier.fr; Current affiliation: Service de Physique Théorique, Université Libre de Bruxelles, Boulevard du Triomphe, CP225, 1050 Brussels — Belgium

† lavalle@in2p3.fr

‡ martin.stref@lapth.cnrs.fr

¹One of the main theoretical supports for WIMPs was that it was independently motivated by solutions to the so-called electroweak

hierarchy problem in particle physics. The fact that no new particles have been discovered at the LHC has strongly affected approaches to that issue, see *e.g.* [8], and motivations for WIMPs are now mostly phenomenological [9, 10].

subhalos, merge into larger DM halos, but a significant fraction of them survives tidal disruption and populates galactic halos in numbers today [38–42]. These DM inhomogeneities have long been invoked as potential boosters of the DM annihilation rate in galaxies, enhancing the production of gamma rays and antimatter cosmic rays [43–47]. They could also enhance the gamma-ray power spectrum on specific angular scales [48, 49]. They actually also represent interesting point-source targets for gamma-ray telescopes [47, 50–56], with essentially no X-ray nor radio counterparts (but see [57]). This possibility has generated a particular attention in the recent years as the Fermi-LAT satellite has enriched its catalog with many unidentified and unassociated sources [58, 59], some being interpreted as potential DM subhalos [60–69].

In this study, we take advantage of the recent analytical Galactic subhalo population model developed in Ref. [41] (SL17 henceforth)—see complementary analytical approaches in *e.g.* Refs [42, 70–74]. This model was built to be consistent with both structure formation theory [40, 75] and kinematic constraints on the MW similar to those discussed in Ref. [76]. Some gamma-ray properties of this model were already derived in Ref. [77] using the Clumpy code [78, 79], which aimed at comparing them with predictions from cosmological simulations [80] (so-called MW-like simulations, but obviously with DM and baryonic distributions that may significantly depart from the real MW), but without fully addressing the detectability of individual objects in a realistic diffuse foreground. This issue was partly covered in [66]. Here, we want to inspect the potential of Fermi-like gamma-ray telescopes to detect subhalos in such a model, but going farther than previous studies in the attention given to the contribution of DM annihilation itself to the diffuse background. The model includes a subhalo population, a smooth dark matter halo, and a baryonic distribution, all made consistent with kinematic constraints, and the gravitational tides that prune or disrupt subhalos are calculated from the very same components (see SL17 for details). This internal self-consistency leads to a spatial correlation between the subhalos, the smooth DM, and the baryonic content, which affects the observational properties of the former through the contribution to the diffuse emission of the latter. Baryons induce gravitational tides that deplete the subhalo population and select the most concentrated objects. Besides, they set the intensity of the Galactic gamma-ray foreground (mostly the pionic component), which also plays a role in the balance between diffuse emission and potential pointlike emissions from subhalos. Finally, assessing the detectability of subhalos should also account for the fact that the diffuse DM emission is also bounded by current constraints to be less than the level of Galactic foreground statistical fluctuations [19, 81–88]. This means that part of the naively available parameter space is actually already excluded, and this can be fully characterized in a complete model. We will show that self-consistently combining all these ingredients leads to interesting, though not necessarily

optimistic, consequences in terms of subhalo detectability.

The paper develops according to a very pedestrian approach and is organized as follows. We begin by quickly reviewing our global Galactic model in Sect. II. In Sect. III, we describe the parameter space of subhalos and the related statistical ensemble, from which derive the statistical properties of their gamma-ray emissivity presented in Sect. IV. We further discuss the detectability of DM subhalos in Sect. V, which is the main part of the paper, and where we pay a particular attention to the possible background configurations. In particular, we exploit a simplified statistical method and derive useful analytical results showing *e.g.* the consequence of imposing to detect subhalos *before* the smooth halo on the sensitivity, which we further confirm with a more sophisticated analysis based on a full likelihood method applied to mock data. In that way, we can place ourselves in the context of an idealized experiment resembling Fermi-LAT, and derive predictions for both current and future observations. We summarize our results and draw our conclusions in Sect. VI, to which we invite the expert reader to go directly, and provide additional technical details in the Appendices.

II. REVIEW OF THE SUBHALO POPULATION MODEL

In this section, we motivate the need for a dynamically consistent model for the DM distribution in the MW which globally include both the subhalo population and the smooth Galactic halo—see a more detailed discussion in SL17.

It is well known that in the cold DM scenario, structure formation leads to a high level of self-similarity that translates into an almost universal shape for the dark halos over a large range of scales, close to a parametric Navarro-Frenk-White (NFW henceforth) profile, as found in cosmological simulations [89, 90]. Such a (spherical) halo shape should characterize systems like the MW down to all pre-existing layers of inhomogeneities like subhalos, the latter also globally contributing to shaping the former. Increasing the spatial/mass resolution of cosmological simulations does not modify this picture, it only uncovers a larger population of smaller subhalos in their host halos, sharing similar morphologies [91–93]—the overall profiles of the host halos remaining unaffected. Consistency therefore demands that the sum of the smooth DM component and its substructure be globally following an NFW profile (or any variant motivated by improved fitting formulae [94–96], with possible alterations in the central regions due to baryonic feedback [97–99]).

This actually implies a spatial correlation between the smooth halo and its substructure, the details of which are related to the accretion history and more importantly to the tidal stripping experienced by subhalos and induced

both by the total gravitational potential of the host halo and by baryons (disk shocking, stellar encounters, etc.). This spatial correlation is expected to have some impact on the gamma-ray observability properties of subhalos as pointlike sources, because it translates into a correlation between the hunted sources and the background in which they lurk. Such a correlation was partly accounted for in *e.g.* Refs [47, 78], but without realistic treatment of gravitational tides. At this stage, it is worth recalling that the global DM content of the MW is better and better constrained as the quality of stellar kinematic data improves. This implicitly translates into limits on the distribution of dark subhalos—except for those “visible” subhalos hosting stars and already identified as MW satellites.

Here, we take advantage of the SL17 analytical subhalo population model for the MW. This model is consistent with recent kinematic constraints on the MW, as it is constructed to recover the best-fit Galactic mass model found in [76] (McM17). Note that the McM17 best-fit model (which includes both DM and baryons) is itself consistent with more recent results (*e.g.* Refs [100, 101]) based on analyses of big samples of RR Lyrae or red-giant stars with accurate proper motions inferred from the Gaia survey [102–104]. In the SL17 subhalo population model, subhalo tidal stripping is determined from the detailed distributions of both DM and baryons derived in McM17. The total DM density profile ρ_{tot} is assumed to be spherical and a mixture of two components:

$$\rho_{\text{tot}}(R) = \rho_{\text{sm}}(R) + \rho_{\text{sub}}(R), \quad (1)$$

where R is here the distance to the Galactic center (GC), ρ_{sm} describes the smooth DM component, and ρ_{sub} describes the average mass density in the form of subhalos. More precisely, the latter can formally be expressed as

$$\rho_{\text{sub}}(R) = \int dm_t m_t \frac{dn(R)}{dm_t}, \quad (2)$$

where $n(R)$ is the number density of subhalos and the integral runs over the tidal mass m_t —all this will be properly defined later. Kinematic data set constraints on ρ_{tot} , and therefore, though more indirectly, on n . The SL17 model assumes that if subhalos were hard spheres, they would simply track the smooth component, and then ρ_{sub} would be proportional to ρ_{sm} . Further calculating the effect of tidal stripping allows us to determine how DM initially in ρ_{sub} migrates to ρ_{sm} , a leakage that increases in strength toward the inner parts of the MW where the gravitational potential gets deeper and where the baryonic disk is located. The SL17 model also predicts the spatial dependence of the subhalo concentration distribution function and of the mass function as a consequence of gravitational tides. All this is in perfect qualitative agreement with what is found in cosmological simulations with [105, 106] and without baryons [92, 93, 107].

The main modeling aspects to bear in mind before discussing the gamma-ray properties of subhalos are the following:

- The total DM halo of Eq. (2) is described either as a spherical NFW halo or as a cored halo, whose parameters are given in Appendix A, and which are both consistent with current kinematic constraints.
- We assume inner NFW profiles for subhalos, and consider initial mass and concentration functions inferred from standard cosmology (before tidal stripping).
- The final spatial distribution of subhalos follows the overall DM profile in the outskirts of the MW, but gets suppressed in the central regions of the MW as an effect of gravitational stripping—there is no simple parametric form to describe the smooth and subhalo components together, since the latter depend on the details of tidal stripping: they are predicted from the model.
- Tidal effects make the final mass and concentration functions fully intricate and spatially dependent; they cannot be factorized out and the SL17 model accounts for this physical intrication.
- Gravitational tides prune more efficiently the less concentrated subhalos, hence the more massive objects.
- The tidal subhalo mass m_t (tidal radius r_t) is generically much smaller than the mass m_{200} (the virial radius r_{200}) it would have in a flat cosmological background—the actual minimal mass can therefore be much smaller than the minimal mass considered for subhalos in terms of m_{200} (this will depend on the tidal disruption criterion discussed around Eq. 7).
- the baryonic content of the model comprises a multicomponent axisymmetric disk (thick and thin disks of stars and gas) and a spherical bulge; all these components are taken into account for the gravitational tides, but only the gaseous component is considered to model the regular Galactic diffuse gamma-ray emission.

In the next section, we discuss the statistical properties of subhalos, which are inherited from their cosmological origin.

III. THE SUBHALO POPULATION STATISTICAL ENSEMBLE

In this section, we review the internal properties of subhalos and fully characterize their statistical ensemble. This will later translate into observable gamma-ray properties.

A. Structural properties of subhalos and distribution functions

Here, we introduce the basic definitions inherent to subhalos, which are rather standard [46, 78]. We assume a spherical NFW inner profile for subhalos, defined as

$$\rho(x) = \rho_s \times \{g(x) \equiv x^{-1}(1+x)^{-2}\}, \quad (3)$$

where ρ_s is the scale density, and the scale variable $x \equiv r/r_s$ expresses the distance r to the subhalo center in units of the scale radius r_s , and where the dimensionless parametric function g is explicitly defined as an NFW profile, though it needs not be the case. Note that g encodes all the details of the profile, such that switching to another profile simply amounts to changing g . In the following, we use $\rho(x)$ and $\rho(r)$ interchangeably, letting the reader adapt the definition accordingly. The integrated mass reads

$$m(x) = 4\pi r_s^3 \rho_s \left\{ \mu(x) \equiv \int_0^x dx' x'^2 g(x') \right\}, \quad (4)$$

where we define the dimensionless mass $\mu(x)$ that encodes the morphological details of the inner profile. Again, we use $m(x)$ and $m(r)$ interchangeably in the following.

A subhalo is conventionally defined from its mass on top of a flat background density and its concentration. It is common practice to adopt $m_{200} \equiv m(r_{200})$ for the initial subhalo mass definition. This corresponds to the mass contained inside a radius r_{200} , often called virial radius, over which the subhalo has an average density of 200 times the critical density $\rho_c \equiv 3H_0^2 M_P^2/8\pi$, where H_0 is the Hubble parameter value today, and M_P is the Planck mass². In the following, we use $H_0 = 68 \text{ km/s/Mpc}$. The scale parameters of subhalos are then entirely defined once the concentration parameter $c_{200} \equiv r_{200}/r_s$ is fixed. The latter is not really a physical parameter since it formally depends on the cosmological background density, but tells us how dense the subhalo is inside r_s . Since smaller subhalos have formed first in a denser universe, the concentration is a decreasing function of the mass. In this paper, we use the SL17 model as derived from the concentration-mass relation given in Ref. [108], to which we associate a log-normal distribution function ($p_c(c_{200})$, used below in *e.g.* Eq. (9)), with a variance set (in dex) to $\sigma_c^{\text{dex}} = 0.14$. To simplify the notations, we further use m for m_{200} and c for c_{200} , unless specified otherwise.

Although the mass m and the concentration c fix the internal properties of a subhalo, the only relevant physical parameters are actually ρ_s and r_s , and more importantly the tidal radius r_t . We also introduce

$$x_t \equiv r_t/r_s, \quad (5)$$

its dimensionless version. Subhalos are indeed not moving in a flat background. Tidal radii are actually difficult to determine since they depend on the details of all gravitational effects felt by subhalos along their orbits in the host halo. The SL17 model precisely provides us with a prediction of subhalos' tidal radii which depend on their structural properties, their position in the halo, and on the details of the DM and baryonic components featuring the MW. Therefore, the real mass and extension of a subhalo are not m_{200} nor r_{200} , but instead

$$\text{the tidal radius } r_t(m, c, R) \leq r_{200}, \quad (6a)$$

$$\text{and the tidal mass } m_t = m(r_t) \leq m, \quad (6b)$$

where the dependence of the tidal radius on the subhalo structural properties and on its average position R in the MW has been made explicit. It is important to keep in mind that the tidal extension of a subhalo is usually much smaller than r_{200} , which may strongly decrease the subhalo gamma-ray luminosity with respect to a naive estimate using r_{200} . The SL17 model further proposes a criterion for tidal disruption, which is expressed as a lower limit in x_t . This can be understood as the fact that tidal stripping can be so efficient that the remaining subhalo core has not enough binding energy left to survive, and gets disrupted. In the following, we will mainly use two different disruption thresholds according to the following rule:

$$\text{tidal disruption } \forall x_t < \epsilon_t = \begin{cases} 1 & (\text{fragile subhalos}) \\ 0.01 & (\text{resilient subhalos}) \end{cases} \quad (7)$$

The fragile case refers to a criterion found in early simulation studies of tidal stripping [109], while the latter case accounts for the fact that the disruption efficiency found in simulations is very likely overestimated due to the lack of resolution and to spurious numerical effects [110]. It can actually be reasonably conceived that the very inner parts of subhalos, which are also very dense, could actually survive tidal stripping for a very long time, simply as a consequence of adiabatic invariance [111, 112]. One of the advantages of the SL17 model is that we can really check the impact of the disruption efficiency on gamma-ray predictions by tuning the disruption parameter ϵ_t . Including further evolution of the structural properties themselves is possible in principle [113, 114], but it is actually not straightforward to scale that up to a population study. We will therefore just assume a hard cut of the subhalo density profile at the tidal radius, which can be considered as an optimistic assumption in terms of gamma-ray emissivity. Self-consistently accounting for tidal stripping is anyway already a significant improvement with respect to many past studies.

²The use of ‘‘virial’’ quantities m_{200} and r_{200} can be misleading in the context of subhalo phenomenology. Indeed, the actual mass and radius of a subhalo embedded in the gravitational potential of the MW (assuming spherical symmetry still holds) are the tidal ones, which depend on the tidal stripping it has experienced along its orbit—roughly speaking, the local gravitational potential and the number of disk crossings and stellar encounters along the orbit. Therefore, these virial quantities are only useful to determine the subhalo inner properties, once the mass-concentration relation is fixed.

Beside the individual properties of subhalos, the SL17 model also provides the population’s global properties, which amounts to define a probability distribution function (pdf) for subhalos. Assuming subhalos are independent from each other, the subhalo number density per unit of (virial) mass can be expressed as

$$\frac{dn(R, m)}{dm} = N_{\text{tot}} \int_1^\infty dc \hat{p}_t(R, m, c), \quad (8)$$

where the integral runs over concentration, N_{tot} is the total number of subhalos in the MW, which will be discussed later below Eq. (14), and the global pdf \hat{p}_t is given by

$$\hat{p}_t(R, m, c) = \frac{\theta(x_t(R, m, c) - \epsilon_t)}{K_t} \times p_V(R) \times p_m(m) \times p_c(c). \quad (9)$$

In these equations, $m = m_{200}$ stands for the virial (fictitious) mass in a flat background, $c = c_{200}$ is the concentration parameter, and K_t allows for the normalization to unity over the whole parameter space defined by the product of the volume element $4\pi R^2 dR$ with the concentration element dc , the reference mass element dm , and the associated pdfs. All pdfs p ’s above are normalized to unity over their own individual range. Tidal disruption, despite its quite simple implementation in the form of a step function $\theta()$, induces an intrication of the individual pdfs. Moreover, since the dimensionless tidal radius x_t depends on all parameters, the same holds true for the tidal mass: a subhalo with a given m can obviously have a different m_t depending on its concentration and position in the MW.

For the “fictitious-mass” function $p_m(m)$, we adopt a power law for simplicity,

$$p_m(m) = K_m (m/m_0)^{-\alpha}, \quad (10)$$

where K_m and m_0 are dimensionful constants that allow us to normalize the mass function to unity over the full subhalo mass range. More involved functions can actually be used, but it turns out that the extended Press-Schechter formalism, reflecting the state-of-the-art analytical formalism in this framework [35–37, 115, 116], gives a mass function close to a power law of index $\alpha \sim 1.95$ —see Fig. 1 for illustration. We will therefore use values of 1.9 and 2 as reference cases. The real(tidal)-mass function, in contrast, also depends on position, and can be written

$$\hat{p}_{m_t}(m_t, R) = \int dm p_m(m) \int dc p_c(c) \times \theta(x_t(R, m, c) - \epsilon_t) \times \delta(m - m_t(R, m, c)). \quad (11)$$

This expression makes it clear that the tidal mass function is spatially dependent not only because of tidal disruption (in the step function), but also because of tidal stripping (in the delta function). In the SL17 model, surviving subhalos are more stripped and more concentrated

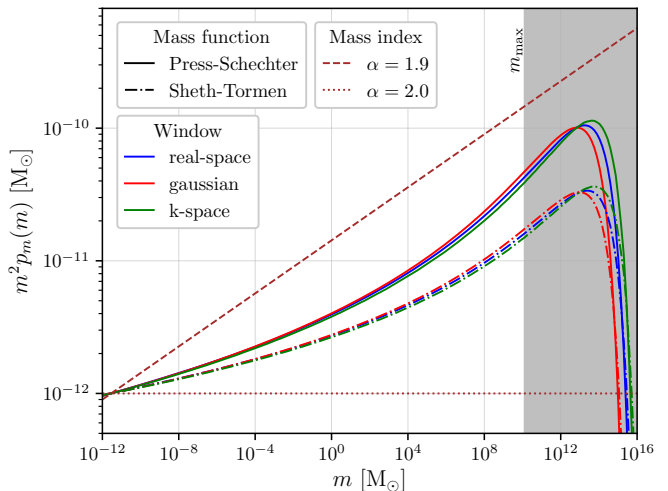


FIG. 1. “Fictitious” virial mass function rescaled by m_{200}^2 as a function of m_{200} at redshift $z = 0$, assuming a cutoff mass $m_{\text{min}} = 10^{-12} M_\odot$. The Press-Schechter and Sheth-Tormen mass functions are calculated using Planck best-fit cosmological parameters [117] for different window filters and fall in all cases between the power-law functions of indices $\alpha = 1.9$ and $\alpha = 2.0$. The gray band corresponds to halos too massive to be accounted for MW subhalos.

as they are found closer to the central regions of the MW. More precisely, tidal stripping acts as a high-pass filter by moving upward a threshold in the concentration distribution function (for a given mass), leading to a strong depletion of the subhalo population as one approaches the central Galactic regions. This effect is genuinely observed in cosmological simulations, and usually parametrically modeled as an additional radial dependence in the median mass-concentration relation (see *e.g.* Refs [47, 107]). In the SL17 model it is not parametrized but predicted from the constrained distributions of the Galactic components.

The SL17 subhalo spatial distribution is built upon assuming that if subhalos were hard spheres, they would simply follow the global DM profile, as is the case for “particles” in cosmological simulations. Therefore, the hard-sphere spatial distribution of the total population of subhalos (including the disrupted ones) is simply

$$p_V(R) = \frac{\rho_{\text{tot}}(R)}{M_{\text{halo}}}, \quad (12)$$

where M_{halo} is the total DM mass in the assumed extent of the MW halo. However, tidal stripping and disruption strongly distorts that hard-sphere distribution, and the actual one only describing surviving subhalos has to integrate the disrupted ones out. It can be written as

$$\hat{p}_V(R) = \int dm \int dc \hat{p}_t(R, m, c) \neq p_V(R), \quad (13)$$

where \hat{p}_t is the global pdf that includes tidal stripping,

given in Eq. (9). The whole population of subhalos is then described from its number density per unit (tidal) mass as follows,

$$\frac{dn(R, m_t)}{dm_t} = N_{\text{tot}} \int dm \int dc \hat{p}_t(R, m, c) \times \delta(m - m_t(R, m, c)). \quad (14)$$

Note that N_{tot} , the total number of subhalos, can be normalized according to different choices. A possibility is to normalize it from the number of dwarf galaxy satellites in the relevant mass range [46] (correcting for sky and efficiency completion), from merger-tree arguments [37, 118], or similarly from a global subhalo mass fraction also in a given mass range Δ_m [47]. We adopt the normalization of SL17 that matches the Via Lactea II DM-only simulation results [92], and conventionally sets the *fictitious* mass fraction³ to $\tilde{f}_{\text{sub}} \sim 10\%$ (for Δ_m taken in the heavy tail of the subhalo mass range, which is very well resolved in simulations). Then

$$N_{\text{tot}} = \frac{K_t \tilde{f}_{\text{sub}} M_{\text{halo}}}{\tilde{K}_t \langle m \rangle_{\Delta_m}}, \quad (15)$$

where K_t is the global pdf normalization introduced in Eq. (9), and the tilde indicates quantities for which baryonic tides are unplugged—see Ref. [41] for details.

It is instructive to calculate the expected number of subhalos that might fall in the mass range of satellite dwarf galaxies in this model, which we give in Table I for different assumptions in the mass function index and in the tidal disruption efficiency. We see that the number of objects more massive than a typical threshold of $10^8 M_\odot$ [113] is of order ~ 100 , consistent with current observations.

Finally, we show the radial distribution of the number density of subhalos for a mass function index $\alpha = 1.9$ in the left panel of Fig. 2, where we have considered both the fragile and resilient subhalos, several values of minimal cutoff mass, and started from two different assumptions for the global Galactic halo—an NFW or a cored halo, both consistent with kinematic constraints [76].

TABLE I. Number of subhalos with a virial mass m , or with physical mass m_t greater than $10^8 M_\odot$ inside a Galactic radius $R_{\text{max}} = 250$ kpc, for fragile ($\epsilon_t = 1$) and resilient ($\epsilon_t = 10^{-2}$) subhalos.

Initial mass index	$N_{\text{sub}}(m_{200} > 10^8 M_\odot) N_{\text{sub}}(m_t > 10^8 M_\odot)$	
	$\epsilon_t = 10^{-2}$	$\epsilon_t = 1$
$\alpha = 1.9$	322 133	268 130
$\alpha = 2.0$	278 108	232 106

³It is called *fictitious* mass fraction because it was calibrated in such a way that each surviving subhalo should carry its full fictitious mass m in the mass integral, even though its real mass m_t is generically smaller.

IV. GAMMA RAYS FROM SUBHALOS: A STATISTICAL DESCRIPTION

In this section, we relate the gamma-ray properties of subhalos to their internal properties. This will fully characterize the statistical properties of their gamma-ray emission, an important step before rigorously determining their detectability properties.

A. Subhalo luminosity

Since we consider DM annihilation in subhalos, it is convenient to define an intrinsic luminosity or emissivity function (in units of squared mass per volume),

$$\xi(r, m, c) = 3 \left\{ \xi_\infty \equiv \frac{4\pi}{3} r_s^3 \rho_s^2 \right\} \times \int_0^x dx' x'^2 g^2(x'), \quad (16)$$

where $x' = r'/r_s$, and where we have introduced a reference luminosity ξ_∞ which is such that for an NFW profile $\xi_\infty = \lim_{r \rightarrow \infty} \xi(r)$ and

$$\xi(2r_s) = \frac{26}{27} \xi_\infty = 0.963 \xi_\infty \approx \xi_\infty. \quad (17)$$

The tidal luminosity of a given object depends only on its position, virial mass, and concentration, which we can express as

$$\xi_t(R, m, c) = \xi(r_t(R, m, c), m, c). \quad (18)$$

For simplicity, we fix the “luminosity” size of a subhalo to

$$\begin{cases} r_t & \text{if } r_t < 2r_s \\ 2r_s & \text{if } r_t \geq 2r_s. \end{cases} \quad (19)$$

This defines the spatial/angular extension of a subhalo in the gamma-ray sky. It will be used when discussing pointlike subhalos in Sect. IV D.

B. Gamma-ray fluxes and J factors

Here we introduce our conventions to deal with gamma-ray fluxes. For a target seen by an observer on Earth, we use the common distance-longitude-latitude triplet (Galactic coordinates), $\vec{s} = (s, l, b)$, such that in the direct Cartesian frame attached to the observer and defined by the unit vectors $(\vec{e}_x, \vec{e}_y, \vec{e}_z)$, where \vec{e}_y points to the GC and \vec{e}_x is also attached to the Galactic plane,

$$\vec{s} = s (\cos b \sin l \vec{e}_x + \cos b \cos l \vec{e}_y + \sin b \vec{e}_z). \quad (20)$$

The GC is therefore located at $\vec{R}_\odot = (0, R_\odot, 0)$, where R_\odot is the distance of the Sun to the GC, such that the target distance R to the GC is simply

$$\begin{aligned} R^2(s, l, b) &= (\vec{s} - \vec{R}_\odot)^2 \\ &= s^2 + R_\odot^2 - 2sR_\odot \{\cos \psi \equiv \cos b \cos l\}, \end{aligned} \quad (21)$$

where we have introduced the angle $\psi = (\vec{s}, \vec{R}_\odot)$ between the line of sight sustaining the target and the observer-GC axis. Since the SL17 model is spherically symmetric, the averaged amplitude of the gamma-ray flux induced by DM annihilation is fully specified by ψ .

Gamma rays accumulate inside a cone characterized by the angular resolution of the telescope, so the spherical MW volume element associated with the spatial distribution of subhalos $4\pi R^2 dR$ (see Sect. III A) has to be replaced by the conical volume element about the line of sight

$$s^2 d\Omega ds = s^2 \sin\theta d\theta d\phi ds, \quad (22)$$

where θ is the polar angle defining the aperture about the line of sight, and ϕ the azimuthal angle. The distance R of the target to the GC then acquires an extra dependence in θ and ϕ which amounts to replace

$$\cos\psi \longrightarrow (\cos\psi \cos\theta - \sin\psi \cos\theta \sin\phi) \quad (23)$$

in Eq. (21). In practice, conical volume integrals are performed over the resolution angle under consideration.

We can now write the gamma-ray flux induced by DM annihilation along the line of sight of angle ψ [equivalently all corresponding pairs (l, b) in Galactic coordinates]:

$$\frac{d\phi_{\gamma,\chi}(E, \psi)}{dE d\Omega} = \frac{\mathcal{S}_\chi(m_\chi, E)}{4\pi} \int_0^{s_{\max}(\psi)} ds \rho_\chi^2(s, \psi), \quad (24)$$

where ρ_χ denotes any DM mass density profile under consideration, and $s_{\max}(\psi) \approx R_{200} + R_\odot \cos\psi$ is the distance to the virial border of the halo in the ψ direction. We have introduced a spectral function,

$$\mathcal{S}_\chi(m_\chi, E) \equiv \frac{\delta_\chi \langle\sigma v\rangle}{2m_\chi^2} \frac{dN_\gamma(E)}{dE}, \quad (25)$$

that carries all the WIMP-model-dependent information, namely the particle mass m_χ , its total s -wave annihilation cross section into photons $\langle\sigma v\rangle$, and the differential photon spectrum dN_γ/dE , which sums up the contributions of all relevant annihilation channels to the photon budget. Parameter $\delta_\chi = 1$ (1/2) for scalar DM or Majorana (Dirac) fermionic DM.

Integrating this flux over a solid angle $\delta\Omega_r = \delta\Omega(\theta_r)$, where θ_r is a fixed resolution angle, we can define a first version of the usual J factor [119] as follows:

$$\frac{d\phi_{\gamma,\chi}(E, \psi, \theta_r)}{dE} = \mathcal{S}_\chi(m_\chi, E) J_\psi(\theta_r), \quad (26)$$

that is

$$J_\psi(\theta_r) \equiv \frac{1}{4\pi} \int_{\delta\Omega_r} d\Omega j_\psi(\psi, \theta, \phi) \quad (27)$$

with $j_\psi(\psi, \theta, \phi) \equiv \int_0^{s_{\max}} ds \rho_\chi^2(s, \psi, \theta, \phi)$

This J factor carries the dimensions of a squared mass per (length)⁵ and may slightly differ from other conventions

found in the literature. Note that in the general case, an *experimental* resolution angle θ_r depends on energy, hence the J factor as defined above. We will account for this energy dependence whenever relevant.

Following up with practical declensions, the flux averaged over the resolution angle θ_r in the ψ direction is simply

$$\left\langle \frac{d\phi_{\gamma,\chi}(E, \psi)}{dE d\Omega} \right\rangle_{\delta\Omega_r} = \mathcal{S}_\chi(m_\chi, E) \mathcal{J}_\psi(\theta_r) \quad (28)$$

$$\text{with } \mathcal{J}_\psi(\theta_r) \equiv \frac{J_\psi(\theta_r)}{\delta\Omega_r}, \quad (29)$$

where we implicitly assume a flat and maximal collection efficiency over θ_r . This angular average of the J factor, \mathcal{J}_ψ , is directly related to the gamma-ray flux per solid angle provided by experimental collaborations in diffuse gamma-ray studies.

Finally, we introduce a last variant of the J factor, more directly related to the real measurements performed by experiments:

$$\overline{J}_\psi(\Delta E) \equiv \frac{\int_{\Delta E} dE \mathcal{A}(E) \mathcal{S}_\chi(E) J_\psi(\theta_r(E))}{\Delta E \overline{\mathcal{A}} \mathcal{S}_\chi}, \quad (30a)$$

$$\overline{\mathcal{J}}_\psi(\Delta E) \equiv \frac{\int_{\Delta E} dE \mathcal{A}(E) \mathcal{S}_\chi(E) \mathcal{J}_\psi(\theta_r(E))}{\Delta E \overline{\mathcal{A}} \mathcal{S}_\chi}, \quad (30b)$$

$$\begin{aligned} \overline{\mathcal{A}} \mathcal{S}_\chi(\Delta E) &\equiv \frac{1}{\Delta E} \int dE \mathcal{A}(E) \mathcal{S}_\chi(E) \quad (30c) \\ &= \frac{\langle\sigma v\rangle}{2m_\chi^2} \frac{\langle\mathcal{N}_\gamma \mathcal{A}\rangle_{\Delta E}}{\Delta E}, \end{aligned}$$

where ΔE is an energy range to be specified and \mathcal{A} is an effective experimental collection area. The latter should depend both on the energy and the angle with respect to the pointing direction, but for simplicity we assume a flat and maximal angular acceptance within the resolution angle θ_r , which can itself depend on energy. We have also introduced the number of photons per annihilation \mathcal{N}_γ in the energy range ΔE . These experiment-averaged definitions will allow us to formulate the observational sensitivity more accurately. Note that when the resolution angle does not depend much on energy within ΔE , then $\overline{J} \simeq J$ and $\overline{\mathcal{J}} \simeq \mathcal{J}$. Independently, if the line-of-sight integral does not vary much within the resolution angle, whatever large may the latter be, then $\overline{\mathcal{J}} \simeq \mathcal{J}$ —this is typically the case at reasonable angular distance from the Galactic center. Finally, one can easily convince oneself that for a pointlike object, $\overline{\mathcal{J}}^{\text{pt}} = \mathcal{J}^{\text{pt}}$ (see Sect. IV D 3).

C. Diffuse emission from the smooth and subhalo components

The total averaged DM contribution to the gamma-ray flux is the sum of the smooth contribution, the global subhalo contribution, and the cross-product (*e.g.* [41],

78]). It can be expressed as

$$\frac{d\phi_{\gamma,X}(E, \psi, \theta_r)}{dE} = \mathcal{S}_X(E) \{ J_\psi^{\text{diff}} \equiv J_\psi^{\text{sm}} + J_\psi^{\text{sub}} + J_\psi^{\text{cross}} \} \quad (31)$$

where we have introduced the total diffuse contribution J_ψ^{diff} , which is the sum of

$$J_\psi^{\text{sm}} = \frac{1}{4\pi} \int_{\delta\Omega_r} d\Omega \int_0^{s_{\text{max}}(\psi)} ds \rho^2(s, \psi) \quad (32a)$$

$$J_\psi^{\text{sub}} = \frac{1}{4\pi} \int_{\delta\Omega_r} d\Omega \int_0^{s_{\text{max}}(\psi)} ds \int dm \frac{dn(s, \psi)}{dm} \times \int dc \xi_t \theta(x_t - \epsilon_t) \quad (32b)$$

$$J_\psi^{\text{cross}} = \frac{1}{2\pi} \int_{\delta\Omega_r} d\Omega \int_0^{s_{\text{max}}(\psi)} ds \int dm \frac{dn(s, \psi)}{dm} \times \int dc m_t \rho_{\text{sm}}(s, \psi) \theta(x_t - \epsilon_t). \quad (32c)$$

All these terms characterize the DM contribution to diffuse gamma rays. Note that in the averaged subhalo contribution J_ψ^{sub} , featuring the differential subhalo number density dn given in Eq. (8), we have actually integrated the contribution of all subhalos assuming that they are pointlike (*i.e.* their tidal radii are contained in the solid angle characterized by the resolution θ_r)—hence the presence of the full ξ_t luminosity function. This is formally an approximation, but a very accurate one in fact because the number of pointlike objects is much larger than the extended ones in the resolution angles we will consider (see Sect. [IV D 2](#)). The Heaviside function allows us to integrate only over those subhalos which have not been destroyed by gravitational tides in our model.

D. Pointlike subhalos

Here we give a practical definition to the concept of pointlike subhalo. To avoid any confusion, we emphasize here that this notion applies to both resolved and unresolved sources, in the observational sense (*i.e.* above and below background).

1. Definition

We start with a geometric definition (see *e.g.* Refs [78, 120]). A subhalo located at a distance s from the observer is considered as pointlike if most of its luminosity is contained in the resolution angle θ_r assumed for the telescope, *i.e.*

$$\frac{\min(r_t, 2r_s)}{s} \leq \sin(\theta_r), \quad (33)$$

where we have used the luminosity radius introduced in Eq. (19), and based on that 96% of the luminosity is contained within $2r_s$ for NFW (sub)halos [see Eq. (17)].

Trading the scale radius for a combination of the virtual (virial) mass m and the concentration c , this inequality relation for the tidal radius becomes an inequality relation for the (virial, not tidal) mass, reading

$$m \leq m_{\text{pt}}^{\text{max}}(s, c, x_t) \equiv \frac{4\pi}{3} (200 \rho_c) \left\{ \frac{c s \sin(\theta_r)}{\min(x_t, 2)} \right\}^3 \quad (34)$$

This relation only tells us that the probability for a subhalo to be pointlike increases with its concentration, its distance to the observer, or a combination of both. It allows us to define a maximal mass $m_{\text{pt}}^{\text{max}}$ that depends on that distance and on the subhalo properties. Remember that the dimensionless tidal radius x_t is a function of position and concentration in our model, $x_t(R(s, \psi), c)$. That can further be rephrased in terms of virial (virtual) radius as

$$r_{200}(m) \leq \frac{c s \sin(\theta_r)}{\min(x_t, 2)} \approx \frac{c s \theta_r}{2} \\ \Leftrightarrow r_s(m, c) \lesssim \frac{s \theta_r}{2}, \quad (35)$$

Since we only consider resolution angles such that $\sin(\theta_r) \sim \theta_r \ll 1$, we can see that the size of a pointlike subhalo is always much smaller than its distance to the observer.

2. Number of pointlike subhalos

It is instructive to compute the fraction f_ψ^{pt} of pointlike subhalos lying in the solid resolution angle $\delta\Omega_r$ in any direction ψ in the sky. Given the subhalo parameter space introduced in Sect. [III A](#) and the definition introduced in the previous paragraph, then

$$f_\psi^{\text{pt}} = \frac{\int_{\{m \leq m_{\text{pt}}^{\text{max}}(s, c)\}} d\hat{\sigma} \hat{p}_t(R(s, \psi), m, c)}{\int_{\{m \leq m_{\text{max}}\}} d\hat{\sigma} \hat{p}_t(R(s, \psi), m, c)} \quad (36)$$

$$\text{with } d\hat{\sigma} \equiv s^2 ds \sin \theta d\theta d\phi dm dc. \quad (37)$$

We have used Eq. (22) to define the full phase-space volume element $d\hat{\sigma}$ about the line of sight. It is easy to understand that $f_\psi^{\text{pt}} \simeq 1$ for all angles ψ and for the resolution angles we consider, just because the volume where most subhalos would appear as extended is strongly confined around the observer. This is shown in the right panel of Fig. 2, where we have evaluated this fraction (more precisely $1 - f_\psi^{\text{pt}}$) numerically as a function of the line-of-sight angle ψ for different assumptions on the minimal subhalo mass, the initial mass index α , and the tidal disruption efficiency ϵ_t .

3. J factor for a single object

If a subhalo of mass $m_{t,i}$ is pointlike, located at a distance $s_i \gg r_t$, its J factor $J_{\psi,i}^{\text{pt}}$ should actually account

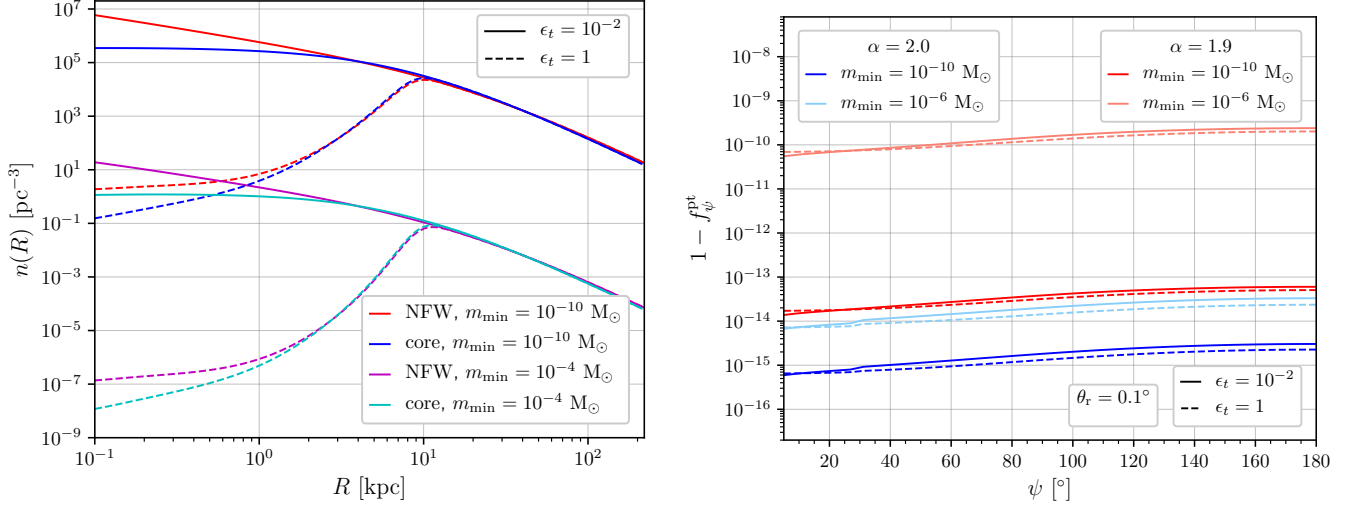


FIG. 2. **Left panel:** Radial distribution of the number density of subhalos assuming a function mass slope of $\alpha = 1.9$, different lower cutoff masses, for subhalos either resilient ($\epsilon_t = 0.01$) or fragile ($\epsilon_t = 1$) against tidal disruption. **Right panel:** Total fraction of extended subhalos per solid angle as a function of the line-of-sight angle ψ , for different mass functions and cutoff masses. As expected, the fraction of pointlike subhalos $f_{\psi}^{\text{pt}} \simeq 1$, such that the fraction of extended objects ($1 - f_{\psi}^{\text{pt}} \ll 1$).

for the fact that its occupancy volume δV_i , assumed centered about the line of sight and characterized by an angular radius equal to or smaller than the considered experimental resolution angle, contains both the subhalo density and the smooth halo density. This should lead to

$$J_{\psi,i}^{\text{pt}/\delta V_i} = J_{\psi,i}^{\text{pt}} + J_{\psi,i}^{\text{sm}} + J_{\psi,i}^{\text{cross}}, \quad (38)$$

where

$$J_{\psi,i}^{\text{pt}} \equiv J_{\psi,i}^{\text{pt}}(m, c, s_i) = \frac{\xi_t}{4\pi s_i^2} \quad (39a)$$

$$\begin{aligned} J_{\psi,i}^{\text{sm}} &\equiv \frac{1}{4\pi} \int d\Omega \int_{\vec{s} \in \delta V_i} ds \rho_{\text{sm}}^2(R(s, \psi)) \\ &\simeq \frac{\rho_{\text{sm}}^2(R(s_i, \psi)) \delta V_i}{4\pi s_i^2} \end{aligned} \quad (39b)$$

$$\begin{aligned} J_{\psi,i}^{\text{cross}} &\equiv J_{\psi,i}^{\text{cross}}(m, c, s_i) \\ &= \frac{1}{2\pi} \int d\Omega \int_{\vec{s} \in \delta V_i} ds \rho_{\text{sm}}(R(s, \psi)) \rho(s) \\ &\simeq \frac{\rho_{\text{sm}}(R(s_i, \psi)) m_{t,i}}{2\pi s_i^2}. \end{aligned} \quad (39c)$$

The smooth contribution $J_{\psi,i}^{\text{sm}}$ is actually already included in the foreground contribution of the smooth halo, so we can formally remove it. Besides, since the DM mass density at the border of the subhalo is always such that $\rho(r_{t,i}) > \rho_{\text{sm}}(R(s_i, \psi))$ as a consequence of tidal stripping [41], we always have $J_{\psi,i}^{\text{pt}} \gg J_{\psi,i}^{\text{cross}} \gg J_{\psi,i}^{\text{sm}}$. Therefore, in the following, we only consider

$$J_{\psi,i}^{\text{pt}/\delta V_i} = J_{\psi,i}^{\text{pt}} = J_i^{\text{pt}} \quad (40)$$

for the J factor associated with a pointlike subhalo, which is precise at the subpercent level. Note that for a point

source, we also have $J_i^{\text{pt}} = \overline{J_i^{\text{pt}}}$, where \overline{J} , defined in Eq. (30), involves an average over the experimental acceptance. The associated gamma-ray flux is simply given by

$$\frac{d\phi_{\gamma,i}(E)}{dE} = \mathcal{S}_{\chi}(m_{\chi}, E) J_i^{\text{pt}}, \quad (41)$$

consistently with Eq. (26).

4. Statistical properties of pointlike subhalo J factors

In order to assess the possibility of detecting subhalos as pointlike sources, we have to derive the full statistical properties of J_{ψ}^{pt} . They are obviously related to the properties of subhalos themselves, which are encoded in the global pdf \hat{p}_t introduced in Eq. (11). However, now, the parameter space becomes limited by the maximal mass $m_{\text{pt}}^{\text{max}}$ attainable by a pointlike object, and defined in Eq. (34). Actually, given a resolution angle θ_r and a line-of-sight angle ψ , the differential probability $d\mathcal{P}_J^{\text{pt}}$ for a subhalo to have a J factor equal to J^0 can be formally expressed as

$$\begin{aligned} \frac{d\mathcal{P}_J^{\text{pt}}}{dJ_{\psi}}(J_{\psi}^0) &= \int_{\{m \leq m_{\text{pt}}^{\text{max}}(s, c)\}} d\hat{\sigma} \hat{p}_t(R(s, \psi), m, c) \\ &\quad \times \delta(J_{\psi}(s(R, \psi), m, c) - J_{\psi}^0). \end{aligned} \quad (42)$$

The volume element $d\hat{\sigma}$ about the line of sight was introduced in Eq. (37). One can then define the integrated

probability to have a J factor larger than some value as

$$\begin{aligned} \mathcal{P}_J^{\text{pt}}(J_\psi^{\text{pt}} \geq J_\psi^0) &= \int_{\{m \leq m_{\text{pt}}^{\text{max}}(s,c)\}} d\hat{\sigma} \hat{p}_t(R(s, \psi), m, c) \\ &\quad \times \theta(J_\psi^{\text{pt}}(s(R, \psi), m, c) - J_\psi^0) \\ &= \int_{J_\psi^0}^{\infty} dJ' \frac{d\mathcal{P}_J^{\text{pt}}}{dJ_\psi}(J'). \end{aligned} \quad (43)$$

Note that $\mathcal{P}_J^{\text{pt}}(J_\psi^{\text{pt}} \geq 0) < 1$ because it defines the probability in the ψ direction only. It normalizes to unity only after integration over the full sky. In the left panel of Fig. 3, we show the shapes of these pdfs assuming line-of-sight angles of $\psi = 20^\circ$ and 90° , the former being optimal for subhalo searches and the later possibly minimizing the foreground. We also considering two minimal virial subhalo masses, $m_{\text{min}} = 10^{-10} M_\odot$ and $10^{-4} M_\odot$, for a conservative initial mass function index $\alpha = 1.9$. Here, the subhalo population is embedded in a global NFW halo. We also anticipate as a green vertical band a range of threshold J factors that expresses the sensitivity of a Fermi-like experiment for 100 GeV DM particles annihilating in $\tau^+ \tau^-$ in an observation time of 10 yr. This will be discussed extensively in Sect. V, notably in Sect. VC.

This plot illustrates the nontrivial dependence of the $\mathcal{P}_J^{\text{pt}}$ on the pointing angle, characterized by a sharp decrease beyond a given J at small angles, which can be associated with the ring structure arising within $\sim 50^\circ$ from the GC (we shall discuss this in more details later when reaching Fig. 5). This transition just reflects the position of the peak in the number density arising from the inner regions of the MW, close to the solar circle, as shown in Fig. 2. This peak corresponds to the region where tidal effects start depleting the subhalo population beyond the peak of the concentration pdf associated with the smallest objects, hence the dramatic decline of subhalos inward. On the other hand, around this peak is where subhalos are still both numerous enough and highly concentrated. One can integrate subhalos over this peak within $\sim 50^\circ$ from the GC (corresponding to a height of ~ 10 kpc from the GC), which explains this particular feature in $\mathcal{P}_J^{\text{pt}}$. Much less important than it seems is the difference of probability amplitude between $m_{\text{min}} = 10^{-10} M_\odot$ and $10^{-4} M_\odot$, which only comes from the fact that the total number of subhalos scales like $\propto 1/m_{\text{min}}$ (hence the 6 orders of magnitude between the amplitudes); once rescaled by the total number of subhalos, the pdfs actually match with one another very well (except, obviously, for the very low J_ψ^0 tail, not appearing in the plot).

The right panel of Fig. 3 shows the same results in terms of the number of pointlike subhalos with J factors larger than a threshold J_0 as a function of J_0 , still for a subhalo population embedded in a global NFW halo. We report the number distributions obtained with different line-of-sight angles ψ , and in the bottom frame, we also indicate the relative difference when assuming subhalos

embedded either in an NFW or in a cored global DM halo. We see that the global cored DM halo configuration generically leads to more visible subhalos, Except in the range of $J \in \sim [10^{18}, 10^{19}] \text{ GeV}^2/\text{cm}^5$, which just reflects the fact that the sharp decrease in $\mathcal{P}_J^{\text{pt}}$ for a cored host halo occurs at lower values of J .

From these pdfs, one can also calculate the n th moments of the J factors (including the mean value with $n = 1$) using

$$\langle (J_\psi^{\text{pt}})^n \rangle = \int_0^\infty dJ (J)^n \frac{d\mathcal{P}_J^{\text{pt}}}{dJ_\psi}(J). \quad (44)$$

V. DETECTABILITY OF SUBHALOS AS POINTLIKE SOURCES

This section enters the prevailing discussion of the paper: assessing the detectability of pointlike subhalos. To proceed, we need to carefully define what are the main foregrounds or backgrounds (generically *background* henceforth) to any potential detection. In most past studies, the main background considered was the “baryonic” contribution to the γ -ray flux. This comprises the diffuse Galactic emission (DGE) induced by interactions of cosmic rays with the interstellar gas or radiation (pion production, bremsstrahlung, and inverse Compton processes) and by unresolved conventional Galactic sources, and the isotropic diffuse extragalactic background. A lot of effort has been invested in describing the sensitivity of current gamma-ray experiments to exotic pointlike sources based on as accurate as possible models of such Galactic and extragalactic backgrounds, inferred from both phenomenological cosmic-ray modeling, or from more agnostic template fitting methods [58, 59, 62, 65, 66]. Here, by contrast, we consider a very simplified model of baryonic background, and instead focus our attention onto another background component often neglected, *i.e.* the one induced by DM annihilation itself, which is made up of contributions from the smooth halo and from unresolved subhalos. That DM background has already been defined in Sect. IV C.

We further want to place ourselves within the framework of an idealized Fermi-LAT-like experiment, in which we assume that a diffuse emission has been measured in predefined regions of interest (ROIs), which is consistent, while not perfectly, with the baryonic foreground (hence limiting the diffuse DM contribution to statistical or systematic fluctuations at maximum). This will allow us to set idealized limits on the contribution of DM annihilation to the diffuse emission, hence on the annihilation cross section, which also impacts on the detectability of DM subhalos.

In Sect. VA, we provide the details of our background model. In Sect. VB, we describe the statistics of the number of pointlike subhalos contributing a flux above a given threshold. In Sect. VC, we review the full statistical analysis we perform to infer the sensitivity to point-

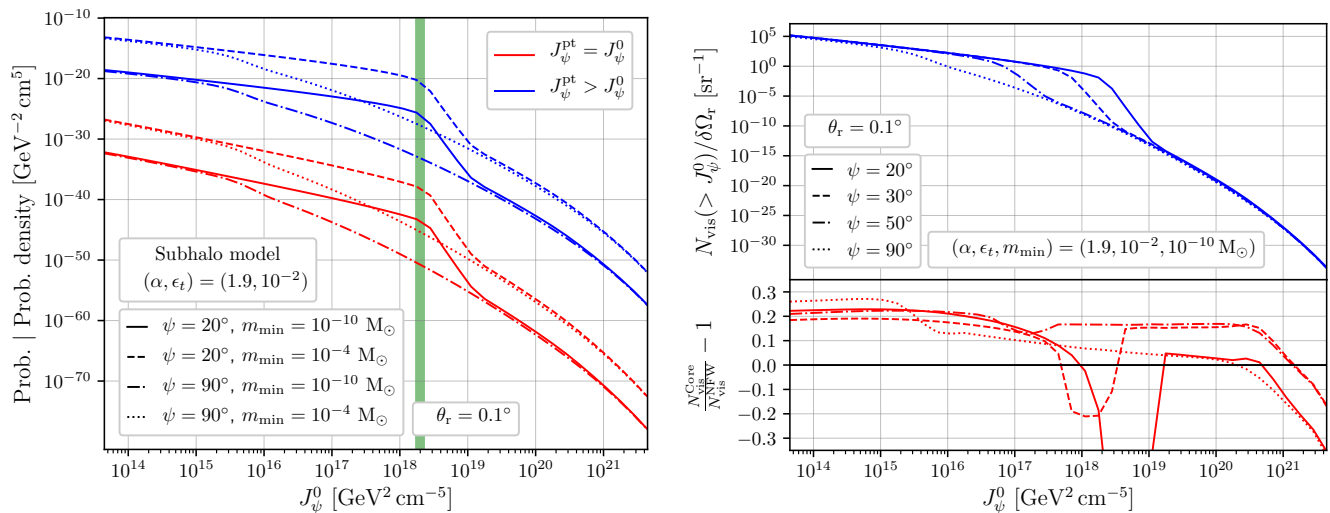


FIG. 3. **Left panel:** Probability distribution functions $d\mathcal{P}_J^{\text{pt}}(J)/dJ_\psi$ (differential) and $\mathcal{P}_J^{\text{pt}}(J_\psi^{\text{pt}} \geq J)$ (integrated), for a resolution angle $\theta_r = 0.1^\circ$, line-of-sight angles $\psi = 20^\circ$ (intermediate latitude) and $\psi = 90^\circ$ (Galactic pole), and a subhalo population configuration of resilient subhalos with $(\alpha, m_{\text{min}}, \epsilon_t) = (1.9, 10^{-10} - 10^{-4}, 0.01)$ embedded in an NFW Galactic halo. The green vertical thick line gives the typical sensitivity for a Fermi-LAT-like experiment calculated for an observation time of 10 yr. **Right panel:** Corresponding distribution of the number of subhalos with J factors larger than J_0 as a function of J_0 , for different line-of-sight angles. The bottom part of the plot shows the relative difference when using a subhalo population model embedded in a cored Galactic halo.

like subhalos in our idealized framework. We start with a simplified statistical reasoning (see Sect. VC2), which allows us to derive useful analytical results for the threshold flux of subhalo detection as a function of time and annihilation cross section. Most notably, we derive useful time-independent asymptotic limits arising in the case of infinite observational time, which correspond to the most optimistic case for the detection of DM subhalos. Finally, we generate mock data and apply a complete likelihood analysis (i) to mimic the current Fermi data analysis, (ii) to qualitatively validate the aforementioned simplified statistical reasoning, and (iii) to get more definite results for the detectability of subhalos. We discuss these results in Sect. VC4.

A. Baryonic background model

We consider two types of contributions to the diffuse background that may shield DM subhalos as individual sources: one coming from DM annihilation itself, already discussed in Sect. IVC, and another one coming from conventional astrophysical processes, dubbed baryonic background (including both the DGE and the isotropic background). To maximize the self-consistency of our study, we base our DGE baryonic background model on the same ingredients used to determine the tidal stripping induced by the baryonic disk, *i.e.* those included in the Galactic mass model derived from kinematic data in Ref. [76]. They consist of the spatial distributions for the atomic and molecular interstellar gas. We remind

the reader that our goal is to have a realistic modeling of the background, though not necessarily a precise one. Indeed, we shall not discuss the Fermi data themselves, but instead provide a realistic insight as to what to expect to find in them in terms of any putative subhalo contribution.

For space-borne observatories like Fermi-LAT [121], the genuine background includes many different astrophysical contributions, as shortly stated above. However, for simplicity, we restrict ourselves to the pion decay contribution induced by the interactions of cosmic rays with the interstellar gas, which is the dominant DGE one in the 1 – 100 GeV energy range that we consider [122]. There are of course other contributions (e.g. leptonic), but the spatial distribution of their amplitudes should not change much with respect to the pion decay one—we will play with the overall normalization of the “pionic” background for a better match, but this will anyway not be critical in our analysis. We add by hand the isotropic diffuse emission assumed to be of extragalactic origin, for which we simply consider the spectrum derived in Ref. [122]. In the following, we only consider gamma-ray energies above 1 GeV, to avoid modeling issues with the pion bump at ~ 100 MeV.

Consistently with our Galactic mass model, we can predict the relative intensity of the pionic emission by convoluting of a cosmic-ray flux, assumed homogeneous in the MW for simplicity, and the spatial-dependent hydrogen number density, n_{ism} . The latter can be expressed

as

$$n_{\text{ism}}(\vec{x}) = n_{\text{H}}(\vec{x}) + 2 n_{\text{H}_2}(\vec{x}) = \frac{\rho_{\text{H}}(\vec{x})}{m_{\text{H}}} + 2 \frac{\rho_{\text{H}_2}(\vec{x})}{m_{\text{H}_2}}, \quad (45)$$

where indices H and H₂ refer to atomic and molecular hydrogen, respectively, m_{H/H_2} being their masses, and where, consistently with the SL17 subhalo model, we take the associated gas mass densities ρ 's from McM17. Further integrating this density along the line of sight, within a resolution solid angle $\delta\Omega_{\text{r}}$, we get

$$\begin{aligned} \left\langle \frac{d\phi_{\pi}(E, l, b)}{dE d\Omega} \right\rangle_{\delta\Omega_{\text{r}}} &= \frac{f_{\pi}(E)}{4\pi \delta\Omega_{\text{r}}} \int_{\delta\Omega_{\text{r}}} d\Omega \int ds n_{\text{ism}}(s, l, b) \\ &\simeq \frac{f_{\pi}(E)}{4\pi} \int ds n_{\text{ism}}(s, l, b), \end{aligned} \quad (46)$$

where l and b are the longitude and latitude, respectively. The spectral function $f_{\pi}(E)$ is taken as a power law over three energy ranges,

$$\begin{aligned} f_{\pi}(E) &= \sum_{i=1}^3 \theta(E - E_{\text{max}}^{(i-1)}) \theta(E_{\text{max}}^{(i)} - E) \\ &\quad \times f_0^{(i)} \left[\frac{E}{1 \text{ GeV}} \right]^{-\gamma_{\text{b}}^{(i)}}, \end{aligned} \quad (47)$$

where the normalization coefficients $f_{0,i}$ and spectral indices $\gamma_{\text{b},i}$ are tuned to give a decent fit to the pionic contribution estimated in Ref. [122]. Starting from a threshold energy $E_{\text{min}} = E_{\text{max},0} = 1 \text{ GeV}$, these parameters read:

$$\left[\begin{array}{c} E_{\text{max}}^{(i)} \\ \text{GeV} \\ \gamma_{\text{b}}^{(i)} \\ f_0^{(i)} \\ 10^{-27} \text{ GeV}^{-1} \text{ s}^{-1} \end{array} \right] = \begin{cases} (i=1) \rightarrow \begin{bmatrix} 1.4 \\ 2.27 \\ 6.69 \\ 2.3 \\ 7.45 \end{bmatrix} \\ (i=2) \rightarrow \begin{bmatrix} 2.59 \\ 2.72 \\ 8.31 \end{bmatrix} \\ (i=3) \rightarrow \begin{bmatrix} 100 \end{bmatrix} \end{cases} \quad (48)$$

The latitudinal profiles of this pionic gamma-ray flux background model integrated over two energy ranges, [1.6-13] GeV and [13-100] GeV are shown in Fig. 4 as solid red curves (top and bottom panels, respectively), for both the central and anticentral Galactic regions (left and right panels, respectively), and are compared with the ones inferred from the Fermi-LAT data and taken from Ref. [122] (dashed red curves for the pionic contribution, and dashed blue for the total DGE). We also show our pionic background model rescaled by a constant factor in the range 1.5-2.5 (redish shaded bands), and the corresponding residuals with respect to the total DGE inferred from the Fermi-LAT data. We see that our DGE

model of both the Fermi-LAT reconstructed pionic emission and of the total DGE are reasonably recovered both in the central regions and in the outskirts of the MW, with errors in amplitude fluctuating by a factor of ~ 2 . This angular gradient is realistic enough for our study. Since we want to remain on the optimistic side regarding the detection of subhalos, we adopt a rescaling factor $\alpha_{\pi \rightarrow \text{DGE}}$ such that our background DGE model does not exceed current data, and therefore fix it to 1.5 from now on. We have checked that our results are qualitatively not sensitive to slight changes around this value.

Our full baryonic background flux is then given by

$$\begin{aligned} \left\langle \frac{d\phi_{\text{b}}(E, l, b)}{dE d\Omega} \right\rangle_{\delta\Omega_{\text{r}}} &= \alpha_{\pi \rightarrow \text{DGE}} \left\langle \frac{d\phi_{\pi}(E, l, b)}{dE d\Omega} \right\rangle_{\delta\Omega_{\text{r}}} \\ &\quad + \left\langle \frac{d\phi_{\text{iso}}(E, l, b)}{dE d\Omega} \right\rangle_{\delta\Omega_{\text{r}}}, \end{aligned} \quad (49)$$

where ϕ_{iso} is the isotropic component that we directly extract from Ref. [122]. We have explicitly introduced the tuning parameter $\alpha_{\pi \rightarrow \text{DGE}}$, which will be further altered later to mimic additional systematic uncertainties or missing sources of background.

To conservatively match with the constrained DGE, we assume $\alpha_{\pi \rightarrow \text{DGE}} = 1.5$ unless specified otherwise. This allows our DGE background model never to exceed the genuine one, especially at large latitudes where mismodeling errors in the real data analysis are expected to be less important. This is at the cost of underestimating the DGE background by up to a factor of ~ 2 in some regions of the sky, which we will comment on in the final discussion but which anyway positions our forthcoming mock data analysis in the rather optimistic configuration as far as subhalo detection is concerned.

B. Number of subhalos above threshold and associated probability

Before entering the details of the determination of the sensitivity to pointlike subhalos in our idealized model, hence of the detection threshold in terms of gamma-ray flux, it is useful to describe how we can translate a sensitivity estimate into a number of observable subhalos and associated probability. For given DM particle mass, annihilation cross section and channel, the gamma-ray flux is fully determined by the J factor (see Eq. 41). Therefore the sensitivity to pointlike subhalos can be expressed in terms of a minimal J factor that we call J_{min} . Since the background is not isotropic, $J_{\text{min}} = J_{\text{min}}(l, b) = J_{\text{min}}^{(l,b)}$.

The integrated probability for a pointlike subhalo to have a J factor larger than $J_{\text{min}}^{(l,b)}$ in the direction characterized by the angle $\psi(l, b)$ such that $\cos \psi = \cos b \cos l$ is given in Eq. (43), for a resolution solid angle $\delta\Omega_{\text{r}}$ —see also Fig. 3. We can further integrate this probability over the full sky, accounting for the fact that J_{min} depends on

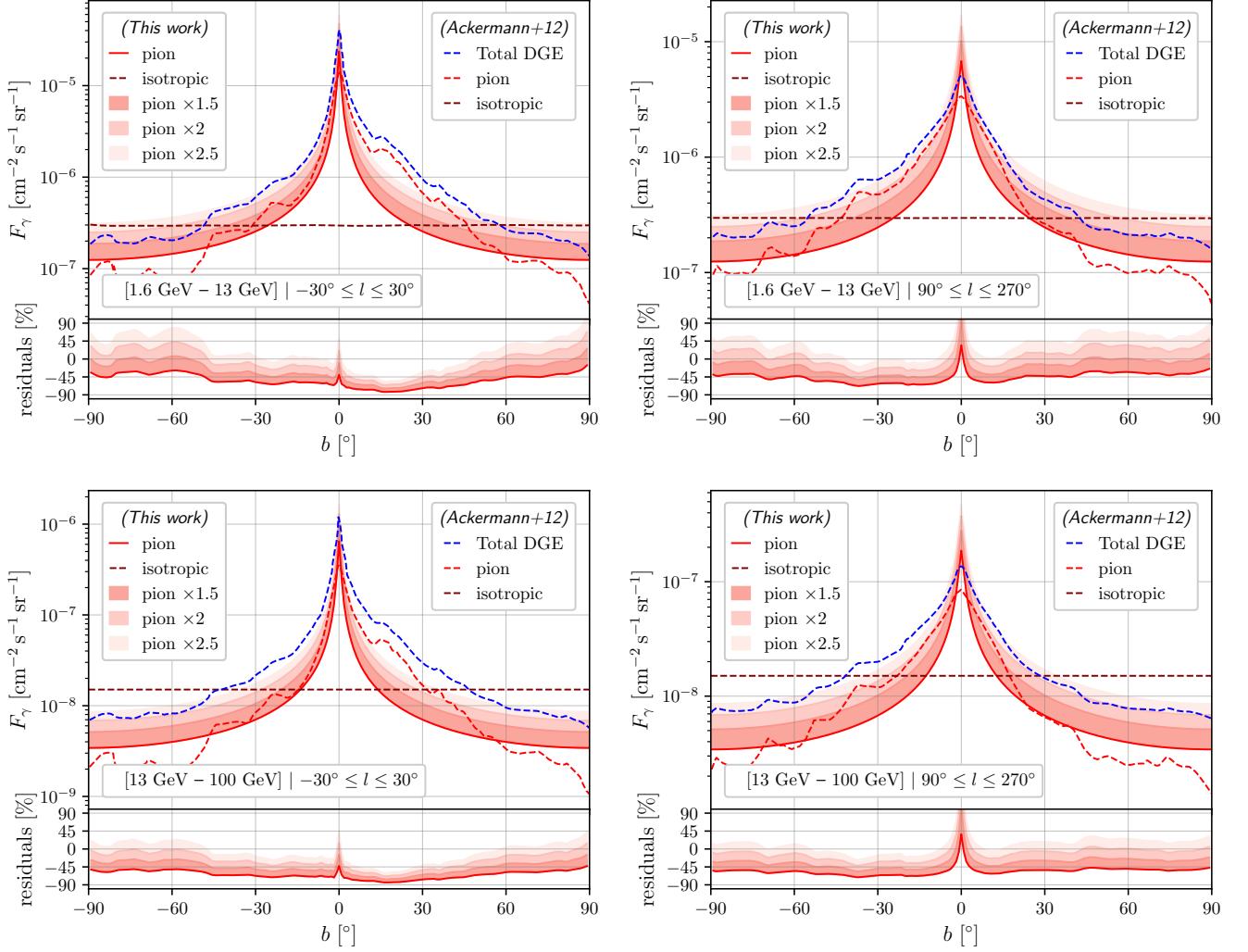


FIG. 4. **Left panels:** Latitudinal profiles calculated from the flux given Eq. (46) and integrated over two energy ranges, [1.6-13] GeV (top left panel) and [13-100] GeV (bottom left panel), and averaged in the inner galactic longitudinal range $-30^\circ \leq l \leq 30^\circ$. The model (solid curves) is compared with the Fermi data (dashed red curves for the pionic emission, dashed blue curves for the total DGE). At the bottom of each plot, we show the residuals of our rescaled pionic model (redish shaded bands) with respect to the total DGE inferred from the data. We also report the isotropic gamma-ray flux (brown dashed curves), for which our model is tuned to the one inferred from the data. **Right panels:** Same as in the left panel, but averaged in the outer longitudinal range $90^\circ \leq l \leq 270^\circ$.

the pointing angle. We get

$$P_{\text{vis}}^{\text{pt}} = \int db \cos b \int dl P_J^{\text{pt}}(J_\psi^{\text{pt}} \geq J_{\text{min}}^{(l,b)}) \quad (50)$$

Here, $P_{\text{vis}}^{\text{pt}}$ is normalized by construction in such a way that it is 1 for $J_{\text{min}}^{(l,b)} = 0$. From now on, we denote this probability p .

Given a total number of pointlike subhalos $N_{\text{pt}} \simeq N_{\text{tot}}$, the probability to detect k subhalos is given by the binomial probability

$$P(k|N_{\text{pt}}) = \binom{N_{\text{pt}}}{k} p^k (1-p)^{N_{\text{pt}}-k}. \quad (51)$$

Since in realistic situations we expect $k \ll N_{\text{pt}}$ and

$N_{\text{pt}} \gg 1$, we can use the Poissonian limit of the previous equation,

$$P(k|N_{\text{pt}}) \simeq \frac{\nu^k}{k!} e^{-\nu} \quad \text{with } \nu \equiv N_{\text{pt}} p. \quad (52)$$

Therefore the probability to observe at least n objects is given by

$$P(\geq n|N_{\text{pt}}) \simeq 1 - \sum_{i=0}^{n-1} P(i|N_{\text{pt}}). \quad (53)$$

We can further consider the cumulative of the probability given in Eq. (52) by promoting k to a real number x , such

that

$$P_x(x|N_{\text{pt}}) = e^{-\nu} \sum_{k=0}^{\lceil x \rceil - 1} \frac{\nu^k}{k!} = \frac{\Gamma(\lceil x \rceil, \nu)}{\Gamma(\lceil x \rceil)}, \quad (54)$$

where the Γ functions in the denominator and in the numerator are the standard and incomplete gamma functions, respectively. We can then define a confidence interval at $100(1 - c)\%$ that x be measured in the range $[N_c^-, N_c^+]$ by solving

$$\frac{c}{2} = \frac{\Gamma(N_c^- + 1, \nu)}{\Gamma(N_c^- + 1)} = 1 - \frac{\Gamma(N_c^+, \nu)}{\Gamma(N_c^+)}. \quad (55)$$

In the following, we use this formalism to determine the number of subhalos that could be observed with a Fermi-LAT-like observatory. The fundamental quantity that should now be characterized is the minimal J factor, $J_{\text{min}}^{(l,b)}$, that we address below.

C. Sensitivity to pointlike subhalos

1. Specifications of our virtual Fermi-LAT-like instrument and of our DM benchmarks

Since we wish to address the potential of Fermi-LAT or any other similar experiment to detect subhalos, we first have to fix the main specifications that will be used to make predictions. These specifications need not match exactly those of Fermi-LAT, but need to be close enough to be quantitatively realistic⁴. We do not seek for percent precision, but rather order 1 precision in terms of subhalo searches. We can therefore simplify the experimental characteristics such that they can be manipulated with ease at the level of calculations. Consequently, in the following, unless specified otherwise, we assume:

- a search energy window⁵ of [1-100] GeV with a flat effective area \mathcal{A} of 0.9 m², and a field of view of 1/5 of the sky (consistent with the acceptance of ~ 2.3 m²sr quoted in [124, 125], and with the exposure of $2.7\text{-}4.5 \times 10^{11}$ cm²s = 0.86-1.43 m²yr quoted in the fourth Fermi catalog and corresponding to 8 yr of data taking [59]);
- two benchmark resolution angles of $\theta_r = 0.1^\circ$ and 1° , with the latter to very roughly address the search for extended subhalos;
- a uniform coverage of the sky.

For WIMP DM, we assume a default canonical s-wave thermal annihilation cross section fixed to $\langle\sigma v\rangle = 3 \times 10^{-26}$ cm³/s (neglecting changes with the WIMP mass, see *e.g.* [126, 127]), and consider the $b\bar{b}$ or $\tau^+\tau^-$ annihilation channels using the spectral tables provided in Ref. [123].

2. A simplified but helpful warm-up statistical analysis

We start with a very simple statistical method based on On-Off event number counting [128]. Given the gamma-ray fluxes for a pointlike source and associated background, we can very roughly define the sensitivity in terms of rudimentary Poisson statistics [128–131]. For a subhalo of index i located at position \vec{s}_i in the observer's frame, and characterized by an angle ψ_i and Galactic coordinates (s_i, l_i, b_i) , with $\cos \psi_i = \cos b_i \cos l_i$, we can estimate the number of gamma-ray events N_γ^i collected in an arbitrary energy range ΔE by a telescope of time-area efficiency set by the effective collection area \mathcal{A} and observation time \mathcal{T}_{obs} . Neglecting for simplicity dependencies other than on energy for the effective collection area, this number of events reads

$$N_\gamma^i(l_i, b_i, \Delta E) = \Delta E \left\langle \frac{dR^i}{dE} \right\rangle \mathcal{T}_{\text{obs}}^i, \quad (56)$$

with

$$\begin{aligned} \left\langle \frac{dR^i}{dE} \right\rangle &\equiv \overline{\mathcal{A}} \mathcal{S}_\chi(m_\chi, \langle\sigma v\rangle, \Delta E) J_i \\ &= \frac{\langle\sigma v\rangle \langle \mathcal{N}_\gamma \mathcal{A} \rangle_{\Delta E}}{2 m_\chi^2 \Delta E} J_i. \end{aligned} \quad (57)$$

We have introduced the differential event rate dR/dE . The flux factor J_i is given by Eq. (40), and the spectral function \mathcal{S}_χ by Eq. (25), with the effective collection area \mathcal{A} . Since this expression is for a point source, J_i needs not be modified by the average over the experimental acceptance [see discussion below Eq. (39)].

Similarly, the number of background events is given by

$$N_\gamma^{\text{bg}}(l_i, b_i, \Delta E) = \Delta E \left\langle \frac{dR^{\text{bg}}}{dE} \right\rangle \mathcal{T}_{\text{obs}}^{\text{bg}}, \quad (58)$$

with the background rate averaged over ΔE

$$\begin{aligned} \left\langle \frac{dR^{\text{bg}}}{dE} \right\rangle &\equiv \frac{1}{\Delta E} \int_{\Delta E} dE \int_{\delta\Omega_r(E)} d\Omega \frac{d\phi_\gamma^{\text{bg}}(E, l_i, b_i)}{dE d\Omega} \mathcal{A}(E) \\ &\simeq \frac{\pi \theta_r^2}{\Delta E} \int_{\Delta E} dE \frac{d\phi_\gamma^{\text{bg}}(E, l_i, b_i)}{dE d\Omega} \mathcal{A}(E). \end{aligned} \quad (59)$$

Again, we have assumed that the angular efficiency is flat and maximal within the energy-dependent angular resolution $\theta_r(E)$ of the instrument, such that $\Theta(\theta_r(E) - \theta)$ can be traded for the solid angle domain $\delta\Omega_r(E)$. The latest approximated equation assumes a vanishingly small energy-independent resolution angle and that the background flux varies by less than a statistical fluctuation

⁴Details can be found on the dedicated [Fermi-LAT](#) webpage.

⁵We restrict ourselves to a limited energy range where the effective area is constant. A maximum of 100 GeV allows a reach in WIM mass of ~ 300 GeV (~ 2 TeV) for an annihilation in $\tau^+\tau^-$ ($b\bar{b}$) [65, 119, 123].

within this angle. In that case the angular integral factorizes out, giving $2\pi(1 - \cos\theta_r) \simeq \pi\theta_r^2$. In the following, we actually neglect the energy dependence of θ_r for the sake of simplicity, and because it has negligible impact on our results (it would have impact in studies of the Galactic center emission).

Without loss of generality, a pointlike source can be detected (or resolved, equivalently) when the number of signal events becomes larger than some threshold number n_σ times the Poissonian fluctuation of background events, assuming the same exposure for both the signal and background. This can be expressed as

$$\frac{N_\gamma^i(l_i, b_i, \Delta E)}{\sqrt{N_\gamma^{\text{bg}}(l_i, b_i, \Delta E)}} > n_\sigma. \quad (60)$$

We can actually artificially absorb any exposure difference between the target and reference background in the number of fluctuations n_σ , which should then be thought of as an effective threshold number of order $\sim 1-10$ [128]. In the classical case of exact Poisson statistics with equal on- and off-source exposure, a detection threshold corresponds to $n_\sigma \geq 5$. From the above equation, we can define a minimal J factor for a pointlike subhalo to be detected as follows:

$$\begin{aligned} J_{\min}^{(l,b)}(\Delta E, m_\chi, \langle\sigma v\rangle) &= \frac{n_\sigma}{T_{\text{obs}}} \frac{\sqrt{N_\gamma^{\text{bg}}(l, b, \Delta E)}}{\mathcal{A}\mathcal{S}_\chi(m_\chi, \langle\sigma v\rangle, \Delta E)} \quad (61) \\ &= \frac{n_\sigma}{\sqrt{T_{\text{obs}}}} \frac{2m_\chi^2 \sqrt{\Delta E \left\langle \frac{dR^{\text{bg}}}{dE} \right\rangle}}{\langle\sigma v\rangle \langle\mathcal{N}_\gamma\mathcal{A}\rangle_{\Delta E}}. \end{aligned}$$

This equation explicitly shows that the pointing-direction dependence of $J_{\min}^{(l,b)}$ is only set by that of the background. Even though obvious, this is an important point because in essence, this means that the most visible point-source subhalos (relative to background) may have different internal properties depending on the pointing direction, and are not necessarily the most intrinsically luminous in a background-free setting (detection probability does not necessarily correspond to luminosity probability). The dependence in $\langle\sigma v\rangle$ is rather trivial at first sight since $J_{\min}^{(l,b)}$ simply linearly increases as the annihilation cross section decreases. A quick inspection of the right panel of Fig. 3, which shows the exponentially decreasing number of subhalos as a function of some threshold in J , already tells us that increasing a bit $J_{\min}^{(l,b)}$ can actually have a dramatic impact on the number of visible subhalos: if constraints on $\langle\sigma v\rangle$ get stronger and stronger, the probability to detect subhalos is going to shrink accordingly, but exponentially. However, we will see below that this is less trivial if the constraint is set from the analysis of the diffuse Galactic emission, and if one insists on detecting subhalos before the smooth halo.

Eventually, one can translate $J_{\min}^{(l,b)}$ in terms of a thresh-

old flux

$$\begin{aligned} \phi_{\min}^{(l,b)}(\Delta E) &= \int_{\Delta E} dE \mathcal{S}_\chi(m_\chi, E) J_{\min}^{(l,b)} \quad (62) \\ &\propto \langle\sigma v\rangle J_{\min}^{(l,b)}, \end{aligned}$$

where the integral is performed over an arbitrary energy range ΔE .

3. Impact of different background configurations

The composite nature of the background affects the behavior of the sensitivity to pointlike subhalos. Here we inspect several background configurations still in the framework of the simplified statistical method introduced above. We first consider subhalo searches neglecting the baryonic foreground and accounting only for the smooth DM and unresolved subhalos background emission. Then we do the contrary, *i.e.* neglecting the diffuse DM contribution and considering only baryons. Finally, we study a more realistic background case including both the baryonic and diffuse DM contributions, and further derive the conditions for a subhalo to be detected *before* the diffuse DM component. As we will see, the latter configuration gives rise to asymptotic conditions that do depend neither on the annihilation cross section nor on the observation time. That result will actually be recovered by means of a more sophisticated statistical analysis resembling that used by the Fermi Collaboration.

a. DM-only background model: Neglecting the baryonic background is obviously not realistic, but this allows us to figure out quickly where the most visible subhalos should concentrate in the sky, notably if the smooth halo were to be discovered first. These are not necessarily the most intrinsically luminous, since they still have to contrast with the background. However, in this case, the background is the lowest possible, *i.e.* induced by DM itself (both the smooth halo and unresolved subhalos). That background configuration also leads to a dependence of the sensitivity to pointlike subhalos on the annihilation cross section different from the baryonic background case, which would rather characterize subhalo searches after the detection of the smooth halo. In the DM-only case, the number of background events is given by

$$\begin{aligned} N_\gamma^{\text{bg}}(l, b, \Delta E) &= N_\gamma^{\text{bg/dm}}(l, b, \Delta E) = N_\gamma^{\text{diff}}(l, b, \Delta E) \\ &= \frac{\langle\sigma v\rangle}{2m_\chi^2} \langle\mathcal{N}_\gamma\mathcal{A}\rangle \overline{J_\psi^{\text{diff}}} T_{\text{obs}}^{\text{diff}}, \quad (63) \end{aligned}$$

which implies

$$J_{\min}^{(l,b)} = J_{\min}^\psi \propto \frac{\theta_r}{\sqrt{\langle\sigma v\rangle T_{\text{obs}}}} \Leftrightarrow \phi_{\min}^\psi \propto \theta_r \sqrt{\frac{\langle\sigma v\rangle}{T_{\text{obs}}}}. \quad (64)$$

The number of background events is therefore similar to that of signal events defined in Eq. (56), except for

the J factor of the diffuse DM component $\overline{J_\psi^{\text{diff}}}$, defined in Eqs. (31) and (30). Note that for an energy-independent resolution angle and a flat angular acceptance $\overline{J_\psi^{\text{diff}}} = J_\psi^{\text{diff}}$. Since the diffuse DM background is itself proportional to $\langle\sigma v\rangle$, the threshold J factor J_{min} given in Eq. (61) scales like $1/\sqrt{\langle\sigma v\rangle T}$, and no longer like $1/(\langle\sigma v\rangle\sqrt{T})$, which only holds when the background is independent of the DM annihilation rate. Consequently, paradoxically enough, even though the sensitivity to pointlike subhalos increases as $\langle\sigma v\rangle$ increases (J_{min} decreases—see the right panel of Fig. 3), the pointlike flux sensitivity ϕ_{min} actually degrades because of the brighter background. The additional factor of θ_r arises from the assumption that the diffuse background varies by less than a statistical fluctuation within the resolution angle of the instrument, see Eq. (59). That assumption essentially holds while not pointing toward the Galactic center, and implies that both the subhalo and flux sensitivities degrade (J_{min} and ϕ_{min} increases) when the resolution angle increases simply as a consequence of collecting more background photons.

In the left panels of Fig. 5, we show sky maps of the effective number of visible subhalos per solid angle unit. They are computed using the nominal subhalo population model self-consistently embedded either within an NFW Galactic halo (top panels) or in a cored one (middle panels), and pointlike subhalos were defined by taking a resolution angle of $\theta_r = 0.1^\circ$. Although we consider the DM-only induced diffuse gamma-ray background for the moment, the subhalo population model still includes baryonic tidal stripping. The model parameters are set to $(\alpha, m_{\text{min}}/M_\odot, \epsilon_t) = (1.9, 10^{-10}, 0.01)$. We further assume WIMPs of 100 GeV annihilating into $\tau^+\tau^-$ with the canonical annihilation cross section, and restrict the spectral gamma-ray window to the [1-100] GeV energy range—we define “visible” by demanding $n_\sigma \geq 3$ in Eq. (61), taking an observation time of 10 yr. With this setup, we get < 1 photon in the virtual detector, so the discussion here is only qualitative, and numbers should only be compared relatively between one another. We see that visible subhalos concentrate in a ring around the Galactic center, whose width and peak actually depend on the subhalo sensitivity J_{min}^ψ .

The right panels of Fig. 5 show the corresponding angular distributions as functions of the line-of-sight angle ψ . They also show the results obtained with a broader resolution angle of $\theta_r = 1^\circ$, as well as the impact of changing the mass slope α (1.9 or 2) and the minimal virial mass (10^{-10} or $10^{-4} M_\odot$)—the shaded areas correspond to the 68% and 95% statistical uncertainties, and are derived according to Eq. (55). It appears from these angular projections that in both NFW and cored Galactic halos, potentially visible subhalos for $\theta_r = 0.1^\circ$ are concentrated in a ring about the GC extending up to $\psi \sim 50^\circ$ with a peak around $\psi \sim 30^\circ$ (reddish curves). It also appears that a larger resolution angle of $\theta_r = 1^\circ$ drastically changes this angular distribution (blueish curves) due to

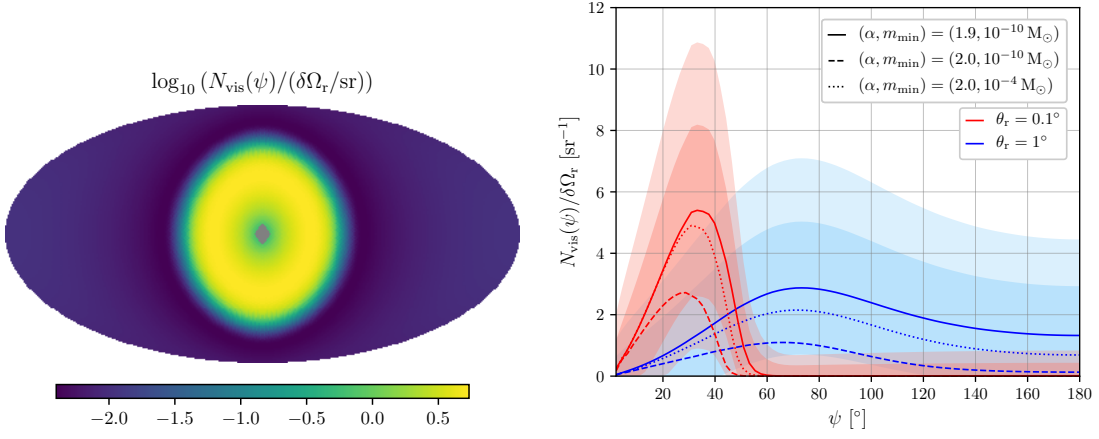
two different effects: (i) as seen from Eq. (64), the sensitivity degrades simply as the detector integrates more background photons; (ii) changing the resolution angle allows bigger (hence intrinsically more luminous) subhalos to become point sources, and bigger subhalos are more efficiently destroyed by gravitational tides in the central Galactic regions. As an outcome, increasing the angular window for individual subhalo searches has the effect of shifting the angular distribution to much larger values of ψ (larger latitude, longitude, or both)—with a very flattened peak now around $\psi \sim 70^\circ$. The precise angular distribution of visible subhalos strongly depends on that of the diffuse background. The latter is affected by unresolved subhalos at large angles, which makes it important to include them as an additional background contribution.

In contrast, changing the global DM halo from an NFW (top panels) to a cored profile (middle panels) does not significantly affect these features, except for enlarging the peaks toward lower angles and slightly flattening them as well (there is less diffuse background in the central regions, but also slightly less subhalos within the halo scale radius). Notice that in the DM-only background configuration, there are more visible subhalos in an NFW Galactic halo than in a cored one. This will actually be reversed when the baryonic foreground is added, which will degrade the sensitivity toward the central Galactic regions. A summary plot of the DM-only background case is presented in the bottom panel of Fig. 5, where the level of background and subhalo sensitivity are varied by tuning $\langle\sigma v\rangle$ instead—see Eq. (64).

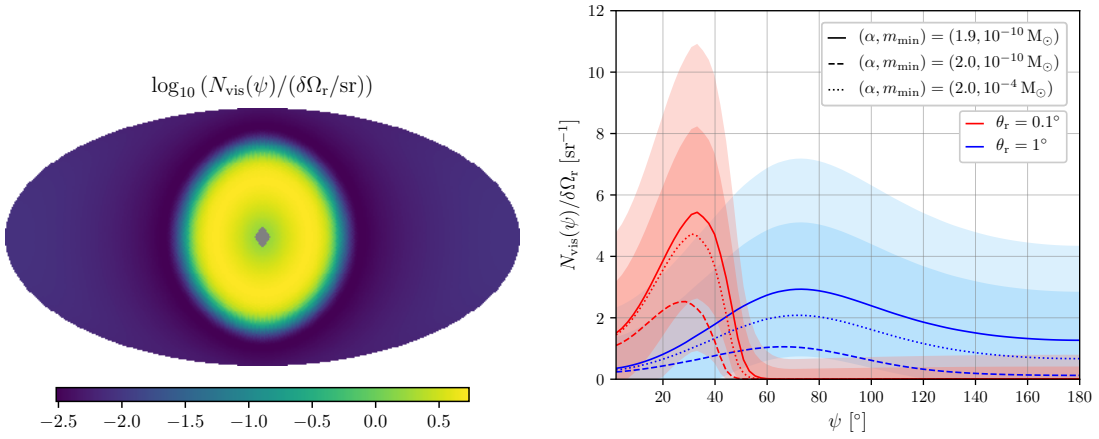
Such trends are consistent with the Monte Carlo results obtained in [77], which instead describe the distribution of the brightest point-source subhalos as a function of distance to the observer. We stress that these are not necessarily the most visible when contrasted with the diffuse background. Our analytical calculations have the advantage of very easily covering the full dynamical range and as many model configurations as necessary, in a very short CPU time.

In the right panels of Fig. 5, we also explore the impact of changing the main subhalo population model parameters by taking different combinations within $(\alpha, m_{\text{min}}/M_\odot, \epsilon_t) = (1.9 - 2, 10^{-10} - 10^{-4}, 0.01)$. It is well known that varying the minimal virial subhalo mass m_{min} has only significant (nonlogarithmic) impact for $\alpha > 1.9$ (see *e.g.* [46, 47, 78]). Therefore, we vary m_{min} only for $\alpha = 2$. This self-consistently keeps the global Galactic halo profile (sum of all components) unchanged once it has been fixed (NFW or cored halo) in the SL17 model, and therefore remains consistent with kinematic constraints by construction. We see that $\alpha = 1.9$ results in significantly more visible pointlike subhalos than $\alpha = 2$. This might look surprising because the number of subhalos is much larger in the latter case, for a given m_{min} . However, there are two compensating effects: (i) there are relatively bigger subhalos (hence more luminous) in the $\alpha = 1.9$ case because the mass function is

NFW Galactic halo - pointlike subhalos in diffuse DM-only background



Cored Galactic halo - pointlike subhalos in diffuse DM-only background



Summary

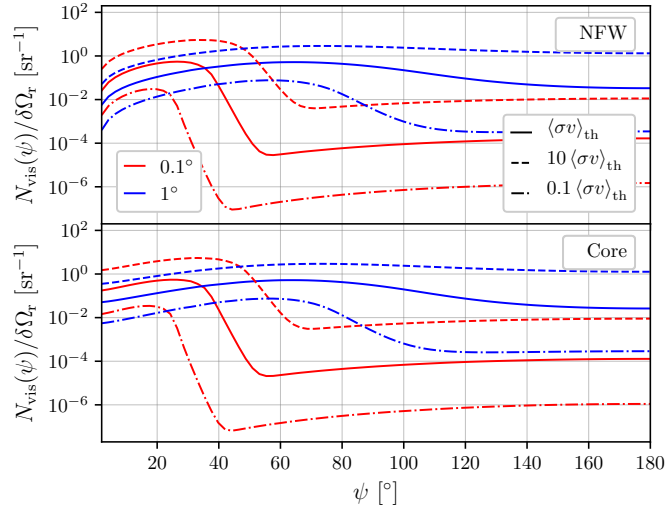


FIG. 5. **Top left panel:** Sky map of the effective number of subhalos per solid angle unit in a DM-only background—assuming a WIMP mass of 100 GeV annihilating to $\tau^+\tau^-$ with $\langle\sigma v\rangle = 3 \times 10^{-26} \text{ cm}^3/\text{s}$, a gamma-ray energy range 1 – 100 GeV, and a subhalo population configuration $(\alpha, m_{\text{min}}/M_\odot, \epsilon_t) = (1.9, 10^{-10}, 0.01)$ embedded in an NFW Galactic halo. **Top right panel:** Associated angular distribution (with 95% confidence band), with two angular resolutions $\theta_r = 0.1^\circ$ and 1° , and several configurations for the subhalo population ranging in $(\alpha, m_{\text{min}}/M_\odot) \in (1.9 - 2, 10^{-10} - 10^{-4})$. **Middle left and right panels:** Same as above for subhalos embedded in a cored Galactic halo. **Bottom panel:** Same as upper right panels, summarizing the angular distribution behavior for both the NFW (upper half) and cored Galactic halo (lower half), and for several annihilation cross sections around the canonical baseline $\langle\sigma v\rangle_{\text{th}} = 3 \times 10^{-26} \text{ cm}^3/\text{s}$.

less steep, and (ii) the diffuse background induced by un- resolved subhalos (equivalently the boost factor) is larger

in the $\alpha = 2$ case. The impact of the unresolved subhalo contribution to the diffuse background can actually be evaluated by changing m_{\min} from 10^{-10} to $10^{-4} M_{\odot}$, in the $\alpha = 2$ case. This shrinks the total number of subhalos (hence that of unresolved) by orders of magnitude ($N_{\text{tot}} \propto m_{\min}^{1-\alpha}$), but that depletion concerns only subhalos in the range 10^{-10} - $10^{-4} M_{\odot}$, which are not massive enough to detach from the background. Therefore, increasing m_{\min} in this mass range only reduces the DM-induced diffuse background emission, leading to more visible subhalos. One should still bear in mind that on general grounds, increasing m_{\min} corresponds to decreasing m_{χ} [32, 34].

Finally, it would be tempting to discuss the absolute numbers of detectable subhalos read off from the angular distribution plots. Caution is of order though, since these numbers are for the moment based on the very rudimentary statistical analysis defined in Eq. (60), and the observation configuration used is such that there is < 1 photon detected. A more refined statistical method will be presented later, but will actually not qualitatively change these results. Anyway, we already see from the right panels of Fig. 5 that even when turning the baryonic background off, the expected number of visible subhalos is or order $\mathcal{O}(1)$, which only slowly varies with $\langle\sigma v\rangle$ and observation time, as shown in Eq. (64).

b. Baryon-only background model: Considering only the baryonic foreground is a common practice to estimate the sensitivity to pointlike subhalos (e.g. [64, 66]), and amounts here to plug the foreground fluxes defined in Sect. V A into Eq. (58), such that

$$N_{\gamma}^{\text{bg}}(l, b, \Delta E) = N_{\gamma}^{\text{bg/cr}}(l, b, \Delta E), \quad (65)$$

where the subscript cr stands for ‘‘cosmic rays’’ (we neglect unresolved conventional astrophysical sources here).

In the absence of DM-induced background, the sensitivity to pointlike subhalos simply scales like

$$J_{\min}^{(l,b)} \propto \frac{\theta_r}{\langle\sigma v\rangle \sqrt{T_{\text{obs}}}} \Leftrightarrow \phi_{\min}^{(l,b)} \propto \frac{\theta_r}{\sqrt{T_{\text{obs}}}}, \quad (66)$$

where we see that the flux sensitivity ($\phi_{\min}^{(l,b)}$) has the standard scaling in time, and does not depend on $\langle\sigma v\rangle$ anymore as expected (it is fixed by the baryonic background within ΔE); as for the sensitivity to subhalos ($J_{\min}^{(l,b)}$), it does obviously depend on $\langle\sigma v\rangle$. Therefore, the reach in terms of $J_{\min}^{(l,b)}$ improves faster with $\langle\sigma v\rangle$ than in the DM-only background case—see Eq. (64). This has consequences in the determination of the number of visible subhalos, since the pdf of the J factor is a sharp function of J —see Fig. 3. However, one should bear in mind the previous approximate result that if detected after the diffuse DM component, in which case the latter adds up to the background, then the dependency in $\langle\sigma v\rangle$ becomes much shallower.

The corresponding sensitivity map of visible subhalos is shown in Fig. 6 (top left panel). To increase the contrast, we have masked a region defined by $\psi < 20^\circ$ in the

middle top panel. In the right top panel, we show the sky map obtained for $J_{\min}^{(l,b)}$, which defines the sensitivity map to pointlike subhalos, after masking the region $|b| < 5^\circ$ where most of the conventional DGE and of the Galactic sources concentrate, and which is less suited for subhalo searches. These maps have been derived from a full likelihood analysis performed on mock data, which will be extensively discussed later, but would be qualitatively the same if derived from the simplified statistical analysis introduced above. Further comparing them with the maps of Fig. 5 still on the qualitative level (they have been inferred from a different map of $J_{\min}^{(l,b)}$ set by the DM-only background), we see a similar concentration of visible subhalos in the central regions of the MW, except for the degraded sensitivity in the disk. The sensitivity to subhalos is less attenuated toward the very center because the increasing smooth halo contribution to the background has been unplugged here. The angular distribution of visible subhalos is not shown, but has similar trends as in Fig. 5, except for the different angular dependence of the background, and the fact that it is independent from $\langle\sigma v\rangle$ (the angular peak would be at lower angle).

c. Complete DM+baryon background model: Finally, we consider a more realistic background model in which both the diffuse DM contribution and the baryonic foreground are included. The number of background events is now given by

$$N_{\gamma}^{\text{bg}}(l, b, \Delta E) = N_{\gamma}^{\text{bg/cr}}(l, b, \Delta E) + N_{\gamma}^{\text{bg/dm}}(l, b, \Delta E), \quad (67)$$

where the number of DM-induced background events has been defined in Eq. (63), and that of standard astrophysical processes in Eq. (65).

To make this configuration even more realistic, we need to account for the fact that in the absence of departure from the background hypothesis, which is the current situation [84, 87, 88], there are actually independent constraints on $\langle\sigma v\rangle$. Therefore, especially in the context of a consistent subhalo model in which all components of the MW are dynamically linked together, the sensitivity to subhalos inherently correlates with the sensitivity to the diffuse DM contribution. This needs to be properly considered.

The constraint on the diffuse DM contribution can be expressed as a limit on the annihilation cross section that derives, in this preliminary simplified statistical analysis, from the condition

$$\frac{N_{\gamma}^{\text{diff}}(l, b, \Delta E)}{\sqrt{N_{\gamma}^{\text{bg}}(l, b, \Delta E)}} < \tilde{n}_{\sigma}, \quad (68)$$

where $\tilde{n}_{\sigma} = \mathcal{O}(1)$ can be considered as an effective number of background fluctuations below which the number of diffuse signal events must be confined to remain consistent with the background-only hypothesis. In the classical case of Poisson statistics, a $\sim 95\%$ ($\sim 99\%$) confidence-level (C.L.) limit is usually set with $\tilde{n}_{\sigma} = 2$ (3). Since

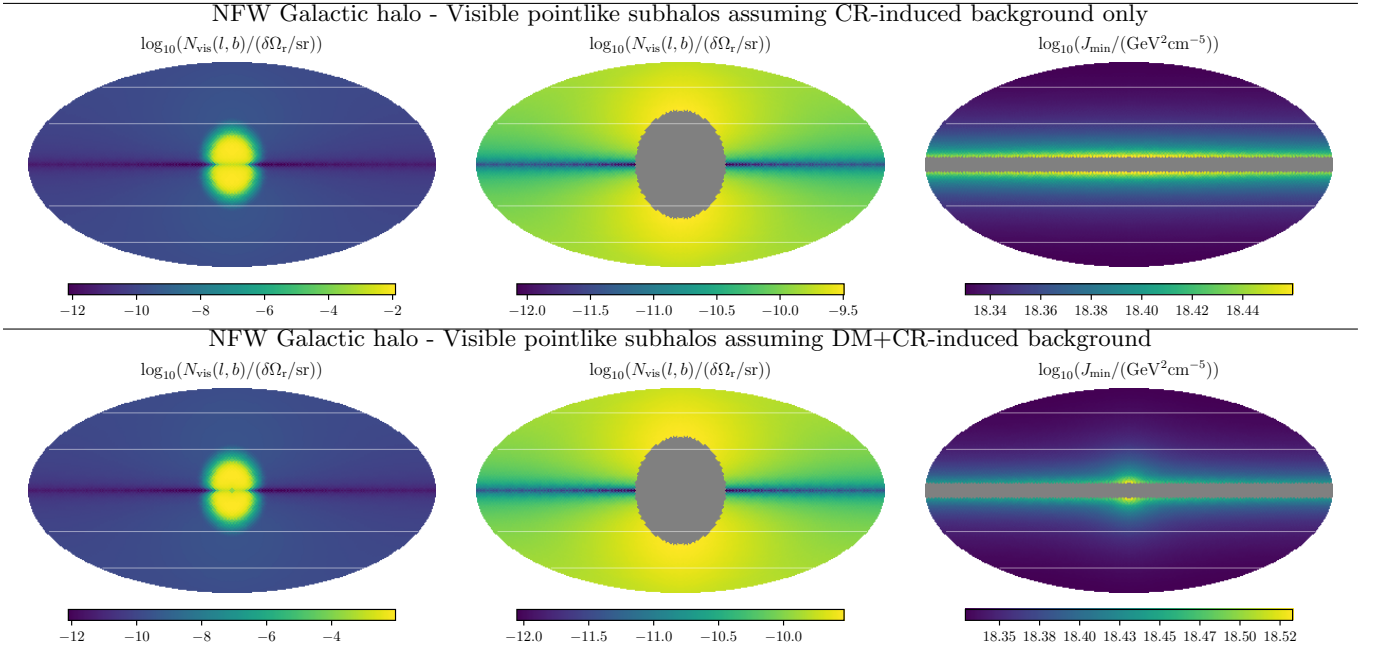


FIG. 6. Sky maps of the visible subhalos assuming a WIMP mass of 100 GeV annihilating into $\tau^+\tau^-$, and a subhalo population embedded in an NFW halo with parameters $(\alpha, m_{\min}/M_{\odot}, \epsilon_t) = (1.9, 10^{-10}, 0.01)$. The annihilation cross section is fixed to the $3\text{-}\sigma$ limit associated with the diffuse DM contribution. The detector configuration assumes a resolution angle of 0.1° , an observation time of 10 yr. The point-source sensitivity derives from a full likelihood analysis performed on mock data with parameters $(\alpha_b, \sigma_b) = (1.3, 0.1)$ in ROIs of $0.2^\circ \times 0.2^\circ$, covering a region of $2.2^\circ \times 2.2^\circ$, and run over 5 logarithmic bins in the [1-100] GeV energy range. Lines on maps indicate latitudes of $|b| = 30^\circ, 60^\circ$. **Top panels:** Baryonic background only. **Bottom panels:** Both baryonic and DM (smooth halo+unresolved subhalos) backgrounds. **Left panels:** Full sky. **Middle panels:** Same sky map with central region $\psi < 20^\circ$ masked to increase contrast. **Right panels:** sky map of $J_{\min}^{(l,b)}$ —sensitivity to pointlike subhalos—with $|b| < 5^\circ$ masked.

current statistical tools in gamma-ray data analyses are well more advanced, as we shall see later, this number is only to be taken as indicative here. Assuming that $N_{\gamma}^{\text{bg/cr}} \gg \tilde{n}_{\sigma}^2 > 1$, and that the diffuse DM signal remains unseen after an observational time \tilde{T} , the above inequality becomes

$$\overline{\mathcal{A}} \mathcal{S}_{\chi} \overline{J_{\psi}^{\text{diff}}} \tilde{T} < \tilde{n}_{\sigma} \sqrt{\tilde{T} \Delta E \left\langle \frac{dR^{\text{bg/cr}}}{dE} \right\rangle}, \quad (69)$$

where we have used Eqs. [(30), (31), and (59)]. This translates into an upper bound on the cross section:

$$\langle \sigma v \rangle_{\max} = \frac{2 m_{\chi}^2 \tilde{n}_{\sigma}}{\sqrt{\tilde{T}} \langle \mathcal{N}_{\gamma} \mathcal{A} \rangle} \min_{(l_c, b_c)} \left\{ \frac{\sqrt{\Delta E \left\langle \frac{dR^{\text{bg/cr}}}{dE} \right\rangle}}{J_{\psi}^{\text{diff}}} \right\}. \quad (70)$$

We emphasize that the minimum appearing above within braces is uniquely determined for a given configuration of DM and baryonic foreground. It is found at Galactic coordinates (l_c, b_c) (and may have replicates by symmetry). The scaling with m_{χ} is not fully explicit here, since the number of photons \mathcal{N}_{γ} also depends on m_{χ} , almost

$\propto \sqrt{m_{\chi}}$ for a large variety of annihilation final states [119]; hence $\langle \sigma v \rangle_{\max} \lesssim m_{\chi}^{3/2}$.

In Fig. 7, we show the results obtained using Eq. (70) for the determination of $\langle \sigma v \rangle_{\max}$ as a function of the WIMP mass m_{χ} , after integration of the gamma-ray fluxes in the 1 – 100 GeV energy range and using typical efficiency parameters for *Fermi*, recalled at the beginning of Sect. VC3. We report the limits derived from the very simplified statistical analysis presented just above as dashed (for $\theta_r = 0.1^\circ$) and dotted curves ($\theta_r = 1^\circ$, respectively), which have been obtained in a pointing direction $(l_c, b_c) = (0^\circ, 10^\circ)$ —dubbed “approx.” in the legends. We assume DM annihilation into $b\bar{b}$ (left panels) and $\tau^+\tau^-$ pairs (right panels), use $\tilde{n}_{\sigma} = 3$, and take two values for the observation time \tilde{T} : 2 (blue), and 10 yr (red curves, respectively). We have considered both an NFW Galactic halo (top panels) and a cored halo (bottom panels). We compare our results with the limits obtained by the *Fermi* Collaboration from the analysis of the diffuse Galactic emission [84] (dark gray area), using two years of data, and, for the sake of completeness, from satellite dwarf galaxies [132, 133] (light gray area). We also report results from a more complete likelihood analysis that will be discussed later (solid and dotted-dashed curves). We see that the simplified approach underesti-

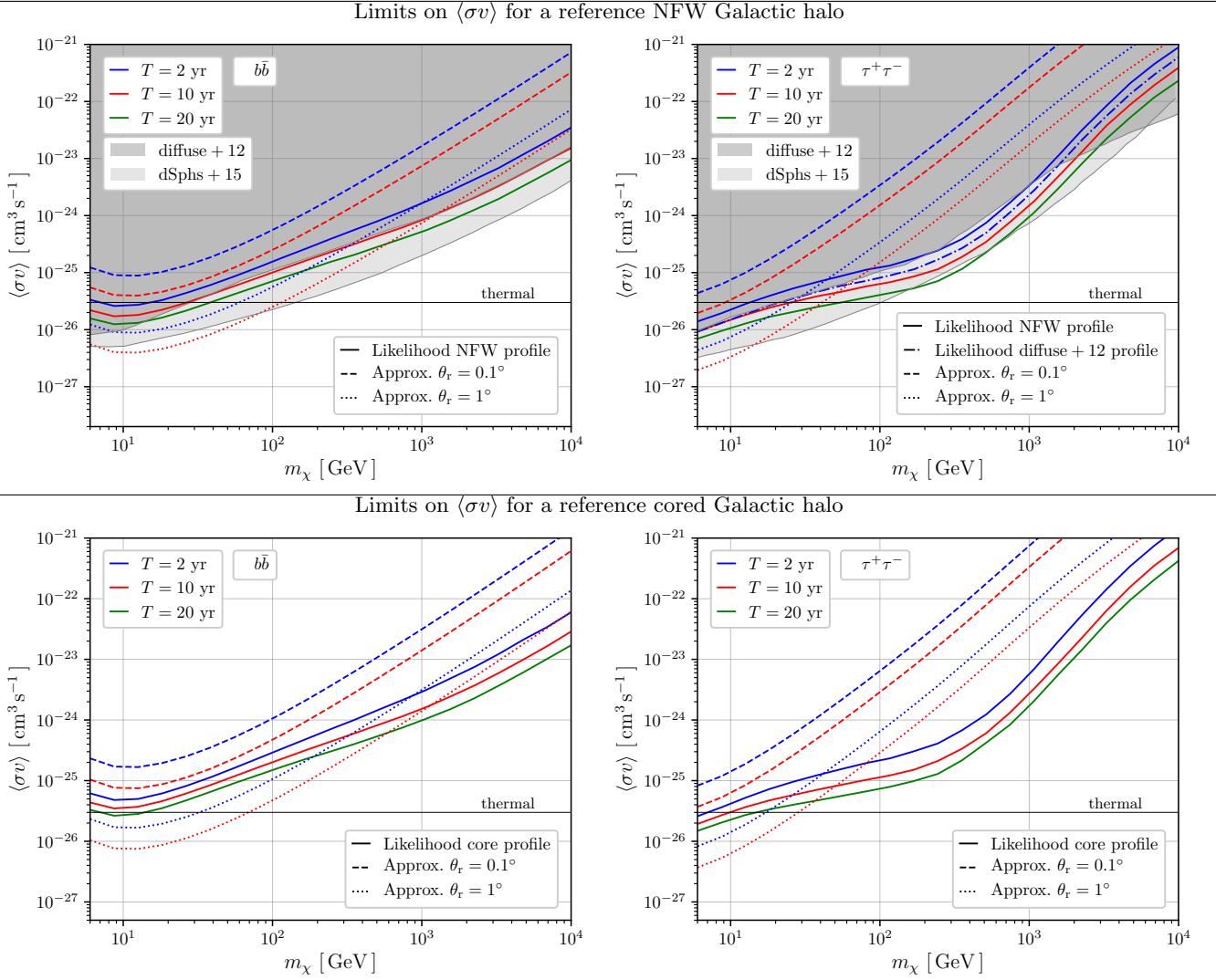


FIG. 7. Limits on $\langle\sigma v\rangle$, *i.e.* $\langle\sigma v\rangle_{\max}$, as a function of the WIMP mass m_χ for a Fermi-LAT-like telescope and for different observation times. Limits are set from: (i) the simplified statistical method presented in Sect. VC3c, with $\tilde{n}_\sigma = 3$, an angular resolution $\theta_r = 0.1^\circ$ (dashed lines) or $\theta_r = 1^\circ$ (dotted lines), pointing to Galactic coordinates $(l_c, b_c) = (0^\circ, 10^\circ)$; (ii) a full likelihood analysis performed on mock data, discussed in Sect. VC4, and using background parameters $(\bar{\alpha}_b, \sigma_b) = (1.3, 0.1)$. The likelihood limits correspond to $3\text{-}\sigma$ exclusion curves (solid curves). **Top panels:** Limits for both our reference NFW halo and the halo shape used in the Fermi-LAT analysis (dubbed “diffuse+12”—the dotted-dashed curve), together with the Fermi-LAT limits obtained from the diffuse Galactic emission [84] (dark gray area), and from dwarf galaxies [132, 133] (light gray area). **Bottom panels:** Same for our reference cored halo profile. **Left/right panels:** Full annihilation to $b\bar{b}/\tau^+\tau^-$ is assumed.

mates the real experimental sensitivity by almost an order of magnitude. Notwithstanding, it has a rather similar dependence in WIMP mass. The difference in sensitivity mostly comes from the fact that we use a single angular and energy bin, and therefore neglect a significant amount of available information. However, it is interesting to note that once we correctly rescale our effective sensitivity number \tilde{n}_σ , we can grossly match with the correct limit. This means that this simplified formalism may help capture the main dependencies and asymptotic behavior of a more realistic sensitivity to DM subhalos.

Assuming that the limit on $\langle\sigma v\rangle$ reaches the upper

bound $\langle\sigma v\rangle_{\max}$, *i.e.* the diffuse DM component is at the verge of being detected but is still not so, we can replace $\langle\sigma v\rangle$ by $\langle\sigma v\rangle_{\max}$ in Eq. (61). This provides us with a critical value for the pointlike subhalo detection threshold:

$$J_{\min}^{\text{crit}}(l, b, \Delta E) = \eta_\sigma^{\text{eff}} \sqrt{\Delta E \left\langle \frac{dR^{\text{bg/cr}}}{dE} \right\rangle} \times \max_{(l_c, b_c)} \left\{ \frac{J_\psi^{\text{diff}}}{\sqrt{\Delta E \langle dR^{\text{bg/cr}}/dE \rangle}} \right\}, \quad (71)$$

where

$$\eta_{\sigma}^{\text{eff}} \equiv \frac{n_{\sigma}}{\tilde{n}_{\sigma}} \sqrt{\frac{\tilde{\mathcal{T}}}{\mathcal{T}}} \approx \frac{n_{\sigma}}{\tilde{n}_{\sigma}}. \quad (72)$$

Interestingly, this critical J factor does not depend on the annihilation cross section anymore. Note that the background event rate $\langle dR^{\text{bg/cr}}/dE \rangle$ is calculated at Galactic coordinates (l_c, b_c) in the max term, while it is calculated at the target coordinates (l, b) outside from the max term—all this is therefore fixed for a given Galactic emission model. It turns convenient to combine the dependencies in the different observation times $\tilde{\mathcal{T}}$ (used to set the limit on $\langle \sigma v \rangle$) and \mathcal{T} (on-subhalo-target time) and in the fluctuation thresholds \tilde{n}_{σ} and n_{σ} into a single effective sensitivity parameter $\eta_{\sigma}^{\text{eff}}$. In pure Poisson statistics associated with an on-off method, and with $\mathcal{T} \sim \tilde{\mathcal{T}}$, we should have $\eta_{\sigma}^{\text{eff}} \sim n_{\sigma}/\tilde{n}_{\sigma} \approx 5/2$ or $5/3$. However, connecting with more advanced statistical analysis methods and different observational strategies allows for considering a much wider range of values, say $\mathcal{O}(1 - 10)$ per energy bin.

For non-pointing experiments, like Fermi-LAT, $\tilde{\mathcal{T}} \approx \mathcal{T}$, and $J_{\text{min}}^{\text{crit}}$ further becomes a priori time-independent (this holds in the large-event-number limit). The fact that $J_{\text{min}}^{\text{crit}}$ is independent from both the annihilation cross section and the observation time (in the infinite-time limit) is, though derived from strongly simplifying assumptions here, a very important result. It is actually recovered when using a more sophisticated statistical analysis as we will see later. It means that we can rigorously answer the question of whether or not subhalos can be detected before the diffuse DM component, should DM self-annihilate and produce gamma-ray photons. Indeed, the derivation of $J_{\text{min}}^{\text{crit}}$ is based upon requiring the diffuse DM contribution to remain below the baryonic background. Therefore, irrespective of the annihilation cross section, one can simply infer the number of observable subhalos by integrating the probability distribution function of the J factor shown in Fig. 3 above $J_{\text{min}}^{\text{crit}}$. If one finds the minimal J factor needs to be lower than this critical value to get a sizable number of observable subhalos, then that means that subhalos could hardly be detected as individual sources before the smooth Galactic DM halo itself.

That $J_{\text{min}}^{\text{crit}}$ does not explicitly depend on time needs further explanation. As said above, it is defined from the sensitivity $J_{\text{min}} \propto (\sqrt{\mathcal{T}} \langle \sigma v \rangle)^{-1}$ (see Eq. 61), but evaluated at the maximal cross section $\langle \sigma v \rangle_{\text{max}} \propto 1/\sqrt{\mathcal{T}}$ (see Eq. 70). This explains why the time dependence disappears in our simplified analysis. However, even though $J_{\text{min}}^{\text{crit}}$ is roughly expected to be time independent, it must still be associated with the time-dependent maximal annihilation cross section $\langle \sigma v \rangle_{\text{max}}$.

In Fig. 8, we trace $J_{\text{min}}^{\text{crit}}$ as a function of observation time from the simplified definition of Eq. (71) on the one hand (with a conveniently rescaled $\eta_{\sigma}^{\text{eff}}$ —blue dashed curve), and from a more sophisticated likelihood analysis of mock data that will be discussed below (blue solid curve). When inferred from the simplified analysis, $J_{\text{min}}^{\text{crit}}$

is independent of time, as explained above. In slight contrast, it becomes flat only after a time of several years when inferred from a full likelihood analysis, because the latter correctly deals with the statistics of small numbers of events, but still asymptotically confirms the prediction obtained from the simplified method. The left and right panels differ only by the resolution angle (see caption). We also report the time-dependent sensitivity to pointlike subhalos J_{min} (in the direction where J_{min} is minimized) as a function of time, assuming an annihilation cross section set by a 3- σ limit on the diffuse DM flux after 10 yr ($\langle \sigma v \rangle = \langle \sigma v \rangle_{\text{max}}(10 \text{ yrs})$, red curves) or 20 yr ($\langle \sigma v \rangle = \langle \sigma v \rangle_{\text{max}}(20 \text{ yrs})$, green curves)—the latter being $\sim \sqrt{2}$ smaller. The J_{min} curves cross the critical $J_{\text{min}}^{\text{crit}}$ ones at the corresponding times, as they should. Beyond these special crossing times, the decrease of $J_{\text{min}} \propto 1/\sqrt{\mathcal{T}}$ holds true assuming the diffuse DM-induced emission has truly been detected at these times. If not, then one should keep on following the critical blue lines until the detection of the diffuse emission (time from which J_{min} scales like $\propto 1/\sqrt{\mathcal{T}}$ again). Therefore, if the values of J_{min} needed to detect a sizable number of subhalos lie below $J_{\text{min}}^{\text{crit}}$, that means that one should detect the diffuse DM-induced emission first.

4. A full likelihood analysis of mock data

In order to validate the previous results, we upgrade our statistical analysis method to get closer to the standards employed in the Fermi Collaboration for both the smooth Galactic DM searches [84, 87, 88] and the subhalo or pointlike source searches [58–69]. We therefore set up a full likelihood analysis.

a. Mock data generation : We first generate mock data based on the signal and background configurations discussed above. However, here, we need to add a layer of subtlety. Indeed, to be as realistic as possible, we want to artificially reproduce the fact that like in the Fermi data analysis, our background model be not perfect, and that positive fluctuations arising from uncontrolled systematic effects degrade the sensitivity to DM searches. We also want to implement the fact that so far the smooth DM has not been convincingly detected. Therefore, our mock data will be based on a biased version of our baryonic diffuse emission model introduced in Sect. V A, which will leave room for positive fluctuations possibly interpreted as DM annihilation in the absence of systematic uncertainties. To make it simple, the bias will simply amount to a systematic shift by 30% of the Galactic baryonic foreground, inspired by the value of residuals found in the Fermi-LAT analysis [84].

We divide the sky into N_{θ} angular bins labeled i (also called pixels in the following) each divided into N_E energy bins labeled j . We denote b_{ij} the averaged number of photons expected from our background emission model and instrumental specifications [see Sect. V A, Sect. V C 1, Eqs. (58) and (59)] in a given

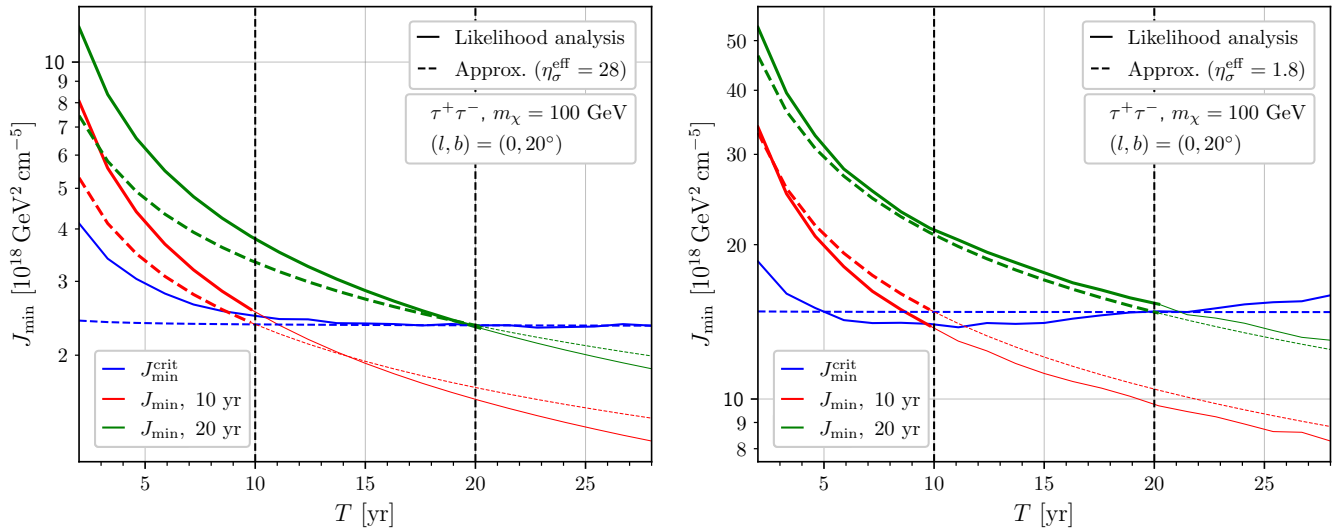


FIG. 8. Minimal J factor (sensitivity to pointlike subhalos) as a function of time, assuming a subhalo population embedded in an NFW Galactic halo, and a WIMP of 100 GeV annihilating into $\tau^+\tau^-$. Solid curves are obtained from the full likelihood analysis of mock data, and dashed curves from the simplified statistical analysis, with a rescaled effective sensitivity parameter η_σ^{eff} . Blue curves indicate the critical J factor $J_{\text{min}}^{\text{crit}}$ at which the smooth DM contribution remains at its $3\text{-}\sigma$ limit. Red curves show $J_{\text{min}}(T)$ assuming an annihilation cross section set from the likelihood $3\text{-}\sigma$ limit (non-detection of the smooth DM contribution) for 10 yr of observation, while green curves show $J_{\text{min}}(T)$ assuming a lower annihilation cross section set from the likelihood limit for 20 yr (see Fig. 7). As expected, the red and green curves cross the critical blue ones at 10 yr and 20 yr, respectively. **Left panel:** $\theta_r = 0.1^\circ$. **Right panel:** $\theta_r = 1^\circ$ (mimicking the sensitivity to extended sources).

two-dimensional (2D) bin. We then generate our mock data by drawing a corresponding number of gamma-ray photons n_{ij} in that bin according to a Poisson distribution

$$p(n_{ij} | b_{ij}) = \frac{b_{ij}^{n_{ij}}}{n_{ij}!} e^{-b_{ij}}. \quad (73)$$

Note that since our goal is to set limits, we do not generate any signal event in our mock data.

In Fig. 9, we show an example of such mock data for a collection time of 2 yr in pixels of size $1^\circ \times 1^\circ$. We get $\sim 360,000$ photon events in the 1–100 GeV energy range and in the selected ROI ($5^\circ < |b| < 15^\circ$ and $|l| < 80^\circ$), which is very close to the number count found in Ref. [84] ($\lesssim 5\%$ larger). To further account for the point-source subtraction performed in the Fermi data analysis we remove $\sim 25\%$ of the bins randomly over the sky, which defines our initial sample of $\sim 270,000$ collected photons, still very close to the statistics used in Ref. [84]. These mock data are further processed through a likelihood analysis discussed just below, which consists of two different steps: (i) setting the limit on $\langle\sigma v\rangle$ from the diffuse emission; (ii) defining the sensitivity to pointlike subhalos.

b. Likelihood analysis of the diffuse emission: Limits on $\langle\sigma v\rangle$: In order to analyze our mock data, we set up a likelihood analysis similar to the one performed by the Fermi-LAT Collaboration to get limits on the diffuse Galactic DM-induced emission. We also want to account for the fact that significant fluctuations arise

between the background model and the data due to an imperfect background modeling, which makes the likelihood possibly underestimate the background by $\sim 30\%$ [84]. To this aim, we introduce a bias parameter α_b that will be applied to the DGE background only. It is centered around a reconstruction efficiency $\varepsilon_{\text{rec}} = 0.7$, and with a Gaussian probability distribution such that an unbiased distribution would cost a $\sim 3\text{-}\sigma$ penalty, which is obtained from a Gaussian width $\sigma_b = 0.1$. This biasing procedure will mechanically degrade the limit derived on the DM annihilation signal, in the same vein as in the conservative analysis performed in Ref. [84]. These values for the bias parameters are inspired from the numbers quoted in Ref. [84], and allow us to derive a limit on the annihilation cross section from our mock data analysis in reasonable agreement with the corresponding results. Changing the values of ε_{rec} and σ_b would not change our results qualitatively, keeping the final orders of magnitude unchanged.

We can now construct a simple likelihood function to fit our signal and background models with a limited number of parameters (for a given WIMP mass m_χ): the annihilation cross section $\langle\sigma v\rangle$ and the background bias parameter α_b . The chance of getting a number n_{ij} of photons in bin (i, j) can be estimated from the likelihood

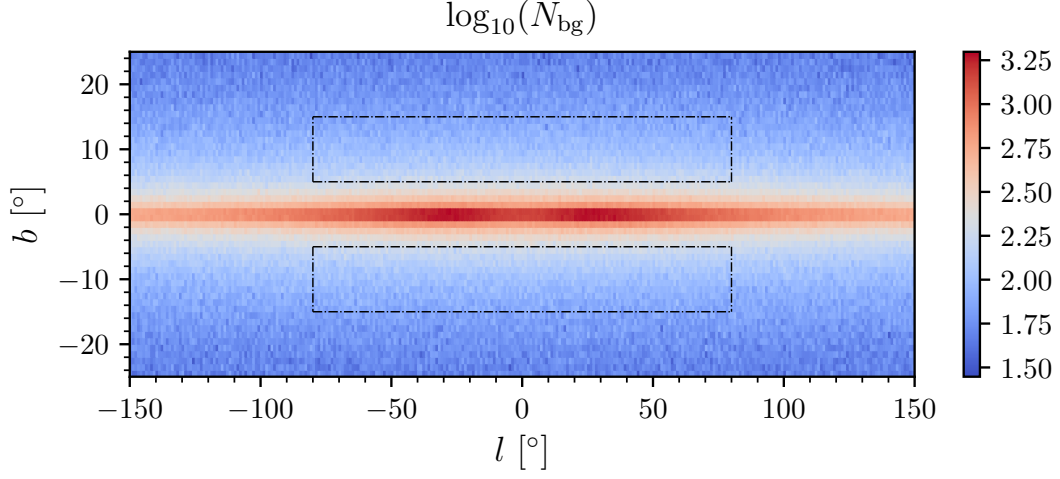


FIG. 9. Mock photon count map of biased background photons received in bins of size $1^\circ \times 1^\circ$ in the range 1 – 100 GeV. The contour areas correspond to the ROI used to set constraints on $\langle\sigma v\rangle$.

function

$$\begin{aligned} \mathcal{L}_{ij}(n_{ij} | \langle\sigma v\rangle, \alpha_b) &= \frac{(a_{ij}\langle\sigma v\rangle + \alpha_b b_{ij}^{\text{DGE}} + b_{ij}^{\text{iso}})^{n_{ij}}}{n_{ij}!} \\ &\times e^{-(a_{ij}\langle\sigma v\rangle + \alpha_b b_{ij}^{\text{DGE}} + b_{ij}^{\text{iso}})} \\ &\times \left\{ \mathcal{L}_{\text{sys}}(\alpha_b) \equiv \frac{e^{-\frac{(\alpha_b - \varepsilon_{\text{rec}})^2}{2\sigma_b^2}}}{\sqrt{2\pi\sigma_b^2}} \right\}, \end{aligned} \quad (74)$$

where a_{ij} is defined such that the averaged number of photons expected from DM annihilation in bin (i, j) be $s_{ij} = \langle\sigma v\rangle a_{ij}$, and b_{ij}^{DGE} and b_{ij}^{iso} stand, respectively, for the DGE and isotropic backgrounds given in Eq. (49). \mathcal{L}_{sys} is our nuisance function that adds up a Gaussian penalty of σ_b if the bias parameter α_b departs from the imperfect reconstruction efficiency $\varepsilon_{\text{rec}} < 1$. This helps the model get closer to the mock data from below, while not too close to leave room for a possible DM contribution. This trick mimics a mismodeled background, which typically leads to 30% fluctuations around the background-only hypothesis in the real Fermi data analysis [84, 87, 88]. This parametrizes our uncertainty in the background model, and allows us to calibrate our likelihood analysis to get results close enough to past or current data analyses, and then to more confidently extrapolate it to future times. Such a likelihood function is often called a profiled likelihood, because it is not normalized to unity with respect to the data. The total profiled likelihood associated with all bins is given by

$$\mathcal{L}(\langle\sigma v\rangle, \alpha) = \prod_{ij} \mathcal{L}_{ij}(n_{ij} | \langle\sigma v\rangle, \alpha_b). \quad (75)$$

Equipped with this improved statistical setup, the first step is to find the best-fitting parameters of the model (including both the signal and the background), which we

denote $(\widehat{\langle\sigma v\rangle}, \widehat{\alpha}_b)$ for a given WIMP mass and given annihilation channels. Whenever the isotropic background can be neglected (*e.g.* in the central Galactic regions at low energy), we could proceed semi-analytically, as explained in Appendix B1. However, in the general case, we have to resort to the numerical method presented in Appendix B3.

Eventually, to set a conservative upper bound on $\langle\sigma v\rangle$ without directly comparing the background-only and the signal-and-background hypotheses, we standardly define our null hypothesis as our signal-and-background best-fitting model characterized by $(\widehat{\langle\sigma v\rangle}, \widehat{\alpha}_b)$, and compute the likelihood ratio to that null hypothesis,

$$\mathcal{R}(\langle\sigma v\rangle) \equiv \frac{\mathcal{L}(\langle\sigma v\rangle, \tilde{\alpha}_b(\langle\sigma v\rangle))}{\mathcal{L}(\widehat{\langle\sigma v\rangle}, \widehat{\alpha}_b)}. \quad (76)$$

Here, $\tilde{\alpha}_b(\langle\sigma v\rangle)$ characterizes the best-fitting model for which $\langle\sigma v\rangle$ is now a fixed parameter.

Let us now present as clearly as possible the way we set a limit, and its precise statistical meaning. Wilks' theorem [134, 135] tells us that when the number of data points goes to infinity, under the condition that the null hypothesis holds true, the log-likelihood ratio defined as $-2 \ln \mathcal{R}(\langle\sigma v\rangle)$ satisfies a $\chi^2(1)$ distribution [136], where the probability density of $\chi^2(k)$ is given by

$$f_{\chi^2(k)}(x) \equiv \frac{1}{2^{k/2}\Gamma(k/2)} x^{k/2-1} e^{-x/2}. \quad (77)$$

If we denote p_0 the probability to have $-2 \ln \mathcal{R}(\langle\sigma v\rangle) > t$

under the null hypothesis, then t is implicitly defined by

$$\begin{aligned} p_0 &= \int_t^\infty dy f_{\chi^2(1)}(y) \\ &= \int_t^\infty dy \frac{1}{\sqrt{2\pi y}} e^{-y/2} \\ &= \sqrt{\frac{2}{\pi}} \int_{\sqrt{t}}^\infty dx e^{-x^2/2}. \end{aligned} \quad (78)$$

Therefore, if we demand a constraint at $\tilde{n}_\sigma \sigma$, then this translates into

$$\begin{aligned} p_0 &= 1 - \frac{1}{\sqrt{2\pi}} \int_{-\tilde{n}_\sigma}^{+\tilde{n}_\sigma} dx e^{-x^2/2} \\ &= \sqrt{\frac{2}{\pi}} \int_{\tilde{n}_\sigma}^\infty dx e^{-x^2/2}, \end{aligned} \quad (79)$$

which implies from the previous equation that $t = \tilde{n}_\sigma^2$.

To summarize, a limit at $\tilde{n}_\sigma \sigma$ can be set by looking for the value of $\langle \sigma v \rangle$ such that $-2 \ln \mathcal{R}(\langle \sigma v \rangle) = t = \tilde{n}_\sigma^2$. If instead we want to define the limit from the probability itself, for example $p_0 = 0.05$ (equivalently a limit at 95% confidence level), then we just have to solve

$$\text{erfc} \left[\sqrt{\frac{t}{2}} \right] = 0.05, \quad (80)$$

which has solution $t \simeq 3.85$. Actually, parameter t represents here what is generically called the test statistics (TS) [130] in Fermi-LAT data analyses.

We use this likelihood approach to derive limits on $\langle \sigma v \rangle$ from the analysis of our mock data. This limit is important to assess whether pointlike subhalos can be detected before or after the DM-induced diffuse emission itself. It is the likelihood equivalent to $\langle \sigma v \rangle_{\text{max}}$ defined in Eq. (70) and derived from our simplified statistical analysis. It fully determines $J_{\text{min}}^{\text{crit}}$ (see Eq. 71), the critical threshold J factor for subhalos, below which subhalos cannot be detected before the DM-induced diffuse emission itself.

We first check whether the limit we get is consistent with the one derived by the Fermi-LAT Collaboration in Ref. [84], calculated with two years of data. In fact, this comparison can help us check whether the imperfect reconstruction efficiency ε_{rec} , which characterizes the bias between the background model and the mock data, and the Gaussian penalty σ_b paid by the reconstruction likelihood to catch up with the mock data, provide a realistic analysis framework. Indeed, these parameters are meant to inject a tunable systematic error that degrades the limit on $\langle \sigma v \rangle$, in order to more correctly fake the results obtained from the real data analysis performed in Ref. [84].

We analyze the mock data introduced before by selecting the same ROI as in Ref. [84], *i.e.* $5^\circ < |b| < 15^\circ$ and $|l| < 80^\circ$, which we divide into 160 angular bins of size $1^\circ \times 1^\circ$. We collect photons in an energy range of 1 – 100 GeV further split into 5 logarithmic bins, using the experimental specifications listed in Sect. VC1

with a flat angular resolution of $\theta_r = 0.1^\circ$. After removal of virtual point sources randomly distributed in 25% of the available pixels, we reach a total of $\sim 270,000$ collected photons in the ROI after two years, similar to the statistics found in Ref. [84]. Setting our systematic bias parameters to $\varepsilon_{\text{rec}} = 0.7$ and $\sigma_b = 0.1$ in the likelihood function, we derive the limits shown as solid curves in Fig. 7 (using our Galactic halo model). We also report the likelihood limit inferred from the very same NFW halo parameters as in Ref. [84] as the dotted-dashed curve (top right panel, $\tau^+ \tau^-$ channel), which can be more directly compared with the limit derived in Ref. [84] (dark gray shaded area). We see that in spite of a slight and systematic underestimate of the genuine limit, the “spectral” agreement is quite reasonable up to WIMP masses of $\lesssim 1$ TeV for the $\tau^+ \tau^-$ channel. This is a positive cross-check of our chain of mock data analysis (we cut the analysis above 100 GeV). The agreement is also reasonable for the $b\bar{b}$ channel (top left panel).

These good qualitative matching and reasonably good quantitative agreement with a real data analysis validate the method, and make us confident to extrapolate our results to longer observation times. This is what we show also in Fig. 7, by extracting our limits for 10 and 20 years of observation (red and green curves, respectively). Since our mock data are generated without DM signal, we see that the limits improve as $\sim \sqrt{T}$, as expected. The next step is to study the sensitivity to individual subhalo detection.

c. Likelihood analysis to set the sensitivity to pointlike subhalos :

To determine the sensitivity to pointlike subhalos, we again implement a statistical method similar to the standards used in the Fermi collaboration [58, 59], which are also based on a likelihood approach. In the following, the search for pointlike subhalos is performed over the full sky, except for for the disk region $|b| < 5^\circ$ which is masked.

In the case of pointlike subhalo searches, the likelihood function should have the same form as the one used to set constraints on the diffuse emission model, but that diffuse-only model itself needs to be upgraded to allow for the insertion of a pointlike subhalo in a pixel of angular resolution size.

Focusing on a specific direction in the sky and slightly around, and labeling our angular bins by i (with a nominal resolution angle $\theta_r = 0.1^\circ$) and the energy bins by j , we define the point-source search window as a region of $2.2^\circ \times 2.2^\circ$ about the pointing direction, divided in angular bins of $0.2^\circ \times 0.2^\circ$. When extending the nominal case to an increased resolution of $\theta_r = 1^\circ$, we shall increase the region to $6^\circ \times 6^\circ$ divided in bins of $2^\circ \times 2^\circ$. We still use 5 logarithmic energy bins covering the 1 – 100 GeV energy range.

The null hypothesis amounts to having no point source at all. We want to quantify the likelihood ratio change if we introduce a source in pixel i_0 . To do so, we generate new mock data in the same way as for the diffuse emission

for $i \neq i_0$, with the probability

$$p(n_{ij} | b_{ij}) = \frac{(b_{ij} + a_{ij}\langle\sigma v\rangle)^{n_{ij}}}{n_{ij}!} e^{-(b_{ij} + a_{ij}\langle\sigma v\rangle)}, \quad (81)$$

where b_{ij} stands for both the DGE and the isotropic baryonic backgrounds, and where we impose $\langle\sigma v\rangle \leq \langle\sigma v\rangle_{\max}$ ($T = 2$ yr) since we consider cases for which we have not detected DM through the diffuse component at the time of observation (we could use ~ 8 yr [88] instead, but this would not qualitatively change our results). In the central pixel i_0 we simply set

$$n_{ij} = b_{ij} + a_{ij}\langle\sigma v\rangle + \bar{J}\langle\sigma v\rangle c_{ij}, \quad (82)$$

where the product $\bar{J}\langle\sigma v\rangle c_{ij}$ represents the number of photons received from a pointlike subhalo in pixel $i = i_0$ with a J factor \bar{J} and an annihilation cross section $\langle\sigma v\rangle$. The factor c_{ij} satisfies $c_{ij} = c_{ij}^0 \delta_{i,i_0}$. We stress that here $\langle\sigma v\rangle$ has to be considered as a fixed parameter of the model. Remind also that \bar{J} is the true J factor injected in the mock data.

The reconstruction likelihood function to consider should then be characterized by two free parameters ($\langle\sigma v\rangle$ being fixed): J , *i.e.* the J factor of the pointlike subhalo to estimate, and α_b , which represents the departure from central value of the background model. That likelihood function reads

$$\begin{aligned} \mathcal{L}_{ij}(n_{ij} | J, \alpha; \langle\sigma v\rangle) = & \frac{(c_{ij}^0 \langle\sigma v\rangle J \delta_{i,i_0} + a_{ij}\langle\sigma v\rangle + \alpha_b b_{ij}^{\text{DGE}} + b_{ij}^{\text{iso}})^{n_{ij}}}{n_{ij}!} \\ & \times e^{-(c_{ij}^0 \langle\sigma v\rangle J \delta_{i,i_0} + a_{ij}\langle\sigma v\rangle + \alpha_b b_{ij}^{\text{DGE}} + b_{ij}^{\text{iso}})} \\ & \times \frac{1}{\sqrt{2\pi\sigma_b^2}} e^{-\frac{(\alpha_b - \varepsilon_{\text{rec}})^2}{2\sigma_b^2}}. \end{aligned} \quad (83)$$

As before, departing from $\alpha_b = \varepsilon_{\text{rec}}$ to better match with the mock data costs a Gaussian penalty of σ_b , which again allows to artificially account for background mis-modeling, as in the diffuse emission analysis.

The total likelihood function is then simply given by

$$\mathcal{L}(J, \alpha; \langle\sigma v\rangle) = \prod_{ij} \mathcal{L}_{ij}(n_{ij} | J, \alpha; \langle\sigma v\rangle). \quad (84)$$

We first want to determine the bias parameter $\tilde{\alpha}_b$ that maximizes the likelihood function in the null hypothesis (no point source). This could be done semi-analytically if we neglected the isotropic background, as shown in Appendix B2. However, contrary to the previous case, the signal hypothesis is now characterized by two maximizing parameters $(\hat{\alpha}_b, \hat{J})$, which are solutions to a system of equations hardly solvable by semi-analytical methods. Therefore, in the signal hypothesis, even in a simplified background modeling, we have to resort to the Newton-Raphson algorithm, as explained in Appendix B3.

We can eventually write down the likelihood ratio of the signal-to-null hypotheses

$$\mathcal{R} \equiv \frac{\mathcal{L}(\hat{J}, \hat{\alpha}_b; \langle\sigma v\rangle)}{\mathcal{L}(0, \tilde{\alpha}_b; \langle\sigma v\rangle)}, \quad (85)$$

and unambiguously define a 5σ detection threshold by demanding $2 \ln \mathcal{R} > 25$. It is clear that the higher \bar{J} in the generated mock data, the higher \mathcal{R} in the analysis, as it drives the likelihood ratio further and further away from the null hypothesis. We denote J_{\min} the value of \bar{J} such that in average $2 \ln \mathcal{R} = 25$, similarly to Eq. (61) in the simplified statistical analysis. More formally:

$$J_{\min}^{(l,b)} = \bar{J} \mid \ln \mathcal{R}(l,b) = \frac{25}{2}. \quad (86)$$

This time, the sensitivity to pointlike subhalos J_{\min} , still a function of Galactic coordinates (l,b) , is determined from a much more rigorous statistical likelihood analysis of mock data, such as the ones currently used on real data.

Skymaps of J_{\min} are shown in the right panels of Fig. 6 (baryonic background only in the top panel, and both baryonic and diffuse DM backgrounds in the bottom panel, setting $\langle\sigma v\rangle$ to its 3σ limit in the latter case, $\sim 5 \times 10^{-26} \text{ cm}^3 \text{ s}^{-1}$, which can be read off Fig. 7). We see that the angular distribution strongly depends on the background, with a stronger contrast toward the central regions of the MW when the diffuse DM contribution is included. This obviously affects the angular distribution of detectable objects, as we will discuss later. We note that we get values of $J_{\min} \approx 10^{18} \text{ GeV}^2/\text{cm}^5$, which provide a rather generic order of magnitude for the subhalo detection threshold, which can be compared with the probability density function of subhalo J factors in Fig. 3.

The time dependence of J_{\min} is further shown in Fig. 8 as the red and green solid curves (the corresponding dashed curves illustrate the simplified analysis). The former is obtained by setting the annihilation cross section to its limit after 10 yr of (virtual) observation without detection of the smooth halo, while the latter is based on the 20-yr limit (hence a value of $\langle\sigma v\rangle$ smaller by a factor of $\sim \sqrt{2}$). The left (right) panel assumes an experimental angular resolution of $\theta_r = 0.1^\circ$ (1° , respectively). We see that the prediction from the simplified analysis $J_{\min} \propto 1/\sqrt{T}$ is only recovered in the large θ_r case, while for nominal angular resolution J_{\min} decreases slightly faster with time. This is a purely statistical effect which derives from the fact that some energy bins are empty or almost so in the latter case. This cannot be captured with our simplified analysis, while it is properly treated with the likelihood method. In particular, we see that the values obtained for J_{\min} in that case are much more conservative at small observation time with the likelihood determination. However, the simplified analysis gets the qualitative trend of results correct, which shows its relevance to help understand the driving physical effects from analytical calculations.

By combining the sensitivity J_{\min} with the 3σ limit on $\langle\sigma v\rangle$ obtained from the absence of DM signal in the diffuse emission in the mock data, we can determine the critical sensitivity J_{\min}^{crit} , *i.e.* the threshold above which pointlike subhalos cannot be detected before the diffuse

DM signal. As explained around Eq. (71), J_{\min}^{crit} is simply the time-dependent value of J_{\min} obtained by setting $\langle\sigma v\rangle = \langle\sigma v\rangle_{\max}(T)$ in the likelihood function of Eq. (83) applied to the mock data generated for pointlike source searches. This can be formulated as

$$J_{\min}^{\text{crit}}(T) = J_{\min}(T, \langle\sigma v\rangle_{\max}(T)). \quad (87)$$

Being the critical J factor sensitivity below which the DM-induced diffuse emission should have already been detected, integrating the pdf of pointlike subhalo J factors above J_{\min}^{crit} (see Fig. 3) allows us to determine the number of subhalos that can be detected as pointlike objects before the smooth DM itself. With the rather involved statistical method described above, we can already check one of the main predictions of the earlier simplified statistical treatment: the fact that J_{\min}^{crit} should become asymptotically constant with time, and independent of annihilation cross section (as long as it is defined from the 3σ limit on $\langle\sigma v\rangle$ derived from the diffuse signal analysis, which does depend on observation time).

Values of J_{\min}^{crit} as functions of time and computed from the likelihood analysis are reported in Fig. 8 as the solid blue curves (the dashed blue curves show the results obtained with the simplified analysis). The left (right) panel assumes an angular resolution of $\theta_r = 0.1^\circ$ (1° , respectively). Are also shown the evolutions of the subhalo detection threshold (or sensitivity) J_{\min} derived assuming two different annihilation cross sections: one corresponding to the 10-yr limit in the diffuse signal (red curves), and the other one corresponding to the 20-yr limit (green curves). The J_{\min}^{crit} curves cross the J_{\min} red (green) ones at 10 yr (20 yr, respectively), as expected, since they have been derived assuming $\langle\sigma v\rangle_{\max}(10/20 \text{ yr})$.

These complete likelihood results for J_{\min}^{crit} do confirm the prediction obtained from the simplified analysis: J_{\min}^{crit} flattens and tends to a constant value at large observation time, which can be accurately determined from a likelihood analysis. It might look surprising that J_{\min}^{crit} is independent of time, but recall that it is calculated from $\langle\sigma v\rangle_{\max}(T)$ which does depend on time. The deep meaning of this time independence is that not detecting the diffuse component intrinsically limits the luminosity of subhalos, which is proportional to $\langle\sigma v\rangle$. Hence, this critical parameter self-consistently includes all the physical degeneracies of the problem.

VI. SUMMARY RESULTS AND CONCLUSION

After this pedestrian exploration of the issue of subhalo searches with Fermi-LAT-like gamma-ray experiments, it is worth summarizing our main results and drawing more quantitative conclusions.

First of all, the path we have followed in this study is complementary to many other similar works in that (i) it does not rely on a real data analysis, only on educated modeling; (ii) it is based on subhalo population

models self-consistently embedded in full kinematically constrained Galactic mass models; (iii) it relies on semi-analytical calculations that allow us to integrate over the full available phase space that describes subhalos. Our subhalo population model accounts for tidal stripping induced by both the DM component and the baryonic disk, which are properly evaluated from the currently constrained distributions of DM and baryons. It is therefore not based on *ad hoc* rescaled formulations from cosmological simulations. This induces a tight dynamical correlation between the subhalo properties and the other Galactic components, which has to be treated self-consistently for a proper estimate of the detectability of subhalos. Indeed, this correlation strongly affects the angular distribution of the signal-to-noise ratio.

We have tried to address two different questions: (i) **can we have subhalos been plausibly detected and are they already present in the Fermi catalog as unidentified sources?** (ii) **how probable is it to detect subhalos without having detected the smooth halo first?** We have not fully answered these questions yet but shall do so just below. However, we have introduced or defined physical and statistical quantities appropriate to help us answer. As well known in the field, the physical quantity that best defines the gamma-ray flux of a dark matter object for an observer on Earth is the J factor, first introduced in [119].

The probability density function of subhalo J factors, which is fully determined from the main subhalo characteristics (effective⁶ mass and concentration functions, and spatial distribution after tidal stripping), provides the most important piece of statistical information [see Eq. (42) and Fig. 3]. This was already noticed in *e.g.* [56], but our probability function differs significantly from theirs because we account for tidal stripping, which modifies more naive scaling relations. This probability distribution of J factors actually combines a complex mixture of different elements, each weighted by a specific though intricate probability: apparent size of a subhalo (fixed by angular resolution, position, mass and concentration), its intrinsic luminosity (mass and concentration), and its distance to the observer—all these are affected by tidal effects.

This is of course not enough, since one also needs to figure out what the gamma-ray background is as precisely as possible, in particular its angular distribution. A rather sound model for the background allows us to define the sensitivity to pointlike subhalos, which can be expressed as a threshold J factor. It is denoted $J_{\min}^{(l,b)}$ in this paper [see a simplified definition Eq. (61), and a more statistically rigorous one in Eq. (86)], and depends on Galactic coordinates (l, b) via the background. It defines the J factor necessary for a pointlike subhalo to fluctuate above

⁶Effective because they depend both on cosmological input functions (initial conditions) and on tidal stripping.

the background emission significantly enough to be detected. That sensitivity to pointlike subhalos is closely related to the point-source flux sensitivity, more familiar to gamma-ray astronomers and defined in Eq. (62). The accurate calculation of $J_{\min}^{(l,b)}$ is the key element to answer to question (i) above. Once it is calculated over the full sky (see the right panels of Fig. 6), one can easily derive the expected number of visible subhalos by integrating the probability density of subhalo J factors above $J_{\min}^{(l,b)}$ over the full sky (see Fig. 3, where the green vertical thick line piles up the values of J_{\min} in all directions).

We have explored the dependence of J_{\min} on the main physical parameters with a simplified statistical method in Sect. VC2, and confirmed our results from a full likelihood analysis performed on mock data in Sect. VC4. We can summarize the main dependencies as follows:

- $\langle\sigma v\rangle$: The sensitivity to subhalos increases linearly with $\langle\sigma v\rangle$ (*i.e.* $J_{\min} \tilde{\propto} 1/\langle\sigma v\rangle$) in a baryonic background domination, but only $\tilde{\propto} \sqrt{\langle\sigma v\rangle}$ when the DM-induced diffuse background becomes important as well. In contrast, the point-source flux sensitivity ϕ_{\min} is independent of $\langle\sigma v\rangle$ in a baryonic background domination, and degrades like $\tilde{\propto} \sqrt{\langle\sigma v\rangle}$ when the DM-induced diffuse background takes over. These scaling relations assume that the Poissonian regime is reached.
- α : Interestingly enough, the sensitivity to subhalos slightly *degrades* if the initial mass function slope $\alpha > 1.9$, because this increases the relative fraction of light (hence faint) subhalos with respect to heavier (hence brighter) ones, and thereby increases the contribution of unresolved subhalos to the diffuse emission (said differently, this increases the annihilation boost factor which contributes as an additional diffuse background). See an illustration in Fig. 5.
- m_{\min} : The impact of the cutoff virial mass m_{\min} is only important for $\alpha > 1.9$. Then, decreasing m_{\min} *degrades* the sensitivity to pointlike subhalos because this increases the background diffuse emission induced by unresolved subhalos, as explained just above.

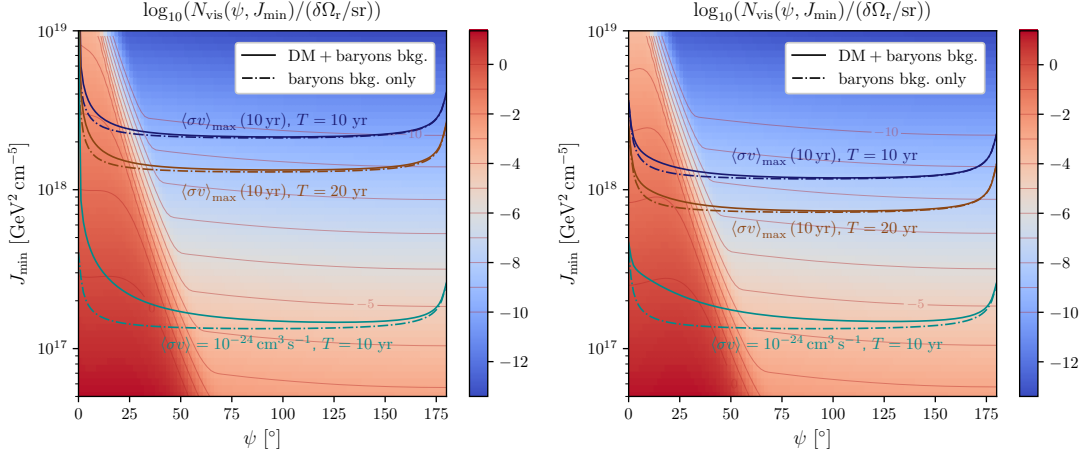
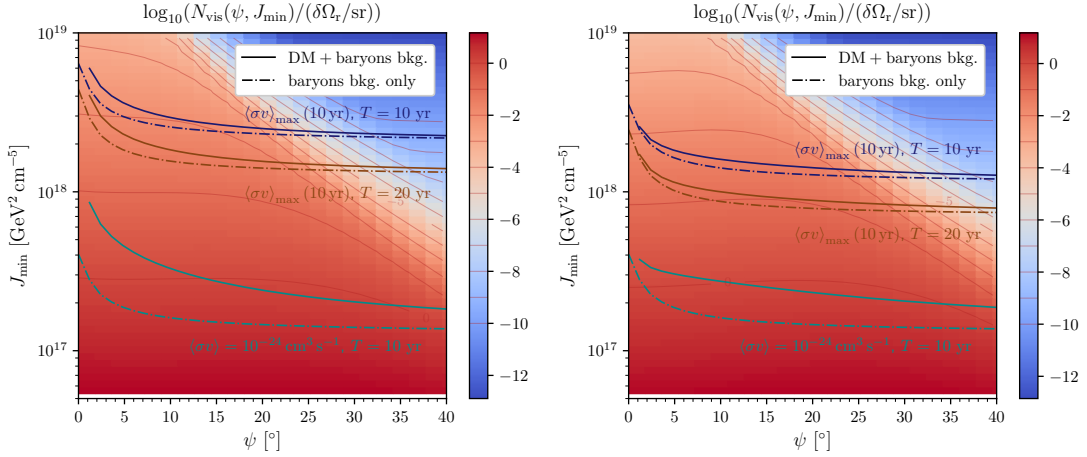
Some other characteristics (most probable distances, masses, concentrations) are further illustrated in the appendix, see Appendix C. They significantly depend on the angular resolution considered to define the pointlike character. By the way, extending the angular resolution beyond its nominal value of $\theta_r = 0.1^\circ$ in our calculations might be a way to address the sensitivity to extended objects.

We provide final summary results in Fig. 10, in which the left (right) panels deal with a subhalo population model embedded within a global NFW (cored, respectively) Galactic halo. Top panels show sensitivity curves $J_{\min}^{(l,b)}$ [with $(l, b) = (0^\circ, \psi) | (180^\circ, \psi - 180^\circ)$] as functions

of the line-of-sight angle to the Galactic center ψ , in addition to the angular distribution of subhalos above a given threshold J_{\min} (colored vertical scale and associated isolines). The $J_{\min}^{(l,b)}$ curves are calculated from different assumptions for the annihilation cross section and for the observation time — $\langle\sigma v\rangle_{\max}(10\text{ yr})$ (dark blue and brownish curves), which corresponds to the 3σ limit on $\langle\sigma v\rangle$ derived from Eq. (79) ($\approx 6 \times 10^{-26}\text{ cm}^3/\text{s}$, see Fig. 7), and an unrealistically large $\langle\sigma v\rangle = 10^{-24}\text{ cm}^3/\text{s}$ (cyan curves); for $T = 10$ (dark blue and cyan curves) or 20 yr (brownish curves). Two background configurations are assumed: baryonic background only (the DM contribution to the diffuse emission is unplugged—dot-dashed curves), and the complete background comprising both the baryonic and the DM-induced diffuse emissions (solid curves). All results assume WIMPs of 100 GeV annihilating into $\tau^+\tau^-$. These curves are inferred from the likelihood method introduced in Sect. VC4, with the biased background parameters fixed to a degraded efficiency of $\varepsilon_{\text{rec}} = 0.7$ and a Gaussian penalty of $\sigma_b = 0.1$. These parameters artificially introduce a systematic mismodeling of the baryonic background and are tuned to match the limits obtained by the Fermi Collaboration on real data reasonably well, consistently with the analysis performed in Ref. [84]. The experimental angular resolution is fixed to $\theta_r = 0.1^\circ$ —see the corresponding plots for $\theta_r = 1^\circ$ in Fig. 11. Middle panels are just zoomed versions of the top panels in the range $\psi \in [0^\circ, 40^\circ]$. Bottom panels show the corresponding averaged angular distributions of pointlike subhalos above $J_{\min}^{(l,b)}$, *i.e.* the visible subhalos (provided the integrated number exceeds 1). These angular distributions can be read off from the upper panels by looking at the background color gradient along the $J_{\min}^{(l,b)}$ curves.

Varying the background has almost no effect because the DM parameters are such that the baryonic background always dominate (sizable differences can only be seen in the case on the unrealistically large $\langle\sigma v\rangle$). For reasonable values of $\langle\sigma v\rangle$, we see that the global halo shape has no strong impact on the angular profile of detectable subhalos, with a peak found around $\sim 20^\circ$ falling sharply at larger angles, which strongly limits the angular search window. Still, the global halo shape has slightly more impact on the global distribution amplitude, making it slightly more probable to detect subhalos if they are embedded in cored Galactic halo. As seen in Fig. 11 though, increasing the angular resolution to 1° has a more spectacular impact, since this strongly extends the angular distribution of visible pointlike subhalos, and also increases the associated amplitude in both the NFW and the cored Galactic halo cases. This might tend to indicate that searches for extended objects are a better strategy than searches for pointlike ones.

We further quantify our results in Table II, where we fully integrate over the statistical ensemble. We provide our predictions for the total number of visible subhalos and its 95% C.L. range assuming several configurations for DM, the background, and the observation time. DM

Global NFW Galactic halo ($\theta_r = 0.1^\circ$)Global cored Galactic halo ($\theta_r = 0.1^\circ$)Angular distribution of subhalos above a given J_{\min} (colored), predicted J_{\min} (curves), and iso- $\log_{10}(N_{\text{vis}})$ Same as above zoomed in the range $\psi \in [0^\circ, 40^\circ]$ 

Corresponding angular distributions of visible subhalos

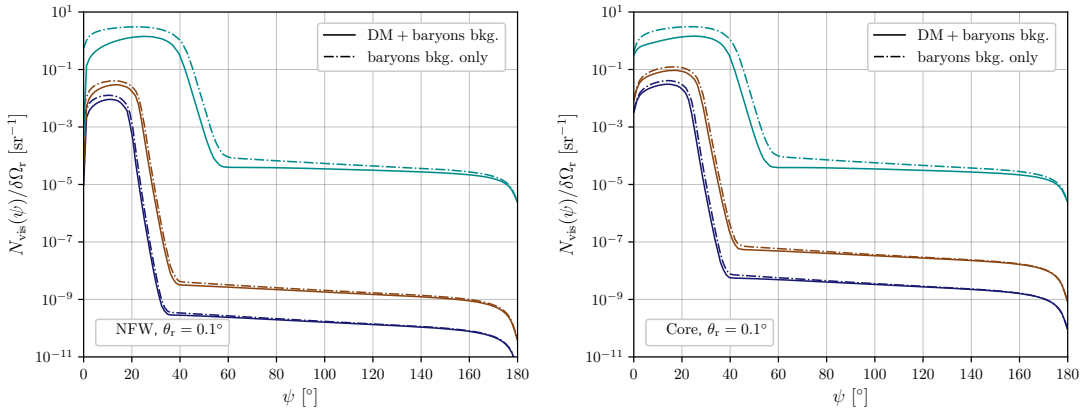
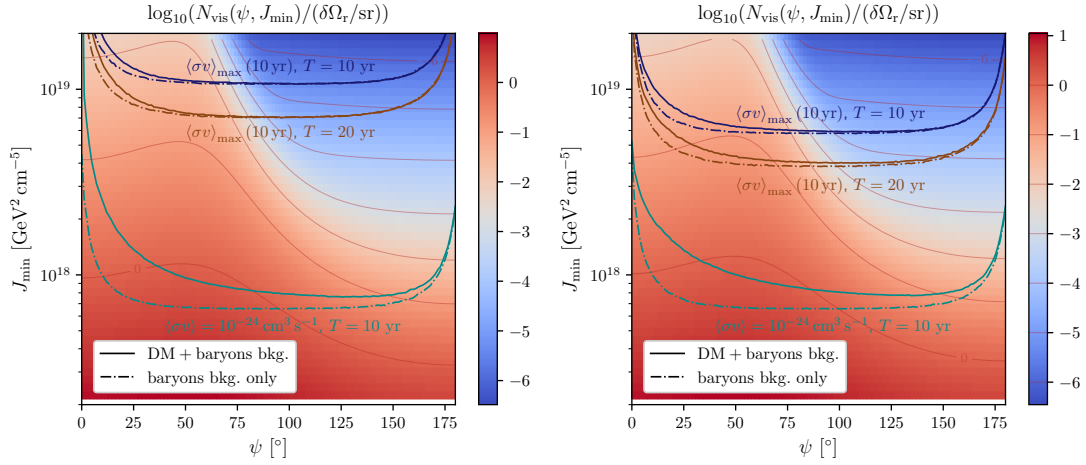
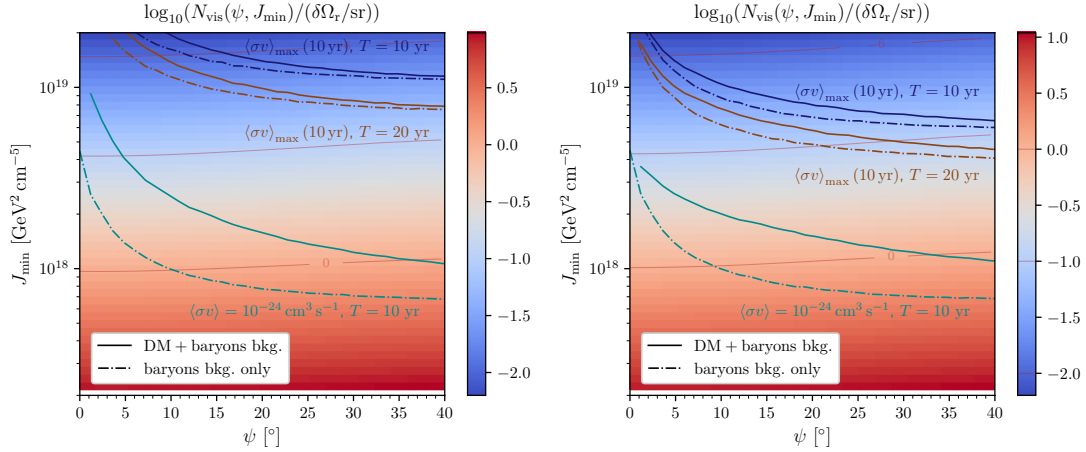
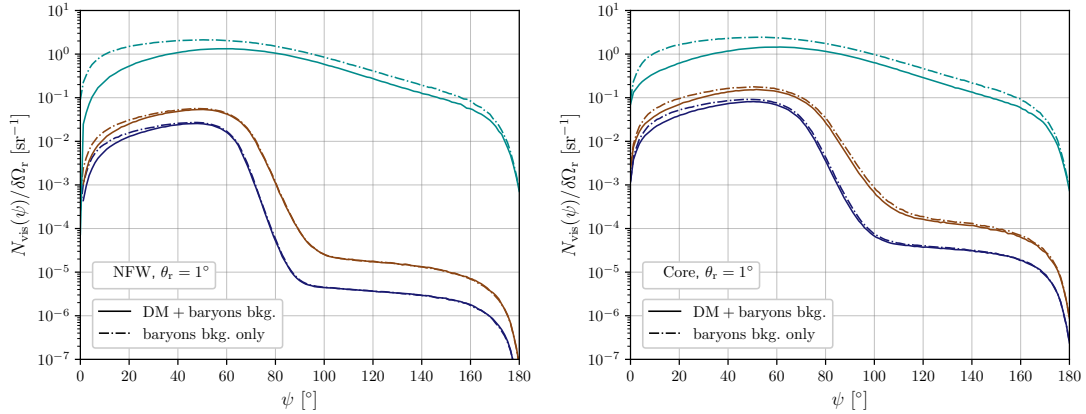


FIG. 10. Angular profile of visible pointlike subhalos ($J > J_{\min}^{(l,b)}$) assuming $\theta_r = 0.1^\circ$ for a global NFW (left panels) or cored halo (right panels). Subhalo parameters are set to $(\alpha, m_{\min}/M_\odot, \epsilon_t) = (1.9, 10^{-10}, 0.01)$. The J_{\min} curves assume $\langle\sigma v\rangle$ fixed to its 3σ limit for 10 yr or to an already excluded value of $10^{24} \text{ cm}^3/\text{s}$ for a 100 GeV WIMP annihilating into $\tau^+\tau^-$. Observation times of 10 and 20 yr are considered. **Top panels:** Angular distribution of subhalo J factors (colored), J_{\min} curves ($l = 0^\circ, 180^\circ$), and iso- $\log_{10} N_{\text{vis}}$. **Middle panels:** Zoom in the $\psi \in [0^\circ - 40^\circ]$ range. **Bottom panels:** Two-dimensional projection.

is taken in the form of WIMPs of 100 GeV or 1 TeV, distributed according to an NFW or a cored halo, an-

Global NFW Galactic halo ($\theta_r = 1^\circ$)Global cored Galactic halo ($\theta_r = 1^\circ$)Angular distribution of subhalos above a given J_{\min} (colored), predicted J_{\min} (curves), and iso- $\log_{10}(N_{\text{vis}})$ Same as above zoomed in the range $\psi \in [0^\circ, 40^\circ]$ 

Corresponding angular distributions of visible subhalos

FIG. 11. Same as Fig. 10 for an angular resolution of $\theta_r = 1^\circ$.

ihilating into $b\bar{b}$ or $\tau^+\tau^-$, and with a cross section set to the 3σ limit on the diffuse DM signal corresponding to 10 or 20 yr of unsuccessful observation (see Fig. 7). To derive the number of detectable subhalos, we have as-

sumed an observation time of 10 or 20 yr. In the former case, we have fixed the annihilation cross section to the 10-yr limit for the diffuse signal, and in the later case, to either the 10- or 20-yr limit. A cross section set to the 10-

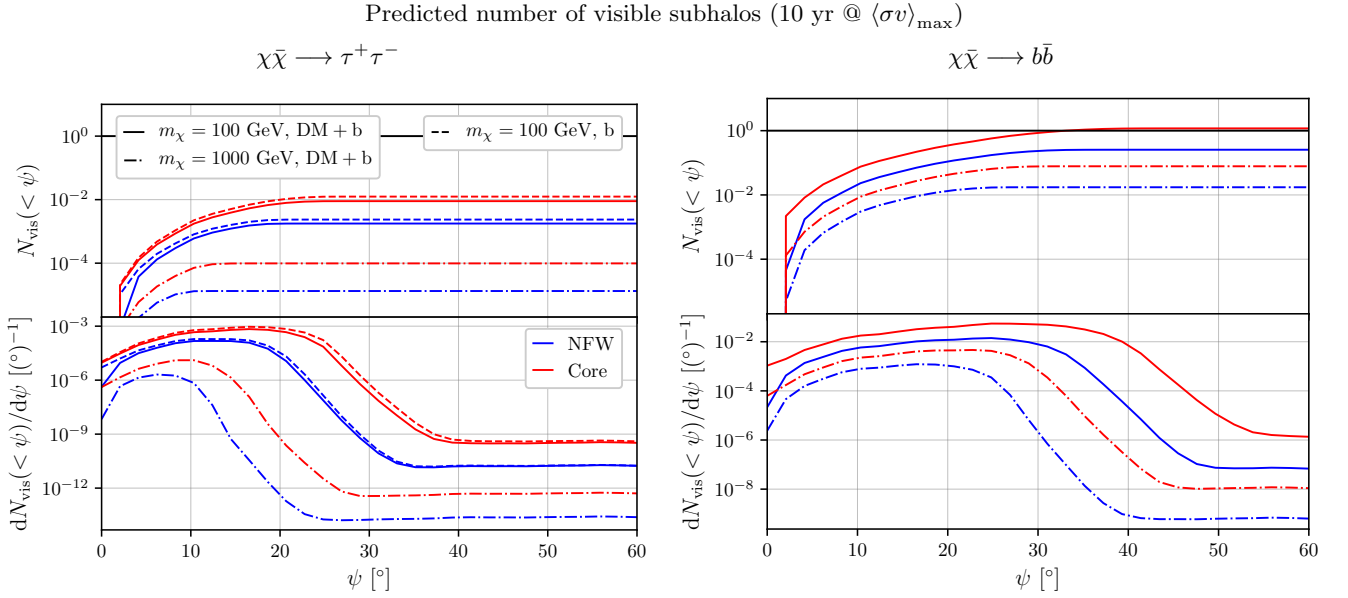


FIG. 12. Predicted number of visible subhalos based on likelihood analyses on mock data generated for an observation time of 10 yr. Top (bottom) parts of the plots show the integrated (differential) number as a function of the line-of-sight angle ψ , for different WIMP benchmark models. The annihilation cross section is fixed to its 3σ limit assuming the nondetection of the smooth halo (see Fig. 7). **Left panel:** $\tau^+\tau^-$ annihilation channel. **Right panel:** $b\bar{b}$ channel.

TABLE II. Number of visible subhalos and 95% confidence interval assuming angular resolutions of $\theta_r = 0.1^\circ$ and 1° , and different WIMP models. Mock data are generated with the background model given in Eq. (49), and the subhalo sensitivity is evaluated using the likelihood bias parameters $\varepsilon_{\text{rec}} = 0.7$ and $\sigma_b = 0.1$ in the 1 – 100 GeV energy range (5 logarithmic bins). The subhalo configuration is $(\alpha, m_{\text{min}}/M_\odot, \epsilon_t) = (1.9, 10^{-10}, 0.01)$, *i.e.* it describes a population of subhalos rather resilient to tidal stripping.

$\frac{m_\chi}{[\text{GeV}]}$	channel	bkg.	$\frac{T}{[\text{yr}]}$	$\theta_r = 0.1^\circ$						$\theta_r = 1^\circ$					
				NFW			Core			NFW			Core		
				$N_{95\%}^-$	N_{vis}	$N_{95\%}^+$	$N_{95\%}^-$	N_{vis}	$N_{95\%}^+$	$N_{95\%}^-$	N_{vis}	$N_{95\%}^+$	$N_{95\%}^-$	N_{vis}	$N_{95\%}^+$
100	$\tau^+\tau^-$	DM+b	10*	0	1.8×10^{-3}	0.60	0	8.96×10^{-3}	0.80	0	4.97×10^{-2}	1.19	0	0.16	1.71
100	$\tau^+\tau^-$	b only	10*	0	2.4×10^{-3}	0.63	0	1.25×10^{-2}	0.85	0	5.44×10^{-2}	1.22	0	0.19	1.81
100	$b\bar{b}$	DM+b	10*	0	0.26	2.04	0	1.18	4.2	0	1.26	4.33	0	3.69	8.35
1000	$b\bar{b}$	DM+b	10*	0	1.73×10^{-2}	0.92	0	7.80×10^{-2}	1.35	0	0.20	1.84	0	0.57	2.88
1000	$\tau^+\tau^-$	DM+b	10*	0	1.3×10^{-5}	0.34	0	9.8×10^{-5}	0.41	0	4.2×10^{-3}	0.69	0	1.85×10^{-2}	0.93
100	$b\bar{b}$	DM+ b	20†	0	1.80	5.31	0.14	3.98	8.80
100	$b\bar{b}$	DM+ b	20*	0	3.32	7.80	1.22	5.95	11.60

* Using $\langle\sigma v\rangle_{\max}(10 \text{ yr})$ for the corresponding channel.

† Using $\langle\sigma v\rangle_{\max}(20 \text{ yr})$ for the corresponding channel.

yr limit together with a 20-yr observation time suppose that the diffuse DM signal has been detected for long a the time of subhalo searches. We adopt nominal parameters for the resilient subhalo population model, and use not only the nominal angular resolution of $\theta_r = 0.1^\circ$ for pointlike subhalo searches, but also a more extended one of $\theta_r = 1^\circ$ to try to capture the potential reach of extended subhalo searches. Our main results, which are illustrated in Fig. 12 in terms of angular distributions of visible subhalos for different model configurations, can be summarized as follows:

- In most cases, the number of visible subhalos is presently $N_{\text{vis}} < 1$ at 95% C.L.
- The most optimistic case for a 10-yr search of pointlike subhalos (nominal resolution angle) is found for $m_\chi = 100$ GeV annihilating into $b\bar{b}$, for which $N_{\text{vis}} < 5$ (3) at 95% C.L. for a cored (NFW) Galactic halo. In that case $N_{\text{vis}} = 0$ is still part of the 95% C.L. range.
- Extending the analysis to 20 yr (same annihilation cross section), we find a minor improvement with $N_{\text{vis}} < 6$ (cored halo), though still consistent with 0 at 95% C.L.
- Increasing the angular resolution to $\theta_r = 1^\circ$ slightly increases the statistics by adding bigger objects, which tends to show that there is a little bonus to

be gained from extended source searches.

- If to be hunted somewhere, subhalos should better be looked for in a latitude band extending from $\sim \pm 10^\circ$ to $\sim \pm 40^\circ$, and in a longitude band centered about 0° . With an angular resolution of 0.1° ($1'$), visible subhalos should have tidal masses of $\sim 10^4$ - $10^5 M_\odot$ ($\sim 10^6$ - $10^7 M_\odot$) and be located at a distance of ~ 10 kpc (~ 10 - 20 kpc) from Earth—see Appendix C.

Based on these results, we conclude that it is unlikely that some of the unidentified sources of the Fermi catalog actually be Galactic subhalos; this might also hold for extended subhalo searches, if our large angular resolution example is confirmed to be a reasonable proxy for this complementary search window. The only configuration which may allow for subhalo detection is the cored halo case, owing to a reduced diffuse signal [detecting ≥ 1 subhalo has a p value of ~ 0.7 from Eq. (53)]. Note that these statements are based upon a likelihood analysis of idealized mock data generated from a background model that underestimates the genuine DGE (see Fig. 4), especially within the inner 10 - 40° from the GC, and that also leads to a slight underestimate of the current limits on $\langle\sigma v\rangle$ (see Fig. 7). Therefore, despite the rather pessimistic prospects for subhalo detection, these can be still considered as lying on the optimistic side of possible predictions..

Another consequence of these limited detection perspectives is that further including subhalos to derive limits on the annihilation cross section, though necessary for self-consistency reasons, is not expected to significantly tighten those derived from the analysis of the diffuse Galactic emission only; neither from the absence of any individual detection, nor from their diffuse contribution which is lower than that of the smooth halo component at latitudes $\sim 10^\circ$ - 15° (which can otherwise be expressed as having a negligible subhalo boost factor in the central Galactic regions). This answers to the question (i) raised above.

Finally, we have also defined a quantity, J_{\min}^{crit} [see Eq. (71) for the definition in the simplified statistical analysis, and Eq. (87) for the more rigorous one], which corresponds to the detection threshold $J_{\min}^{(l,b)}$ evaluated at the 3σ limit cross section of the current (or future) observational time. That quantity formally allows us to answer to the question (ii) because it characterizes the critical J factor threshold below which the diffuse signal should be detected before any pointlike subhalo. By comparing the flattish curves obtained for J_{\min}^{crit} in Fig. 8 with the probability density function of subhalo J factors in Fig. 3, we can readily claim that it is much more likely to detect the smooth halo before subhalos in the different configurations we have explored so far. Indeed, if the threshold $J_{\min}^{(l,b)}$ curves in Fig. 8 cross the J_{\min}^{crit} ones, that means that the smooth halo should have already been detected. We see from our results that $J_{\min}^{(l,b)}$ should def-

initely decrease below J_{\min}^{crit} in order to get a guaranteed sizable number of detectable subhalos.

What kind of physical effects could we think of to more optimistically change these conclusions? First of all, let us recall that our subhalo population model is on the optimistic side, since it is based on assuming a significant resilience to tidal effects (subhalo masses are still depleted by tides, but inner subhalo cusps survive). A systematic increase of the subhalo concentration could make them brighter without changing the more constrained smooth halo contribution. However, increasing the luminosity by a factor of ~ 2 would imply an aggressive change at the level of the width of the concentration distribution function (fully accounted for in our analysis), about 0.15 dex (log-normal distribution), which is not theoretically favored (*e.g.* [137–140]). Moreover, this change would have to mostly affect the mass range of visible subhalos, otherwise it would increase the relative contribution of unresolved subhalos to the diffuse emission, and thereby temper the decrease of $J_{\min}^{(l,b)}$. Finally, one could also think about a distorted primordial spectrum that would inject additional power on the relevant subhalo mass scale, as is the case in the formation of primordial black holes or ultracompact mini-halos (*e.g.* [141, 142]). However, even if possible, that would drive us in the study of a more fine-tuned model, which goes beyond the scope of this paper.

ACKNOWLEDGMENTS

This work has been partly supported by the ANR project ANR-18-CE31-0006, the OCEVU Labex (ANR-11-LABX-0060), the national CNRS-INSU programs PNHE and PNCG, and European Union’s Horizon 2020 research and innovation program under the Marie Skłodowska-Curie Grant Agreements No 690575 and No 674896 – in addition to recurrent funding by CNRS-IN2P3 and the University of Montpellier.

Appendix A: Subhalo model description

Here we provide the details of the global galactic halos derived from fits on stellar kinematic data in Ref. [76]. They are based on the following spherical profile:

$$\rho_{\text{tot}}(R) = \rho_{\odot}^{\text{tot}} \left\{ \frac{R}{R_{\odot}} \right\}^{-\gamma} \left\{ \frac{1+X}{1+X_{\odot}} \right\}^{\gamma-3}, \quad (\text{A1})$$

with $X = R/R_s^{\text{tot}}$, R_s^{tot} the scale radius, $\rho_{\odot}^{\text{tot}}$ the total average DM density in the solar system (including subhalos), and $R_{\odot} = 8.2$ kpc the Sun's distance to the GC. We give additional details on the subhalo population models in Table III.

Appendix B: Best-fitting solutions to the likelihood function

1. Semi-analytical solution (limit on $\langle\sigma v\rangle$ with negligible isotropic background)

This method is suitable for quick analyses of diffuse photons and can formally be used when the rescaling or bias factor α_b applies to the full background, which, for consistency, corresponds in our case to negligible isotropic background cases. The best-fit couple of parameters ($\langle\sigma v\rangle, \hat{\alpha}_b$) that maximizes the likelihood $\mathcal{L}(\langle\sigma v\rangle, \alpha_b)$ [see Eq. (75)] is given as a solution to the following system of equations:

$$\begin{cases} \left. \frac{\partial \mathcal{L}(\langle\sigma v\rangle, \alpha_b)}{\partial \langle\sigma v\rangle} \right|_{(\langle\sigma v\rangle, \hat{\alpha}_b)} = 0 \\ \left. \frac{\partial \mathcal{L}(\langle\sigma v\rangle, \alpha_b)}{\partial \alpha_b} \right|_{(\langle\sigma v\rangle, \hat{\alpha}_b)} = 0 \end{cases}. \quad (\text{B1})$$

Since $\mathcal{L}(\langle\sigma v\rangle, \alpha_b) > 0$, these equations are equivalent to much simpler ones involving the log-likelihood:

$$\begin{cases} \left. \frac{\partial \ln \mathcal{L}(\langle\sigma v\rangle, \alpha_b)}{\partial \langle\sigma v\rangle} \right|_{(\langle\sigma v\rangle, \hat{\alpha}_b)} = 0 \\ \left. \frac{\partial \ln \mathcal{L}(\langle\sigma v\rangle, \alpha_b)}{\partial \alpha_b} \right|_{(\langle\sigma v\rangle, \hat{\alpha}_b)} = 0 \end{cases}. \quad (\text{B2})$$

Inserting the expression of \mathcal{L} given in Eqs. (75) and (74), we get

$$\begin{cases} \sum_{i,j} a_{ij} \left(\frac{n_{ij}}{\langle\sigma v\rangle a_{ij} + \hat{\alpha}_b b_{ij}} - 1 \right) = 0 \\ \sum_{i,j} b_{ij} \left(\frac{n_{ij}}{\langle\sigma v\rangle a_{ij} + \hat{\alpha}_b b_{ij}} - 1 \right) - N_S N_E \frac{\hat{\alpha}_b - \varepsilon_{\text{rec}}}{\sigma_b^2} = 0 \end{cases}. \quad (\text{B3})$$

By a linear combination of these equations, we arrive to

$$\begin{aligned} \sum_{i,j} n_{ij} - \sum_{i,j} \left(\langle\sigma v\rangle a_{ij} + \hat{\alpha}_b b_{ij} \right) \\ - N_S N_E \frac{\hat{\alpha}_b (\hat{\alpha}_b - \varepsilon_{\text{rec}})}{\sigma_b^2} = 0, \end{aligned} \quad (\text{B4})$$

which allows us to compute the value of $\langle\sigma v\rangle$ in terms of $\hat{\alpha}_b$ analytically from the following expression

$$\begin{aligned} \langle\sigma v\rangle = \frac{1}{\sum_{i,j} a_{ij}} \\ \times \left[\sum_{i,j} (n_{ij} - \hat{\alpha}_b b_{ij}) - N_S N_E \frac{\hat{\alpha}_b (\hat{\alpha}_b - \varepsilon_{\text{rec}})}{\sigma_b^2} \right]. \end{aligned} \quad (\text{B5})$$

The best fit is then evaluated numerically by combining Eq. (B5) with one of the two expressions in Eq. (B3). This method is useful for quick analyses in the negligible isotropic background limit, or to test the correct implementation of the numerical algorithm presented in Sect. B3 in the same configuration.

2. Solution to define the sensitivity to pointlike subhalos

Here, we derive the set of equations relevant to the case of pointlike subhalo searches, still when the isotropic background can be neglected (when the bias factor can be applied to the full background). The best-fit value of the null hypothesis (no point source) is obtained by solving

$$\left. \frac{\partial \ln \mathcal{L}(0, \alpha_b; \langle\sigma v\rangle)}{\partial \alpha_b} \right|_{\hat{\alpha}_b} = 0, \quad (\text{B6})$$

which, in this case, corresponds to the solution to the equation

$$\begin{aligned} \sum_{i,j} b_{ij} \left(\frac{n_{ij}}{\langle\sigma v\rangle a_{ij} + \hat{\alpha}_b b_{ij}} - 1 \right) \\ - N_S N_E \frac{\hat{\alpha}_b - \varepsilon_{\text{rec}}}{\sigma_b^2} = 0. \end{aligned} \quad (\text{B7})$$

Then we need to find the global best-fit model denoted $(\hat{J}, \hat{\alpha}_b)$ that is given as a solution of the two combined equations on the derivative of the log-likelihood,

$$\begin{cases} \left. \frac{\partial \ln \mathcal{L}(J, \alpha_b; \langle\sigma v\rangle)}{\partial J} \right|_{(\hat{J}, \hat{\alpha}_b)} = 0 \\ \left. \frac{\partial \ln \mathcal{L}(J, \alpha_b; \langle\sigma v\rangle)}{\partial \alpha_b} \right|_{(\hat{J}, \hat{\alpha}_b)} = 0 \end{cases}. \quad (\text{B8})$$

TABLE III. Main characteristics of the subhalo population models used in this paper. Numbers are calculated using a minimal cutoff mass of $m_{\min} = 10^{-10} M_{\odot}$, and for tidally resilient subhalos with $\epsilon_t = 0.01$. Are provided: N_{tot} the total number of surviving subhalos, and f_{tot} , the total DM mass fraction they contain within the virial radius of the host halo.

Galactic model	$\rho_{\odot}^{\text{tot}}$ [M_{\odot}/pc^3]	R_s^{tot} [kpc]	N_{tot}		f_{tot}	
			$\alpha = 1.9$	$\alpha = 2$	$\alpha = 1.9$	$\alpha = 2$
NFW ($\gamma = 1$)	0.0101	18.6	4.58×10^{18}	2.45×10^{20}	0.16	0.52
Cored ($\gamma = 0$)	0.0103	7.7	4.27×10^{18}	2.25×10^{20}	0.15	0.49

Inserting the expression of \mathcal{L} , we get

$$\begin{cases} \sum_{ij} b_{ij} \left(\frac{n_{ij}}{\langle \sigma v \rangle a_{ij} + \hat{\alpha}_b b_{ij} + c_{ij}^0 \langle \sigma v \rangle \hat{J} \delta_{i_0, i}} - 1 \right) \\ - N_S N_E \frac{\hat{\alpha}_b - \epsilon_{\text{rec}}}{\sigma_b^2} = 0 \\ \sum_{ij} c_{ij}^0 \langle \sigma v \rangle \left(\frac{n_{ij}}{\langle \sigma v \rangle a_{ij} + \hat{\alpha}_b b_{ij} + c_{ij}^0 \langle \sigma v \rangle \hat{J} \delta_{i_0, i}} - 1 \right) = 0 \end{cases} \quad (\text{B9})$$

This system of coupled equations is actually very hard to solve. A way out is to use the Newton-Raphson algorithm (see below), which is well suited for this kind of problems.

3. The Newton-Raphson algorithm

Here, we summarize our implementation of the Newton-Raphson algorithm, which is a standard likelihood maximization procedure in gamma-ray astronomy [130]. Let us assume a likelihood function given by $\mathcal{L}(\Theta, \Xi)$, where Θ is a set of parameters, from which we are seeking the one, $\hat{\Theta}$, that maximizes \mathcal{L} — Ξ is another set of fixed parameters. Let $\lambda(\Theta, \Xi) = \ln \mathcal{L}(\Theta, \Xi)$ be the corresponding log-likelihood function, and let us seek for the maximum of λ . To proceed, we introduce the gradient vector of λ defined as $\mathcal{D}(\Theta, \Xi) = \nabla_{\Theta} \lambda(\Theta, \Xi)$ such that, by definition, $\mathcal{D}(\hat{\Theta}, \Xi) = 0$. We can now Taylor expand \mathcal{D} around the best-fit point of coordinates $\hat{\Theta}$ as

follows:

$$\begin{aligned} \mathcal{D}(\Theta, \Xi) &= \mathcal{D}(\hat{\Theta}, \Xi) + [(\Theta - \hat{\Theta}) \cdot \nabla_{\Theta}] (\Theta, \Xi) + \dots \\ &= [(\Theta - \hat{\Theta}) \cdot \nabla_{\Theta}] \mathcal{D}(\Theta, \Xi) + \dots \end{aligned} \quad (\text{B10})$$

By massaging this expression—and making explicit in the notation the dependence in (Θ, Ξ) —we find that

$$\begin{aligned} \mathcal{D} &= \mathcal{H}^T (\Theta - \hat{\Theta}) + \dots, \quad (\text{B11}) \\ \text{with } \mathcal{H}_{k\ell} &\equiv \frac{\partial^2 \lambda(\Theta, \Xi)}{\partial \theta_k \partial \theta_{\ell}} \end{aligned}$$

the Hessian matrix defined using the elements $\Theta = (\theta_0, \theta_1, \dots)$. Since the Hessian matrix is real symmetric by definition, by inverting the previous expression we get at first order

$$\hat{\Theta} \simeq \Theta - \mathcal{H}^{-1} \mathcal{D}. \quad (\text{B12})$$

Like in the one-dimensional Newton algorithm, it is possible (provided \mathcal{D} is well behaved) to find $\hat{\Theta}$ simply by starting from an initial value Θ_0 and defining an iterating procedure as follows:

$$\begin{aligned} \hat{\Theta}_{n+1} &\simeq \Theta_n - \mathcal{H}^{-1}(\Theta_n, \Xi) \mathcal{D}(\Theta_n, \Xi) \\ \text{such that } \hat{\Theta} &= \lim_{n \rightarrow \infty} \Theta_n. \end{aligned} \quad (\text{B13})$$

In practice, this converges very fast.

Appendix C: Internal properties of visible subhalos

The most probable tidal masses, concentrations, and distances of visible subhalos are shown in Fig. 13, Fig. 14, and Fig. 15.

-
- [1] P. J. E. Peebles, *ApJ* **263**, L1 (1982).
 - [2] G. R. Blumenthal, S. M. Faber, J. R. Primack, and M. J. Rees, *Nature* **311**, 517 (1984).
 - [3] G. Bertone and D. Hooper, *Reviews of Modern Physics* **90**, 045002 (2018), arXiv:1605.04909.
 - [4] B. W. Lee and S. Weinberg, *Phys. Rev. Lett.* **39**, 165 (1977).
 - [5] J. R. Bond, A. S. Szalay, and M. S. Turner, *Phys. Rev. Lett.* **48**, 1636 (1982).
 - [6] P. Binétruy, G. Girardi, and P. Salati, *Nuclear Physics B* **237**, 285 (1984).
 - [7] M. Srednicki, R. Watkins, and K. A. Olive, *Nuclear Physics B* **310**, 693 (1988).
 - [8] G. F. Giudice, arXiv e-prints (2017), arXiv:1710.07663.
 - [9] G. Arcadi, M. Dutra, P. Ghosh, M. Lindner, Y. Mambrini, M. Pierre, S. Profumo, and F. S. Queiroz, *Eur. Phys. J. C* **78**, 203 (2018), arXiv:1703.07364 [hep-ph].
 - [10] R. K. Leane, T. R. Slatyer, J. F. Beacom, and K. C. Y. Ng, *Phys. Rev. D* **98**, 023016 (2018), arXiv:1805.10305 [hep-ph].

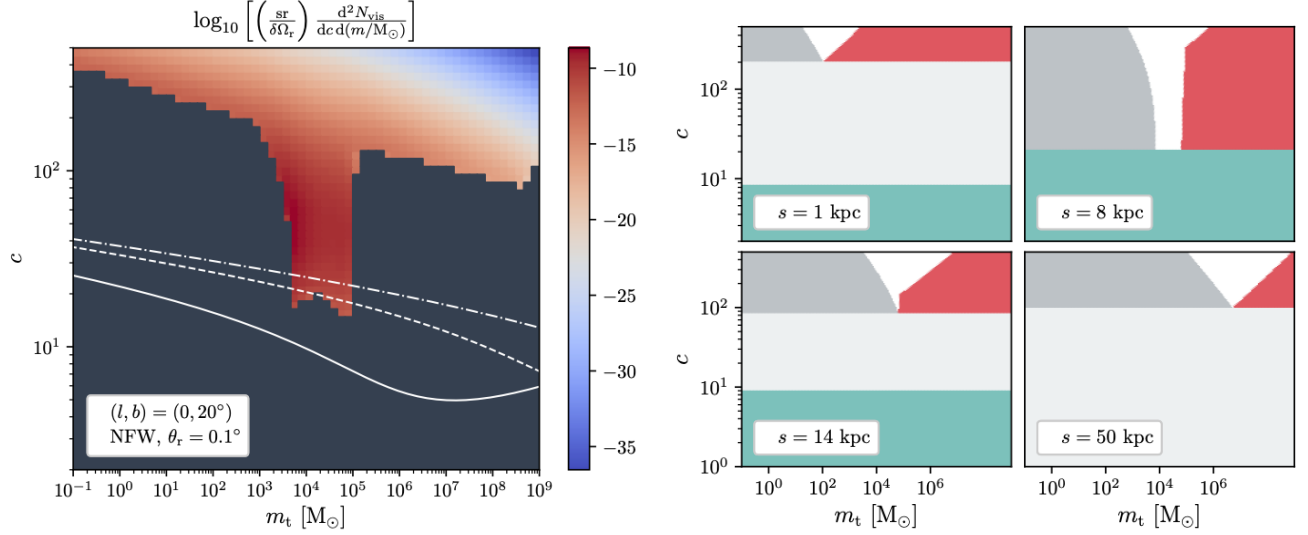
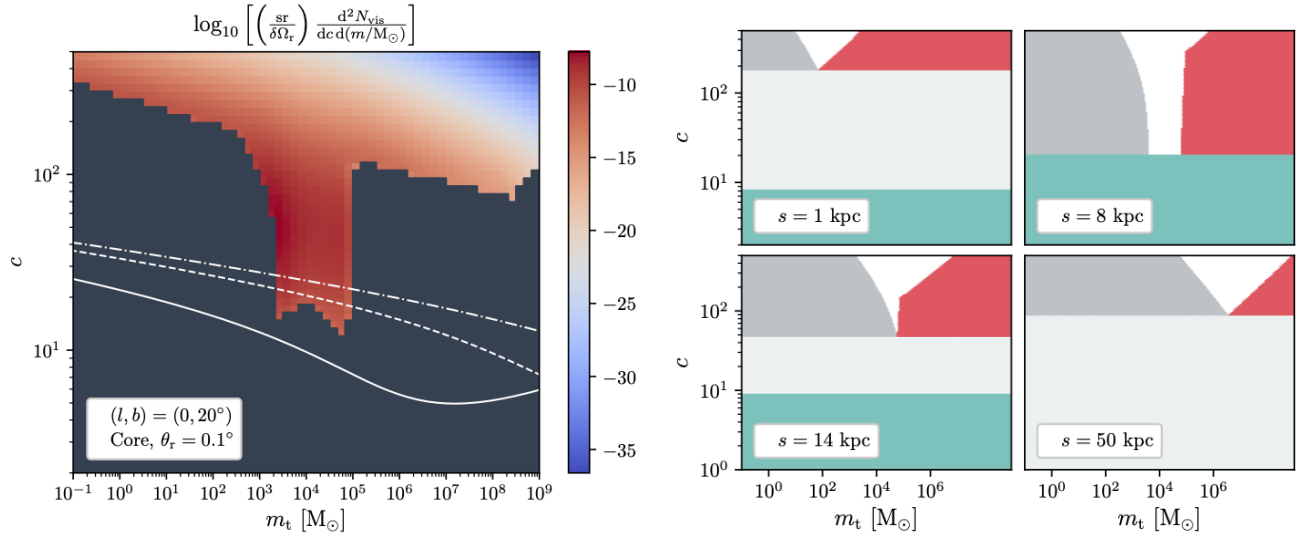
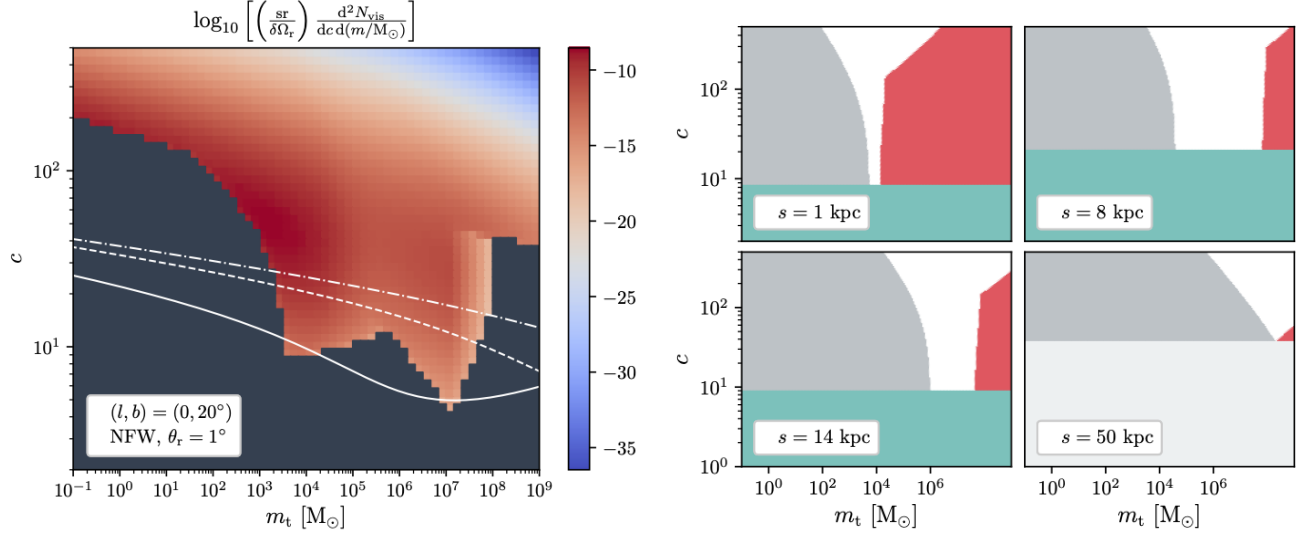
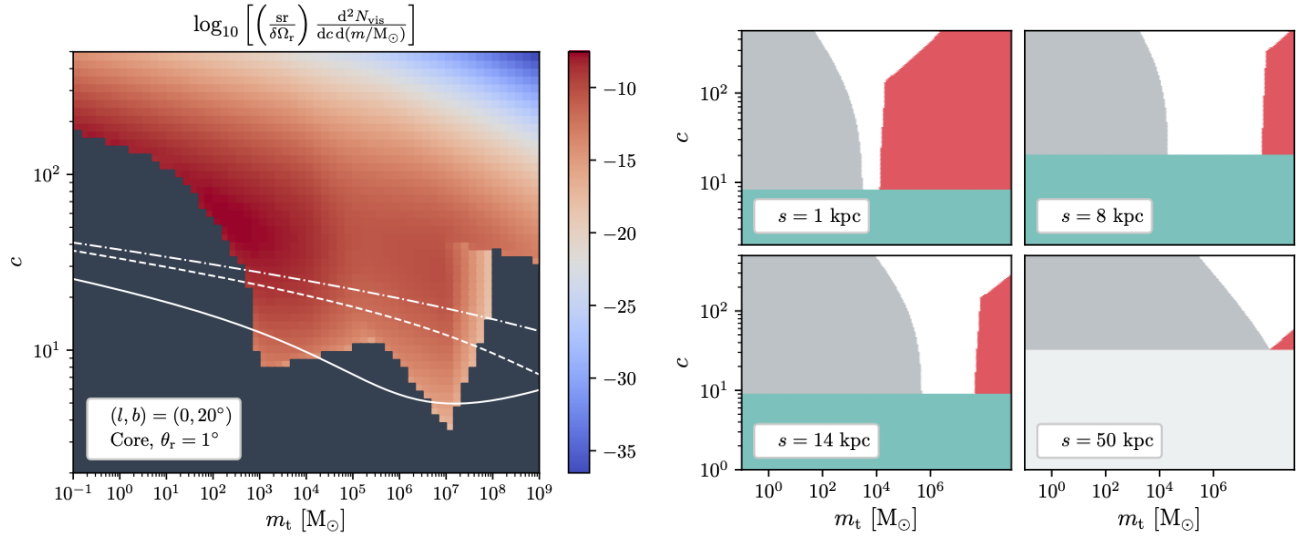
NFW Galactic halo - Properties of subhalos visible with $\theta_r = 0.1^\circ$ Cored Galactic halo - Properties of subhalos visible with $\theta_r = 0.1^\circ$ 

FIG. 13. **Left panels:** Concentrations and physical masses of the most visible subhalos in the direction of Galactic coordinates $(l, b) = (0^\circ, 20^\circ)$. The solid (dashed, dotted-dashed) white curve indicates the median concentration of a subhalo of virial mass m_{200} that would be pruned off down to the tidal mass m_t in abscissa at a galactocentric distance of 1 kpc (10 and 100 kpc, respectively) if tidal disruption were unplugged (though not tidal stripping). This shows that subhalos with a given m_t originate from heavier and heavier objects as they are found closer and closer to the GC (*i.e.* tidal stripping is more and more efficient), should tidal stripping not be destructive—see in comparison the minimal concentration needed to survive tidal effects in the associated right panels. **Right panels:** Exclusion areas for the computation of the probability and for different distances to the observer: subhalos that are not seen as points (red), subhalos that are below the critical/minimal allowed concentration and then tidally disrupted (turquoise— $\epsilon_t = 0.01$), subhalos that are too faint (dark gray on the left), subhalos that are either too faint or not point sources (light gray). Visible: those lying in the white area. **Top panels:** NFW Galactic halo. **Bottom panels:** Cored Galactic halo.

- [11] J. E. Gunn, B. W. Lee, I. Lerche, D. N. Schramm, and G. Steigman, *ApJ* **223**, 1015 (1978).
 [12] J. Silk and M. Srednicki, *Phys. Rev. Lett.* **53**, 624 (1984).
 [13] M. W. Goodman and E. Witten, *Phys. Rev. D* **31**, 3059 (1985).
 [14] J. R. Primack, D. Seckel, and B. Sadoulet, *Annual Review of Nuclear and Particle Science* **38**, 751 (1988).
 [15] G. Jungman, M. Kamionkowski, and K. Griest, *Phys. Rep.* **267**, 195 (1996), [hep-ph/9506380](https://arxiv.org/abs/hep-ph/9506380).
 [16] J. L. Feng, *ARA&A* **48**, 495 (2010), [arXiv:1003.0904](https://arxiv.org/abs/1003.0904) [[astro-ph.CO](https://arxiv.org/abs/astro-ph.CO)].
 [17] L. Bergström, *Reports on Progress in Physics* **63**, 793 (2000), [hep-ph/0002126](https://arxiv.org/abs/hep-ph/0002126).
 [18] J. Lavalle and P. Salati, *Comptes Rendus Physique* **13**, 740 (2012), [arXiv:1205.1004](https://arxiv.org/abs/1205.1004) [[astro-ph.HE](https://arxiv.org/abs/astro-ph.HE)].

NFW Galactic halo - Properties of subhalos visible with $\theta_r = 1^\circ$ Cored Galactic halo - Properties of subhalos visible with $\theta_r = 1^\circ$ FIG. 14. Same as Fig. 13 but with $\theta_r = 1^\circ$.

- [19] T. Bringmann and C. Weniger, *Physics of the Dark Universe* **1**, 194 (2012), arXiv:1208.5481 [hep-ph].
- [20] H. Liu, T. R. Slatyer, and J. Zavala, *Phys. Rev. D* **94**, 063507 (2016), arXiv:1604.02457.
- [21] M. Boudaud, T. Lacroix, M. Stref, and J. Lavalle, *Phys. Rev. D* **99**, 061302 (2019), arXiv:1810.01680 [astro-ph.HE].
- [22] J. D. Lewin and P. F. Smith, *Astroparticle Physics* **6**, 87 (1996).
- [23] K. Freese, M. Lisanti, and C. Savage, *Reviews of Modern Physics* **85**, 1561 (2013), arXiv:1209.3339.
- [24] M. Fairbairn, A. C. Kraan, D. A. Milstead, T. Sjöstrand, P. Skands, and T. Sloan, *Phys. Rep.* **438**, 1 (2007), hep-ph/0611040.
- [25] J. Abdallah *et al.*, *Phys. Dark Univ.* **9**, 8 (2015), arXiv:1506.03116 [hep-ph].
- [26] L. E. Strigari, *Phys. Rep.* **531**, 1 (2013), arXiv:1211.7090 [astro-ph.CO].
- [27] C. Schmid, D. J. Schwarz, and P. Widerin, *Phys. Rev. D* **59**, 043517 (1999), astro-ph/9807257.
- [28] C. Boehm, P. Fayet, and R. Schaeffer, *Physics Letters B* **518**, 8 (2001), astro-ph/0012504.
- [29] X. Chen, M. Kamionkowski, and X. Zhang, *Phys. Rev. D* **64**, 021302 (2001), astro-ph/0103452.
- [30] S. Hofmann, D. J. Schwarz, and H. Stöcker, *Phys. Rev. D* **64**, 083507 (2001), arXiv:astro-ph/0104173 [astro-ph].
- [31] V. Berezhinsky, V. Dokuchaev, and Y. Eroshenko, *Phys. Rev. D* **68**, 103003 (2003), astro-ph/0301551.
- [32] A. M. Green, S. Hofmann, and D. J. Schwarz, *MNRAS* **353**, L23 (2004), astro-ph/0309621.
- [33] E. Bertschinger, *Phys. Rev. D* **74**, 063509 (2006), astro-ph/0607319.
- [34] T. Bringmann and S. Hofmann, *J. Cosmology Astropart. Phys.* **4**, 016 (2007), hep-ph/0612238.
- [35] W. H. Press and P. Schechter, *ApJ* **187**, 425 (1974).

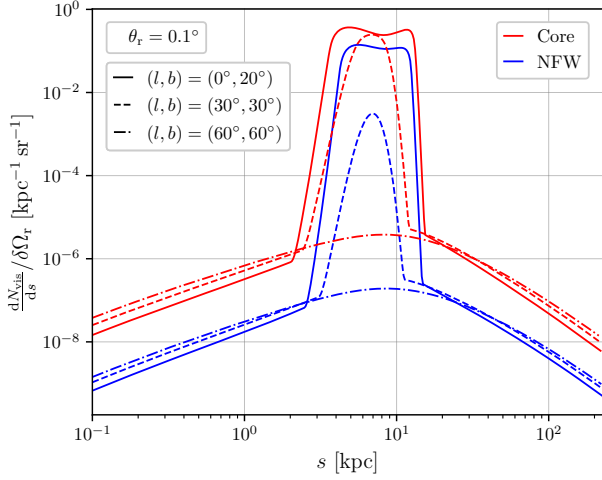


FIG. 15. Distance distribution of the visible subhalos (from the observer), for different pointing directions. This corresponds to the case in which $J_{\min}^{(l,b)}$ is computed assuming $\langle\sigma v\rangle_{\max}(10\text{ yr})$, $\chi\bar{\chi} \rightarrow b\bar{b}$, $\theta_r = 0.1$, and an observation time of 20 yr (the smooth halo should have already been detected).

- [36] J. R. Bond, S. Cole, G. Efstathiou, and N. Kaiser, *ApJ* **379**, 440 (1991).
- [37] C. Lacey and S. Cole, *MNRAS* **262**, 627 (1993).
- [38] J. Diemand, B. Moore, and J. Stadel, *Nature* **433**, 389 (2005), [astro-ph/0501589](#).
- [39] T. Ishiyama, J. Makino, and T. Ebisuzaki, *ApJ* **723**, L195 (2010), [arXiv:1006.3392 \[astro-ph.CO\]](#).
- [40] V. S. Berezhinsky, V. I. Dokuchaev, and Y. N. Eroshenko, *Physics Uspekhi* **57**, 1 (2014), [arXiv:1405.2204 \[astro-ph.HE\]](#).
- [41] M. Stref and J. Lavalley, *Phys. Rev. D* **95**, 063003 (2017), [arXiv:1610.02233](#).
- [42] T. Ishiyama and S. Ando, *MNRAS* **492**, 3662 (2020), [arXiv:1907.03642 \[astro-ph.CO\]](#).
- [43] J. Silk and A. Stebbins, *ApJ* **411**, 439 (1993).
- [44] L. Bergström, J. Edsjö, P. Gondolo, and P. Ullio, *Phys. Rev. D* **59**, 043506 (1999), [astro-ph/9806072](#).
- [45] J. Lavalley, J. Pochon, P. Salati, and R. Taillet, *A&A* **462**, 827 (2007), [arXiv:astro-ph/0603796](#).
- [46] J. Lavalley, Q. Yuan, D. Maurin, and X.-J. Bi, *A&A* **479**, 427 (2008), [arXiv:0709.3634](#).
- [47] L. Pieri, J. Lavalley, G. Bertone, and E. Branchini, *Phys. Rev. D* **83**, 023518 (2011), [arXiv:0908.0195 \[astro-ph.HE\]](#).
- [48] S. Ando and E. Komatsu, *Phys. Rev. D* **73**, 023521 (2006), [astro-ph/0512217](#).
- [49] M. Fornasa, A. Cuoco, J. Zavala, J. M. Gaskins, M. A. Sánchez-Conde, G. Gomez-Vargas, E. Komatsu, T. Linden, F. Prada, F. Zandanel, and A. Morselli, *Phys. Rev. D* **94**, 123005 (2016), [arXiv:1608.07289 \[astro-ph.HE\]](#).
- [50] A. Tasitsiomi and A. V. Olinto, *Phys. Rev. D* **66**, 083006 (2002), [astro-ph/0206040](#).
- [51] F. Stoehr, S. D. M. White, V. Springel, G. Tormen, and N. Yoshida, *MNRAS* **345**, 1313 (2003), [astro-ph/0307026](#).
- [52] R. Aloisio, P. Blasi, and A. V. Olinto, *ApJ* **601**, 47 (2004), [astro-ph/0206036](#).
- [53] L. Pieri, E. Branchini, and S. Hofmann, *Phys. Rev. Lett.* **95**, 211301 (2005), [astro-ph/0505356](#).
- [54] M. Kuhlen, J. Diemand, and P. Madau, *ApJ* **686**, 262 (2008), [arXiv:0805.4416](#).
- [55] B. Anderson, M. Kuhlen, J. Diemand, R. P. Johnson, and P. Madau, *ApJ* **718**, 899 (2010), [arXiv:1006.1628 \[astro-ph.HE\]](#).
- [56] M. Hütten, C. Combet, G. Maier, and D. Maurin, *J. Cosmology Astropart. Phys.* **9**, 047 (2016), [arXiv:1606.04898 \[astro-ph.HE\]](#).
- [57] E. A. Baltz and L. Wai, *Phys. Rev. D* **70**, 023512 (2004), [astro-ph/0403528](#).
- [58] The Fermi-LAT Collaboration, *ApJS* **218**, 23 (2015), [arXiv:1501.02003 \[astro-ph.HE\]](#).
- [59] The Fermi-LAT collaboration, *arXiv e-prints* (2019), [arXiv:1902.10045 \[astro-ph.HE\]](#).
- [60] A. V. Belikov, M. R. Buckley, and D. Hooper, *Phys. Rev. D* **86**, 043504 (2012), [arXiv:1111.2613 \[hep-ph\]](#).
- [61] B. Bertoni, D. Hooper, and T. Linden, *J. Cosmology Astropart. Phys.* **12**, 035 (2015), [arXiv:1504.02087 \[astro-ph.HE\]](#).
- [62] D. Schoonenberg, J. Gaskins, G. Bertone, and J. Diemand, *J. Cosmology Astropart. Phys.* **2016**, 028 (2016), [arXiv:1601.06781 \[astro-ph.HE\]](#).
- [63] N. Mirabal, E. Charles, E. C. Ferrara, P. L. Gonthier, A. K. Harding, M. A. Sánchez-Conde, and D. J. Thompson, *ApJ* **825**, 69 (2016), [arXiv:1605.00711 \[astro-ph.HE\]](#).
- [64] D. Hooper and S. J. Witte, *J. Cosmology Astropart. Phys.* **4**, 018 (2017), [arXiv:1610.07587 \[astro-ph.HE\]](#).
- [65] F. Calore, V. De Romeri, M. Di Mauro, F. Donato, and F. Marinacci, *Phys. Rev. D* **96**, 063009 (2017), [arXiv:1611.03503 \[astro-ph.HE\]](#).
- [66] F. Calore, M. Hütten, and M. Stref, *Galaxies* **7**, 90 (2019), [arXiv:1910.13722 \[astro-ph.HE\]](#).
- [67] D. Glawion, D. Malyshev, E. Moulin, L. Oakes, L. Rinchiuso, and A. Viana, *arXiv e-prints* (2019), [arXiv:1909.01072 \[astro-ph.HE\]](#).
- [68] J. Coronado-Blázquez, M. A. Sánchez-Conde, A. Domínguez, A. Aguirre-Santaella, M. Di Mauro, N. Mirabal, D. Nieto, and E. Charles, *J. Cosmology Astropart. Phys.* **2019**, 020 (2019), [arXiv:1906.11896 \[astro-ph.HE\]](#).
- [69] J. Coronado-Blázquez, M. A. Sánchez-Conde, M. Di Mauro, A. Aguirre-Santaella, I. Ciucă, A. Domínguez, D. Kawata, and N. Mirabal, *J. Cosmology Astropart. Phys.* **2019**, 045 (2019), [arXiv:1910.14429 \[astro-ph.HE\]](#).
- [70] N. Hiroshima, S. Ando, and T. Ishiyama, *Phys. Rev. D* **97**, 123002 (2018), [arXiv:1803.07691](#).
- [71] R. Bartels and S. Ando, *Phys. Rev. D* **92**, 123508 (2015), [arXiv:1507.08656](#).
- [72] J. Zavala and N. Afshordi, *MNRAS* **441**, 1329 (2014), [arXiv:1311.3296](#).
- [73] A. J. Benson, *New A* **17**, 175 (2012), [arXiv:1008.1786](#).
- [74] F. C. van den Bosch, G. Tormen, and C. Giocoli, *MNRAS* **359**, 1029 (2005), [astro-ph/0409201](#).
- [75] J. Zavala and C. S. Frenk, *Galaxies* **7**, 81 (2019), [arXiv:1907.11775 \[astro-ph.CO\]](#).
- [76] P. J. McMillan, *MNRAS* **465**, 76 (2017), [arXiv:1608.00971](#).

- [77] M. Hütten, M. Stref, C. Combet, J. Lavallo, and D. Maurin, *Galaxies* **7**, 60 (2019), arXiv:1904.10935 [astro-ph.HE].
- [78] A. Charbonnier, C. Combet, and D. Maurin, *Computer Physics Communications* **183**, 656 (2012), arXiv:1201.4728 [astro-ph.HE].
- [79] M. Hütten, C. Combet, and D. Maurin, *Computer Physics Communications* **235**, 336 (2019), arXiv:1806.08639.
- [80] T. Kelley, J. S. Bullock, S. Garrison-Kimmel, M. Boylan-Kolchin, M. S. Pawlowski, and A. S. Graus, *MNRAS* **487**, 4409 (2019), arXiv:1811.12413.
- [81] The Fermi-LAT Collaboration, *J. Cosmology Astropart. Phys.* **4**, 014 (2010), arXiv:1002.4415.
- [82] M. Cirelli, P. Panci, and P. D. Serpico, *Nucl.Phys.* **B840**, 284 (2010), arXiv:0912.0663 [astro-ph.CO].
- [83] S. Blanchet and J. Lavallo, *J. Cosmology Astropart. Phys.* **11**, 021 (2012), arXiv:1207.2476 [astro-ph.HE].
- [84] The Fermi-LAT Collaboration, *ApJ* **761**, 91 (2012), arXiv:1205.6474 [astro-ph.CO].
- [85] R. Essig, E. Kuflik, S. D. McDermott, T. Volansky, and K. M. Zurek, *Journal of High Energy Physics* **11**, 193 (2013), arXiv:1309.4091 [hep-ph].
- [86] M. Cirelli, T. Hambye, P. Panci, F. Sala, and M. Taoso, *J. Cosmology Astropart. Phys.* **10**, 026 (2015), arXiv:1507.05519 [hep-ph].
- [87] M. Fornasa and M. A. Sánchez-Conde, *Phys. Rep.* **598**, 1 (2015), arXiv:1502.02866.
- [88] L. J. Chang, M. Lisanti, and S. Mishra-Sharma, *Phys. Rev. D* **98**, 123004 (2018), arXiv:1804.04132 [astro-ph.CO].
- [89] H. Zhao, *MNRAS* **278**, 488 (1996), astro-ph/9509122.
- [90] J. F. Navarro, C. S. Frenk, and S. D. M. White, *ApJ* **462**, 563 (1996), astro-ph/9508025.
- [91] J. S. Bullock, T. S. Kolatt, Y. Sigad, R. S. Somerville, A. V. Kravtsov, A. A. Klypin, J. R. Primack, and A. Dekel, *MNRAS* **321**, 559 (2001), astro-ph/9908159.
- [92] J. Diemand, M. Kuhlen, P. Madau, M. Zemp, B. Moore, D. Potter, and J. Stadel, *Nature* **454**, 735 (2008), arXiv:0805.1244.
- [93] V. Springel, J. Wang, M. Vogelsberger, A. Ludlow, A. Jenkins, A. Helmi, J. F. Navarro, C. S. Frenk, and S. D. M. White, *MNRAS* **391**, 1685 (2008), arXiv:0809.0898.
- [94] J. Einasto, *Trudy Astrofizicheskogo Instituta Alma-Ata* **5**, 87 (1965).
- [95] J. F. Navarro, E. Hayashi, C. Power, A. R. Jenkins, C. S. Frenk, S. D. M. White, V. Springel, J. Stadel, and T. R. Quinn, *MNRAS* **349**, 1039 (2004), astro-ph/0311231.
- [96] J. F. Navarro, A. Ludlow, V. Springel, J. Wang, M. Vogelsberger, S. D. M. White, A. Jenkins, C. S. Frenk, and A. Helmi, *MNRAS* **402**, 21 (2010), arXiv:0810.1522.
- [97] A. Pontzen and F. Governato, *MNRAS* **421**, 3464 (2012), arXiv:1106.0499 [astro-ph.CO].
- [98] F. Governato, A. Zolotov, A. Pontzen, C. Christensen, S. H. Oh, A. M. Brooks, T. Quinn, S. Shen, and J. Wadsley, *MNRAS* **422**, 1231 (2012), arXiv:1202.0554.
- [99] A. Di Cintio, C. B. Brook, A. V. Macciò, G. S. Stinson, A. Knebe, A. A. Dutton, and J. Wadsley, *MNRAS* **437**, 415 (2014), arXiv:1306.0898 [astro-ph.CO].
- [100] C. Wegg, O. Gerhard, and M. Bieth, *MNRAS* **485**, 3296 (2019), arXiv:1806.09635.
- [101] M. Cautun, A. Benítez-Llambay, A. J. Deason, C. S. Frenk, A. Fattahi, F. A. Gómez, R. J. J. Grand, K. A. Oman, J. F. Navarro, and C. M. Simpson, *MNRAS* **494**, 4291 (2020), arXiv:1911.04557 [astro-ph.GA].
- [102] The Gaia Collaboration, *A&A* **616**, A1 (2018), arXiv:1804.09365.
- [103] A.-C. Eilers, D. W. Hogg, H.-W. Rix, and M. K. Ness, *ApJ* **871**, 120 (2019), arXiv:1810.09466 [astro-ph.GA].
- [104] D. W. Hogg, A.-C. Eilers, and H.-W. Rix, *AJ* **158**, 147 (2019), arXiv:1810.09468 [astro-ph.GA].
- [105] E. D’Onghia, V. Springel, L. Hernquist, and D. Keres, *ApJ* **709**, 1138 (2010), arXiv:0907.3482 [astro-ph.CO].
- [106] Q. Zhu, F. Marinacci, M. Maji, Y. Li, V. Springel, and L. Hernquist, *MNRAS* **458**, 1559 (2016), arXiv:1506.05537.
- [107] Á. Moliné, M. A. Sánchez-Conde, S. Palomares-Ruiz, and F. Prada, *MNRAS* **466**, 4974 (2017), arXiv:1603.04057.
- [108] M. A. Sánchez-Conde and F. Prada, *MNRAS* **442**, 2271 (2014), arXiv:1312.1729.
- [109] E. Hayashi, J. F. Navarro, J. E. Taylor, J. Stadel, and T. Quinn, *ApJ* **584**, 541 (2003), astro-ph/0203004.
- [110] F. C. van den Bosch and G. Ogiya, *MNRAS* **475**, 4066 (2018), arXiv:1801.05427.
- [111] M. D. Weinberg, *AJ* **108**, 1398 (1994), astro-ph/9404015.
- [112] O. Y. Gnedin and J. P. Ostriker, *ApJ* **513**, 626 (1999), astro-ph/9902326.
- [113] J. Peñarrubia, A. J. Benson, M. G. Walker, G. Gilmore, A. W. McConnachie, and L. Mayer, *MNRAS* **406**, 1290 (2010), arXiv:1002.3376.
- [114] N. E. Drakos, J. E. Taylor, and A. J. Benson, *MNRAS* **468**, 2345 (2017), arXiv:1703.07836.
- [115] R. K. Sheth, H. J. Mo, and G. Tormen, *MNRAS* **323**, 1 (2001), astro-ph/9907024.
- [116] A. R. Zentner, *International Journal of Modern Physics D* **16**, 763 (2007), astro-ph/0611454.
- [117] The Planck Collaboration, *A&A* **641**, A6 (2020), arXiv:1807.06209 [astro-ph.CO].
- [118] H. Parkinson, S. Cole, and J. Helly, *MNRAS* **383**, 557 (2008), arXiv:0708.1382.
- [119] L. Bergström, P. Ullio, and J. H. Buckley, *Astroparticle Physics* **9**, 137 (1998), astro-ph/9712318.
- [120] M. R. Buckley and D. Hooper, *Phys. Rev. D* **82**, 063501 (2010), arXiv:1004.1644 [hep-ph].
- [121] The Fermi-LAT Collaboration, *ApJ* **697**, 1071 (2009), arXiv:0902.1089 [astro-ph.IM].
- [122] The Fermi-LAT Collaboration, *ApJ* **750**, 3 (2012), arXiv:1202.4039 [astro-ph.HE].
- [123] M. Cirelli, G. Corcella, A. Hektor, G. Hütsi, M. Kadastik, P. Panci, M. Raidal, F. Sala, and A. Strumia, *J. Cosmology Astropart. Phys.* **3**, 051 (2011), arXiv:1012.4515 [hep-ph].
- [124] W. Atwood *et al.*, arXiv e-prints, arXiv:1303.3514 (2013), arXiv:1303.3514 [astro-ph.IM].
- [125] P. Bruel, T. H. Burnett, S. W. Digel, G. Johannesson, N. Omodei, and M. Wood, arXiv e-prints, arXiv:1810.11394 (2018), arXiv:1810.11394 [astro-ph.IM].
- [126] D. G. Cerdeño, T. Delahaye, and J. Lavallo, *Nuclear Physics B* **854**, 738 (2012), arXiv:1108.1128 [hep-ph].
- [127] G. Steigman, B. Dasgupta, and J. F. Beacom, *Phys. Rev. D* **86**, 023506 (2012), arXiv:1204.3622 [hep-ph].
- [128] T. P. Li and Y. Q. Ma, *ApJ* **272**, 317 (1983).

- [129] S. N. Zhang and D. Ramsden, *Experimental Astronomy* **1**, 145 (1990).
- [130] J. R. Mattox *et al.*, *ApJ* **461**, 396 (1996).
- [131] R. D. Cousins, J. T. Linnemann, and J. Tucker, *Nuclear Instruments and Methods in Physics Research A* **595**, 480 (2008), [physics/0702156](#).
- [132] The Fermi-LAT Collaboration, *Phys. Rev. Lett.* **115**, 231301 (2015), [arXiv:1503.02641 \[astro-ph.HE\]](#).
- [133] The Fermi-LAT Collaboration, *ApJ* **834**, 110 (2017), [arXiv:1611.03184](#).
- [134] S. S. Wilks, *Ann. Math. Statist.* **9**, 60 (1938).
- [135] S. S. Wilks, *Mathematical Statistics* (Wiley, New York, NY, 1962).
- [136] G. Cowan, K. Cranmer, E. Gross, and O. Vitells, *European Physical Journal C* **71**, 1554 (2011), [arXiv:1007.1727 \[physics.data-an\]](#).
- [137] A. V. Macciò, A. A. Dutton, and F. C. van den Bosch, *MNRAS* **391**, 1940 (2008), [arXiv:0805.1926](#).
- [138] F. Prada, A. A. Klypin, A. J. Cuesta, J. E. Betancort-Rijo, and J. Primack, *MNRAS* **423**, 3018 (2012), [arXiv:1104.5130](#).
- [139] A. A. Dutton and A. V. Macciò, *MNRAS* **441**, 3359 (2014), [arXiv:1402.7073](#).
- [140] M. A. Sánchez-Conde, M. Cannoni, F. Zandanel, M. E. Gómez, and F. Prada, *J. Cosmology Astropart. Phys.* **12**, 011 (2011), [arXiv:1104.3530 \[astro-ph.HE\]](#).
- [141] V. S. Berezinsky, V. I. Dokuchaev, and Y. N. Eroshenko, *J. Cosmology Astropart. Phys.* **11**, 059 (2013), [arXiv:1308.6742 \[astro-ph.CO\]](#).
- [142] B. Carr, F. Kühnel, and M. Sandstad, *Phys. Rev. D* **94**, 083504 (2016), [arXiv:1607.06077 \[astro-ph.CO\]](#).